The University of Osaka
Institutional Knowledge Archive

Title	Study on interprotein interactions for electron transfer complexation and amyloid fibrillation
Author(s)	木下, 岬
Citation	大阪大学, 2018, 博士論文
Version Type	VoR
URL	https://doi.org/10.18910/69369
rights	
Note	

The University of Osaka Institutional Knowledge Archive : OUKA

https://ir.library.osaka-u.ac.jp/

The University of Osaka

Study on interprotein interactions for electron transfer complexation and amyloid fibrillation

(電子伝達複合体およびアミロイド線維形成における蛋白質間相互作用の研究)

A Doctoral Thesis
by
Misaki Kinoshita

Submitted to the Graduate School of Science
Osaka University

February 2018

Acknowledgement

This work has been performed under the direction of Associate Professor Young-Ho Lee (Institute for Protein Research, Osaka University). I would like to express my great gratitude to him for guidance of my work with detailed, interesting, and kind discussion and enthusiastic encouragement. Without him, I would definitely not have a deep interest in protein science. I can never forget the grace that I received from him until now. Thanks to him, I had a very meaningful three years.

I would thanks to Professor Yuji Goto (Institute for Protein Research, Osaka University) for many amazing guidance of science and life. I have not received direct guidance from him, but I think that I learned a lot from his attitude as a researcher. Through there were many events, I think that those were precious experiences in retrospect. I will do my best by taking advantage of these experiences.

I deeply appreciate to Professor Toshiharu Hase (Osaka University). In my master's degree, I learned much from him about plant biology and protein science. Without these experiences, I would not be a Ph.D. student. I also remember that I broke the large centrifuge, and I would apologize him again.

I would like to express my great appreciation to Dr. Yuxi Lin (currently Sookmyung Women's University, Korea). It is a great memory that I spent much time with him for various experiments. I was often helped by him and learned a lot from him about scientific skills and backgrounds. I want to spent time in future with him.

During my Ph.D course, I had nice opportunities to work with Mrs. Erina Kakimoto, Mr. Tetsuhe Uenoyama, and Mr. Dai Ito. They are past and present members of the current laboratory that I belong to with opportunities of teaching them. I really think that all these opportunities made me mature. Not only teaching, I was also supported by them for my study and many other things.

I deeply appreciate to Assistant Professor Toshihiko Sugiki (Institute for Protein Research, Osaka University) for his kind supports of NMR measurements. I would like to collaborate with him in future.

I would acknowledge Assistant Professsot Masatomo So (Institute for Protein Research, Osaka University), Assistant Professor Yuichi Yoshimura (Hiroshima University), and Mr. Masayuki Adachi for helpful and valuable advices. In addition, I would acknowledge other members of the Laboratory of Protein Folding for fun time during my school life.

To Dr. Shingo Kikuchi, I deeply appreciate to you. I learned many things about experimental techniques and other various things. It was nice time that I talked with you at midnight. I will not able to 'discuss' at night, but I am looking forward to seeing you in the future, again.

Last, I express great appreciations to my mother and father, and my precious wife, Sayaka. To my mother and father, I could overcome this three years with your extensive and kind supports. Thank you for giving birth to a healthy and duarable body and raising up to now. I have managed to work hard and do best due to this my body. I can never thank you enough.

To Sayaka, I am glad to have met you. I cannot write much appreciation here because it is embarrassing. I will tell you my thanks by meeting face to face. I'm looking forward to our future together.

Misaki Kinoshita
February 2018

Table of contents

Acknowledgement ……………………………………………………………………i

Abbreviation ……………………………………………………………………v

Chapter 1. General introduction ……………………………………………………………………1

Chapter 2. Physicochemical nature of interface controlling ferredoxin NADP$^+$ reductase activity through its interprotein interaction with ferredoxin

Abstract ……………………………………………………………………12

1. Introduction ……………………………………………………………………12
2. Materials and methods ……………………………………………………………………14
    - 2.1. Preparation of proteins
    - 2.2. Assay for electron transfer of FNR
    - 2.3. Assay for electron transfer of SiR
    - 2.4. Circular dichroism measurements
    - 2.5. Isothermal titration calorimetry measurements
    - 2.6. Solution NMR measurements of FNR
    - 2.7. Computational docking simulation between FNR and Fd
3. Results ……………………………………………………………………18
    - 3.1. Interface mutations differentially affected enzymatic activity between FNR and SiR
    - 3.2. NADPH-dependent FNR activity using wild-type and mutant Fds
    - 3.3. Investigation of structural changes in Fd mutants by various spectroscopies
    - 3.4. Thermodynamic characterization of Fd:FNR interaction monitored by calorimetry
    - 3.5. Temperature dependenceof thermodynamic parameters for Fd:FNR complexation
    - 3.6. Residue-based investigation of Fd-FNR interactions using NMR spectroscopy
4. Discussion ……………………………………………………………………27

Supplementary information ……………………………………………………………………33

Chapter 3. Energetic basis on interactions between ferredoxin and ferredoxin NADP$^+$ reductase at varying physiological conditions.

Abstract ……………………………………………………………………46

1. Introduction ……………………………………………………………………46
2. Materials and methods ……………………………………………………………………47
    - 2.1. Preparation of Fd and FNR
    - 2.2. Isothermal titration calorimetry measurements
3. Results and discussion ……………………………………………………………………48
    - 3.1. Observation of heat for the Fd:FNR complex formation by ITC
    - 3.2. Energetic cost of enthalpy for complex formation and its possible biological role
    - 3.3. Heat capacity change reflects binding modes between Fd and FNR

    3.4. Purely entropy-driven formation of the Fd:FNR complex through the balance between protein flexibility and dehydration
    3.5. Context-dependent energetic interplay characterized by the driving force plot and its biological relevance
Supplementary information 59

Chapter 4. Energy landscapes of amyloid formation of β_2-microglobrin.

Abstract 70
1. Introduction 71
2. Materials and methods 73
    2.1. Reagents and proteins
    2.2. ITC measurements
    2.3. ThT assay
    2.4. CD measurements
    2.5. AFM measurements
3. Results 74
    3.1. Monitoring and thermodynamic analyses of β2m amyloid formation using ITC at different temperatures
    3.2. Monitoring and thermodynamic analyses of β2m amyloid formation using ITC at different shear forces
    3.3. Monitoring and thermodynamic analyses of β2m amyloid formation using ITC under crowded milieus
    3.4. Characterization of morphologies of β2m amyloid fibrils
    3.5. Kinetic analysis of formation of β2m amyloid fibrils using ITC thermograms
4. Discussion 79
    4.1. Energy landscape of incorrect folding-induced amyloidogenesis and correct folding of β2m
    4.2. Energy landscape of polymorphic amyloid formation of β2m
Supplementary information 83

Publication list 90

Abbreviations

AFM	atomic force microscopy
β2m	β_2-microgloblin
CD	circular dichroism
CSP	chemical shift perturbation
ΔC_p	heat capacity change
ΔG	Gibbs-free energy change
ΔH	enthalpy change
ΔS	entropy change
$^{\mathrm{mix}}\Delta S$	mixing entropy change
$^{\mathrm{dehyd}}\Delta S$	dehydration entropy change
$^{\mathrm{conf}}\Delta S$	conformational entropy change
E_a	activation energy for FNR catalysis
$E_\mathrm{a,Elong}$	activation energy for elongation
$E_\mathrm{a,Nu}$	activation energy for nucleation
EM	electron microscopy
ET	electron transfer
Fd	ferredoxin
FNR	ferredoxin $\mathrm{NADP^+}$ reductase
HSQC	heteronuclear single quantum coherence
ITC	isothermal titration calorimetry / isothermal titration calorimeter
k_cat	catalytic constant
K_d	dissociation constant
k_Elong	elongation rate constant
K_m	Michaelis-Menten constant
k_Nu	nucleation rate constant
NAD	nicotinamide adenine dinucleotide
$\mathrm{NADP^+}$/NADPH	nicotinamide adenine dinucleotide phosphate (oxidized /reduces forms, respectively)
NMR	nuclear magnetic resonance
SiR	sulfite reductase
ThT	Thioflavin T

Chapter 1

General introduction

Protein is one of the most fundamental elements in living organisms together with lipid membranes, nucleic acids, and small molecules. Proteins, which are synthesized as nascent polypeptide chains on ribosomes, fold spontaneously into their unique and specific three-dimensional structures based on the code of the primary structure (Fig. 1). Three-dimensional structures of proteins are determined using X-ray crystallography, nuclear magnetic resonance spectroscopy, and electron microscopy [1]. These unique conformations are, in many cases, required for biological functions, including enzymatic catalysis, electron transfers, proton tunneling, signal transfers, and so on. Some proteins function through direct intermolecular interactions. Intermolecular interactions are driven by many physical forces such as electrostatic attractive and repulsive forces, van der Waals forces, and hydrogen bonding [2] which are controlled intrinsically and precisely through internal factors including interactions among amino acid residues. In addition, the external environment factors including ionic strength, temperature, pH, and crowding effects influence and regulate intermolecular interactions [3-5]. Although internal and external factors control protein interactions with binding partners for function and are related to the stress responses for homeostasis, much remains to be understood on effects of how internal and external factors on protein function and disease based on systematic studies.

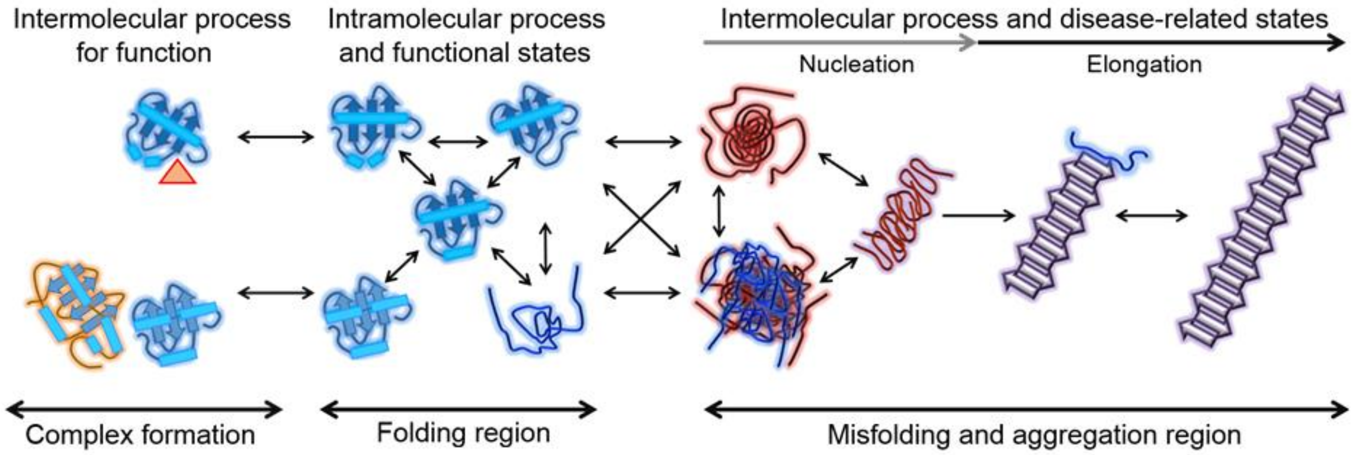
Intermolecular process for function
Intramolecular process and functional states
Intermolecular process and disease-related states
Nucleation
Elongation
Complex formation
Folding region
Misfolding and aggregation region

Fig. 1. Representative protein behaviors.

Unstructured proteins folded to native functional structures ensembles of isoenergetic conformers (Folding region), native proteins interact with partner molecules using intermolecular forces (Complex formation). Destabilized proteins with partial or largely unfolded proteins aggregate into disease related states (Misfolding and aggregation region).

Native proteins are often destabilized by many types of stresses. Although partially or fully unfolded proteins are capable of being correctly refolded into native states or degraded to short polypeptides or amino acids under the well-regulated biological machinery and quality control system [6, 7]. Failure in these controls make unfolded proteins insoluble and induce irreversible aggregates such as ordered β-structured amyloid fibrils or amorphous aggregates [8]. (Fig. 1) These aggregated proteins are closely responsible for a number of diseases, listed in table 1. Importantly, dysfunctional and disease-causing protein aggregate are products of misconducted and misregulrated intermolecular interactions among proteins and other molecules [8, 9]. However, the mechanism of how native proteins play roles in biological activity with functional and controlled intermolecular interactions and destabilized proteins form deleterious aggregates as a result of misregulated intermolecular interactions is required to be clearly understood, which is hopefully helpful for the advance in the research fields of basic science, medical science, and material science.

In this thesis, I focused on both functional and pathogenic interactions in order to obtain comprehensive and general understanding of intermolecular interactions. Functional interpotein interactions were studied by classifying two-types of interactions, intrinsic factors such as mutagenesis which affects interprotein interactions as well as extrinsic factors which mimic physiological conditions where proteins of interest exist,

Table 1. Representative human misfoding diseases and their related protein and peptides

Disease	Aggregating protein or peptide
Alzheimer's disease	Amyloid-β peptides, Tau
Parkinson's disease	α-Synuclein
Type II diabetes	Amylin
Frontotemporal dementia	Tau
Prion disease	Prion
Amyotrophic lateral sclerosis	Superoxide dismutase 1
Hemodialysis-related amyloidosis	β_2-Microgloblin
Huntington's disease	Huntingtin
Light chain amyloidosis	Ig V_L domain
Fatal systemic amyloidosis	Lysozyme
Secondary systemic amyloidosis	Serum amyloid A
Cataract	γ-Crystalline
Senile systemic amyloidosis	Transthyretin

using biochemical and biophysical approaches. Amyloid formation of proteins by pathogenic interprotein interactions under varying extrinsic factors was examined in details from the view point of thermodynamics and kinetics.

In the chapter 2, I studied how mutation of ferredoxin (Fd) [10, 11] influences interprotein interactions with ferredoxin dependent enzymes and enzymatic activity, especially Fd-NADP$^+$ reductase (FNR). In the chapter 3, I examined how physiological conditions in chloroplasts such as not only pH gradients but also changes in temperature and ionic strength [12]. Fd and FNR, used for model proteins, are localized in chloroplasts and important players for electron transfer and biomolecule metabolisms.

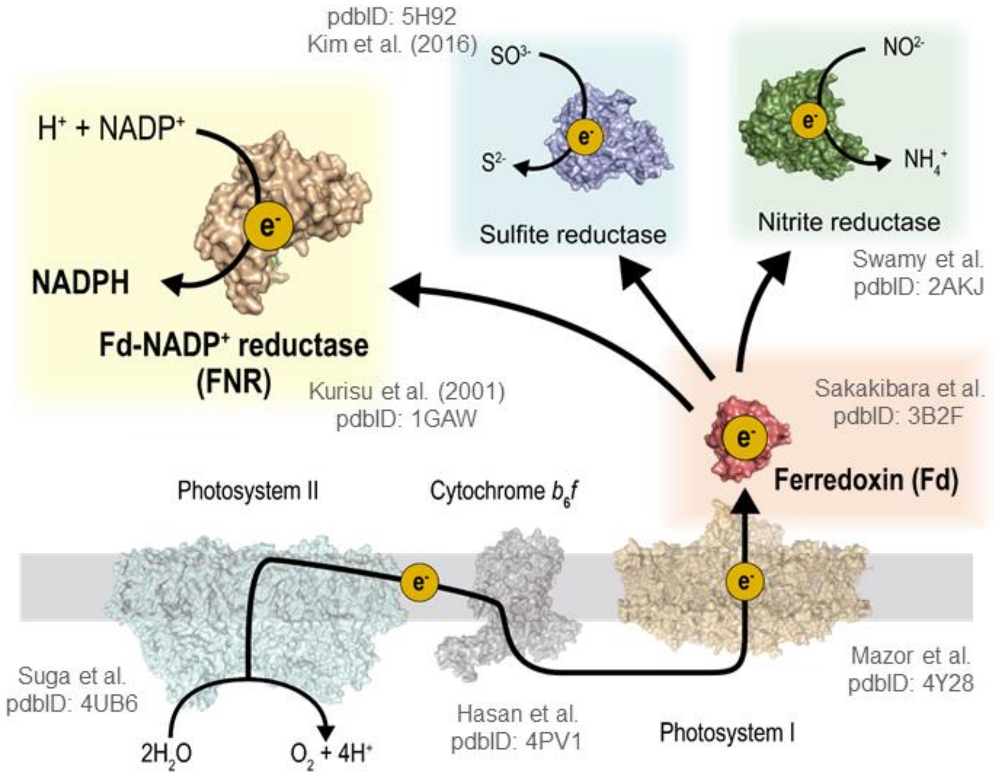
pdbID: 5H92
Kim et al. (2016)
SO^{3-}
S^{2-}
e-
Sulfite reductase
NO^{2-}
e-
NH_4^+
Nitrite reductase
Swamy et al.
pdbID: 2AKJ
$H^+ + NADP^+$
e-
NADPH
Fd-NADP$^+$ reductase
(FNR)
Kurisu et al. (2001)
pdbID: 1GAW
Sakakibara et al.
pdbID: 3B2F
e-
Ferredoxin (Fd)
Photosystem II
Cytochrome b_6f
e-
e-
Suga et al.
pdbID: 4UB6
$2H_2O$
$O_2 + 4H^+$
Hasan et al.
pdbID: 4PV1
Photosystem I
Mazor et al.
pdbID: 4Y28

Fig. 2. Electron distribution by Fd flow in plant chloroplasts.

Electrons produced from water were transferred to cytochrome b6f complex through photosystem II and subsequently flow photosystem I. Fd receives an electron activated in photosystem I and distributes electrons to various enzymes including FNR, sulfite reductase, and nitrite reductase for metabolisms.

In chloroplasts of plants, the electron transfer (ET) photosystem, mainly composed of type-I photosystem (PSI), cytochrome b_6f, and type-II photosystem (PSII), is an essential energy source (Fig. 2) [13]. In the terminal part of the ET system, an electron is transferred to Fd which is a small acidic protein (~10 kDa) including one [2Fe-2S] cluster for electron tranfer. Electrons in reduced Fd are further distributed to various enzymes for metabolic systems, for instance, $NADP^+$ reduction for carbon assimilations, nitrogen assimilation, and sulfite assimilation (Fig. 2).

In general, the distance between electron donors and acceptors is the major factor for ET efficiency.[14] Thus, complex formation between Fd and Fd-dependent partner enzymes in a specific orientation where the optimized distance and local environments adequate for an electron flow is markedly important. On the other hand, complexation between Fd and Fd-dependent enzymes occurs based on various physicochemical intermolecular interaction forces which are largely classified to electrostatic and non-electrostatic interactions. Electrostatic interactions include salt bridges between negatively and positively charged atomic groups, and dipolar-dipolar interactions between weekly-charged atoms [15]. Non-electrostatic interactions include representatively hydrogen bonding, pi-pi stacking interaction, hydrophobic interactions, and van der Waals interactions [16].

Fd accommodates acidic patches on its surface which consists a lot of acidic amino acids, glutamate acid and aspartic acid, and shows a relatively low isoelectric point (pI ~ 3.9). Oppositely, Fd-dependent enzymes have patches which are composed of basic amino acids and have been implicated as main binding sites for Fd. For this reason, it has been generally considered that electrostatic interactions are main actors for the complex formation Fd and Fd-dependent enzymes [17]. However, recent studies raised questions on roles of non-electrostatic interactions for complex formation, electron transfer, and enzyme activity [18].

In the chapter 2, I show that the importance of non-electrostatic forces for interprotein interactions between Fd and FNR and FNR activity using biochemical and biophysical methods. I investigated the role of non-covalent interactions by focusing residues on hydrophobic surfaces of Fd for FNR binding using mainly mutagenesis, enzymatic assay, isothermal titration calorimetry (ITC), solution NMR spectroscopy, and MD simulations. I revealed that non-electrostatic interactions on hydrophobic surfaces are also important for controlling of interprotein affinity, configuration of complex, and FNR activity together with electrostatic interactions, and that intrinsic factors such as mutation impact interprotein interactions and protein funtion. In the chapter 3, I performed in-depth studies on Fd and FNR interactions by changing physiological conditions from the thermodynamic point of view using ITC. It was demonstrated that, even for changes in extrinsic environmental factors, both non-covalent forces, electrostatic and non-electrostatic interactions, are decision makers to determine affinity between proteins. Interprotein interactions were well regulated with thermodynamics depending on external stresses.

In the chapter 4, I examined thermodynamics and kinetics of amyloid formation which is a result of pathogenic and misregulated interprotein interactions using ITC and other biophysical methods. Protein misfolding and aggregations have been recognized as the main cause of the numerous and serious diseases (Table 1). Especially, formation of amyloid fibrils and amyloid fibrils themselves show strongly relation to various neurodegenerative disorders, such as Alzheimer's and Parkinson's diseases [19]. Amyloid aggregation damaged various tissues, cells, organelles and thereby bringing about pathogenesis.

Proteins in the denatured state, i.e., unstable proteins, have a high aggregation propensity due to exposure of hydrophobic regions which are buried to cores of native protein structures. Amyloid aggregation is one type of insoluble protein aggregation. Amyloid fibrils are defined by their fibrillary morphology and β-sheet rich structures. (Fig.3) A number of hydrogen bonds among monomers in β-sheets are formed and arranged along the fibril axis, known as the cross-β-sheet structure which are easily discriminated based on the characteristic far-UV circular dichroism (CD) spectra.

A unique feature is in the self-assembling process. Amyloid fibrils form by way of two successive processes: nucleation and subsequent elongation. (Fig. 3) In the nucleation process, amyloidogenic monomer proteins (i.e., precursors) assemble and aggregate into the small amyloid nucleus, which is energetically unfavorable with the high activation energy and thus produces the lag time. Elongation (i.e., fibril growth) is

Table 2. Summary of three-dimentional structures of amyloid-like fibrils

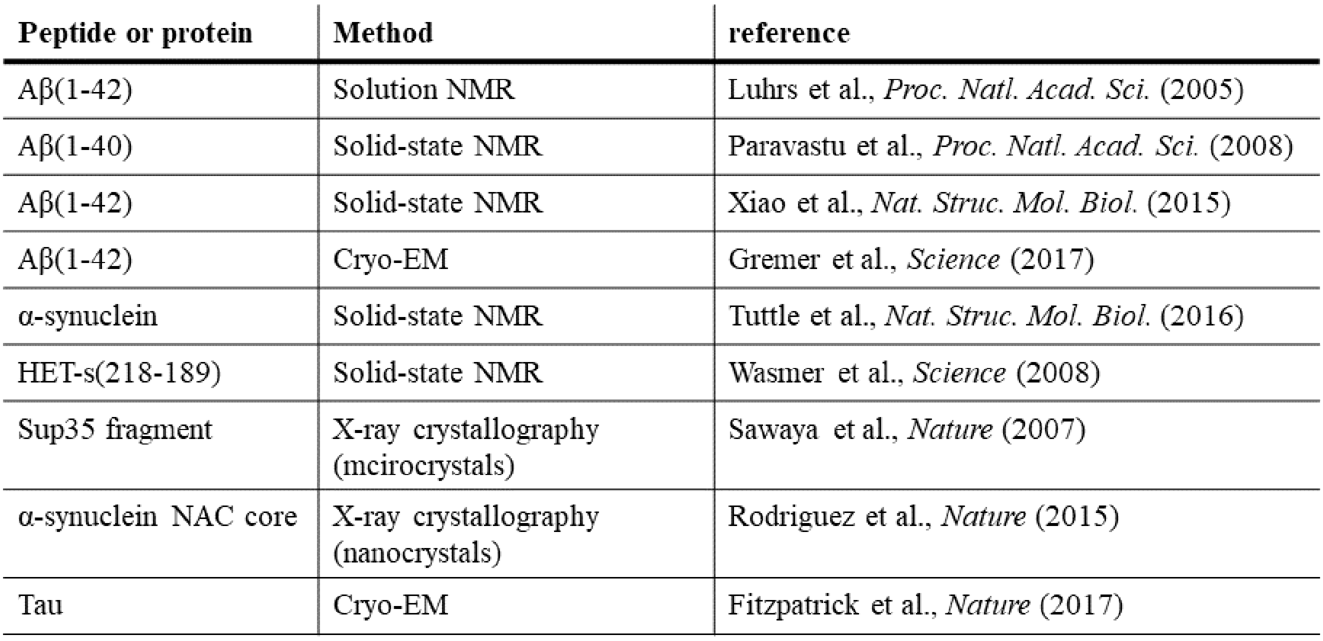

Peptide or protein	**Method**	**reference**
Aβ(1-42)	Solution NMR	Luhrs et al., *Proc. Natl. Acad. Sci.* (2005)
Aβ(1-40)	Solid-state NMR	Paravastu et al., *Proc. Natl. Acad. Sci.* (2008)
Aβ(1-42)	Solid-state NMR	Xiao et al., *Nat. Struc. Mol. Biol.* (2015)
Aβ(1-42)	Cryo-EM	Gremer et al., *Science* (2017)
α-synuclein	Solid-state NMR	Tuttle et al., *Nat. Struc. Mol. Biol.* (2016)
HET-s(218-189)	Solid-state NMR	Wasmer et al., *Science* (2008)
Sup35 fragment	X-ray crystallography (mcirocrystals)	Sawaya et al., *Nature* (2007)
α-synuclein NAC core	X-ray crystallography (nanocrystals)	Rodriguez et al., *Nature* (2015)
Tau	Cryo-EM	Fitzpatrick et al., *Nature* (2017)

faster than nucleation due to with the low activation energy. Precursor monomers are adsorbed on the preformed fibril edges and rearranged their structures into the cross-β-sheet structures [19].

Amyloid aggregation *in vivo* and *in vitro* is detected using various fluorescent dyes including Congo-red and Thioflavin-T (ThT). These fluorophores bind to the hydrophobic fibril surfaces and emit fluorescence and thus ThT-based assay is the most popular and general method for observation of formation of amyloid fibrils and for detecting of amyloid fibrils. Atomic force microscopy (AFM) and transmission electron microscopy (TEM) are also widely used for detecting amyloid fibrils as they provide direct evidence of amyloid fibrils. Solid-state NMR spectroscopy, X-ray crystallography, and cryo-EM further revealed three-dimensional structures of amyloid fibrils at the atomic resolution (Table 2).

With the improvement and development of new instruments and methodologies, structures of amyloid fibrils and basic mechanisms of amyloidogenesis have been increasingly revealed. However, information on detailed processes of amyloid formation based on systematic studies with the view of thermodynamics and kinetics is still limited as amyloid formation is heterogeneous, dynamic, and transient process in nature. Especially, the polymorphic property, that is, formation of various types of fibrillar structures or morphologies from the same amyloidogenic proteins, is largely unknown although polymorphs must be a generic nature of amyloid formation. Generation of polymorphism has been considered to be induced by the distinct surrounding extrinsic factors, such as pH, temperature, ionic strength, and type of agitation due to generation of context-dependent nucleation [20].

Thus, I challenged characterization of thermodynamic and kinetic processes of polymorphic amyloid formation of β_2-microgroblin (β2m), a causative protein for dialysis-related amyloidosis, under various extrinsic stresses such as temperature, the strength of agitation, and crowding effects, using ITC. I previously showed the powerful usage of ITC for studying protein aggregation. I further expanded utility of ITC for protein aggregation by incorporating kinetic analyses and constructing energy landscape of amyloid formation in terms of polymorphism. Amyloid formation of β2m formed through pathogenic and misleaded interprotein interactions was susceptible to extrinsic factors and thereby causing polymorphic amyloidogenesis which was difficult to detect but could be distinguishable based on thermodynamic an kinetic parameters of ITC.

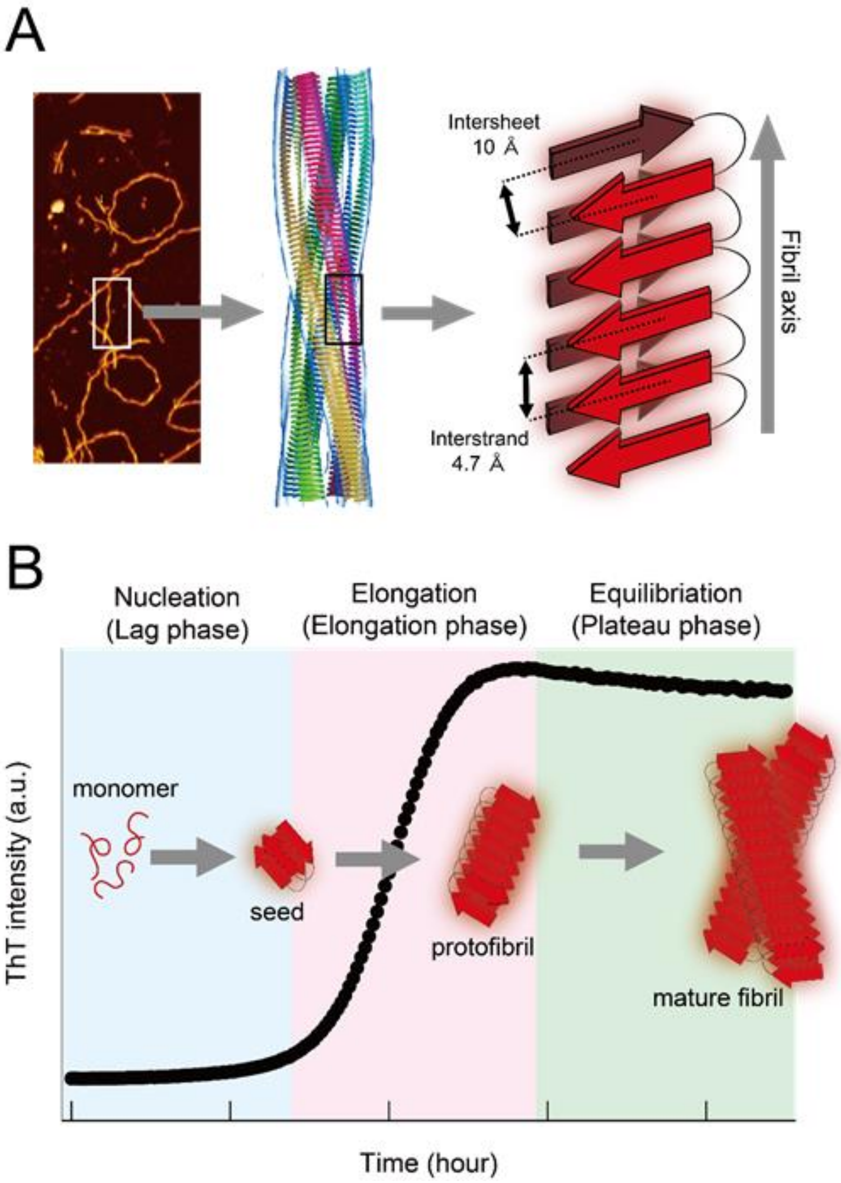
A
Intersheet
10 Å
Interstrand
4.7 Å
Fibril axis
B
Nucleation
(Lag phase)
Elongation
(Elongation phase)
Equilibriation
(Plateau phase)
ThT intensity (a.u.)
monomer
seed
protofibril
mature fibril
Time (hour)

Fig. 3. Characters of amyloid fibrils.

A) An AFM image of fibrils (left), famous model of an amyloid atomic structure (center), and representative structural character of an amyloid fibril. From left to right, viewpoint becomes detailed. B) Explanation of fibril formation using ThT fluorescence, In Lag-phase (light blue), amyloidogenic monomer peptides/proteins form small seed aggregates. In Elongation-phase (purpe), seeds elongate to protofibril through adsorption of monomer to their edges, and finally most of peptides/protein are in fibrils, i.e. a system is in equilibrium (light green).

In summary, I focused largely on functional and pathogenic interprotein interactions. Both functional and dysfunctional interactions were controlled by internal protein interactions which were affected by extrinsic surrounding factors. The environment in the living systems is easy to be changed depending on the change in external environments, and the intermolecular interaction of proteins must be affected by these changes. Capability of adaptation of internal protein interactions using both electrostatic and non-electrostatic forces stimulated by exogenous stresses may be viewed as a general way of proteins to be survived. When control systems work normally and correctly, even misregulated protein interactions may be recovered for keeping homeostasis. However, when systems fail to handle misconducted interprotein interactions, it may be in the risky pathogenic states by forming disease-causing protein aggregates such amyloid fibrils. Although more detailed *in vitro* and *in vivo* information is required for thorough understanding of protein behaviors, the study in this thesis is expected to contribute to improvement of our understanding in a variety of scientific disciplines and application fields.

References

[1] J. Frank, Single-particle imaging of macromolecules by cryo-electron microscopy, Annu Rev Biophys Biomol Struct, 31 (2002) 303-319.

[2] S. Jones, J.M. Thornton, Principles of protein-protein interactions, Proc Natl Acad Sci U S A, 93 (1996) 13-20.

[3] R.J. Ellis, Macromolecular crowding: obvious but underappreciated, Trends Biochem Sci, 26 (2001) 597-604.

[4] D. Molodenskiy, E. Shirshin, T. Tikhonova, A. Gruzinov, G. Peters, F. Spinozzi, Thermally induced conformational changes and protein-protein interactions of bovine serum albumin in aqueous solution under different pH and ionic strengths as revealed by SAXS measurements, Phys Chem Chem Phys, 19 (2017) 17143-17155.

[5] E. Sahin, A.O. Grillo, M.D. Perkins, C.J. Roberts, Comparative effects of pH and ionic strength on protein-protein interactions, unfolding, and aggregation for IgG1 antibodies, J Pharm Sci, 99 (2010) 4830-4848.

[6] C. Hammond, A. Helenius, Quality control in the secretory pathway, Curr Opin Cell Biol, 7 (1995) 523-529.

[7] M.R. Wilson, S.B. Easterbrook-Smith, Clusterin is a secreted mammalian chaperone, Trends Biochem Sci, 25 (2000) 95-98.

[8] C.M. Dobson, Protein folding and misfolding, Nature, 426 (2003) 884-890.

[9] Y.H. Lee, Y. Goto, Kinetic intermediates of amyloid fibrillation studied by hydrogen exchange methods with nuclear magnetic resonance, Biochim Biophys Acta, 1824 (2012) 1307-1323.

[10] K. Fukuyama, T. Hase, S. Matsumoto, T. Tsukihara, Y. Katsube, N. Tanaka, M. Kakudo, K. Wada, H. Matsubara, Structure of S. platensis [2Fe-2S] ferredoxin and evolution of chloroplast-type ferredoxins, Nature, 286 (1980) 522.

[11] L.E. Mortenson, R.C. Valentine, J.E. Carnahan, An electron transport factor from Clostridium pasteurianum, Biochem

Biophys Res Commun, 7 (1962) 448-452.

[12] B. Demmig, H. Gimmler, Properties of the Isolated Intact Chloroplast at Cytoplasmic K Concentrations : I. Light-Induced Cation Uptake into Intact Chloroplasts is Driven by an Electrical Potential Difference, Plant Physiol, 73 (1983) 169-174.

[13] N. Nelson, C.F. Yocum, Structure and function of photosystems I and II, Annu Rev Plant Biol, 57 (2006) 521-565.

[14] H.L. Tavernier, M.D. Fayer, Distance Dependence of Electron Transfer in DNA: The Role of the Reorganization Energy and Free Energy, The Journal of Physical Chemistry B, 104 (2000) 11541-11550.

[15] K.A. Sharp, B. Honig, Electrostatic interactions in macromolecules: theory and applications, Annu Rev Biophys Biophys Chem, 19 (1990) 301-332.

[16] D. Chandler, Interfaces and the driving force of hydrophobic assembly, Nature, 437 (2005) 640-647.

[17] S.B. Mellor, K. Vavitsas, A.Z. Nielsen, P.E. Jensen, Photosynthetic fuel for heterologous enzymes: the role of electron carrier proteins, Photosynthesis Research, 134 (2017) 329-342.

[18] Y. Sakakibara, H. Kimura, A. Iwamura, T. Saitoh, T. Ikegami, G. Kurisu, T. Hase, A new structural insight into differential interaction of cyanobacterial and plant ferredoxins with nitrite reductase as revealed by NMR and X-ray crystallographic studies, The Journal of Biochemistry, 151 (2012) 483-492.

[19] T.P.J. Knowles, M. Vendruscolo, C.M. Dobson, The amyloid state and its association with protein misfolding diseases, Nature Reviews Molecular Cell Biology, 15 (2014) 384.

[20] R. Tycko, Physical and structural basis for polymorphism in amyloid fibrils, Protein Sci, 23 (2014) 1528-1539.

Chapter 2

Physicochemical nature of interfaces controlling ferredoxin NADP$^+$ reductase activity through its interprotein interactions with ferredoxin.

Abstract

Although acidic residues of ferredoxin (Fd) are known to be essential for activities of various Fd-dependent enzymes, including ferredoxin NADP$^+$ reductase (FNR) and sulfite reductase (SiR), through electrostatic interactions with basic residues of partner enzymes, non-electrostatic contributions such as hydrophobic forces remain largely unknown. I herein demonstrated that intermolecular hydrophobic and charge–charge interactions between Fd and enzymes were both critical for enzymatic activity. Systematic site-directed mutagenesis, which altered physicochemical properties of residues on the interfaces of Fd for FNR /SiR, revealed various changes in activities of both enzymes. The replacement of serine 43 of Fd to a hydrophobic residue (S43W) and charged residue (S43D) increased and decreased FNR activity, respectively, while S43W showed significantly lower SiR activity without affecting SiR activity by S43D, suggesting that hydrophobic and electrostatic interprotein forces affected FNR activity. Enzyme kinetics revealed that changes in FNR activity by mutating Fd correlated with Km, but not with kcat or activation energy, indicating that interprotein interactions determined FNR activity. Calorimetry-based binding thermodynamics between Fd and FNR showed different binding modes of FNR to wild-type, S43W, or S43D, which were controlled by enthalpy and entropy, as shown by the driving force plot. Residue-based NMR spectroscopy of ^{15}N FNR with Fds also revealed distinct binding modes of each complex based on different directions of NMR peak shifts with similar overall chemical shift differences. I proposed that subtle adjustments in both hydrophobic and electrostatic forces were critical for enzymatic activity, and these results may be applicable to protein-based electron transfer systems.

1. Introduction

A large number of biological processes are regulated by intermolecular interactions among various biomolecules, small compounds, and metal ions under the control of kinetics and thermodynamics, with the aim of maintaining homeostasis [1–3]. The regulation of protein interactions with target molecules is of particular importance because misguided intermolecular interactions often lead to impaired enzymatic activities and protein functions, thereby resulting in dysfunctional organelles and numerous diseases [4].

One of the most controlled protein-based physiological processes is the electron transport chain in photosynthesis and respiration [5]. In these metabolic processes, a series of soluble proteins/enzymes and membrane protein complexes play pivotal roles in electron transfer by communicating with target and binding molecules in response to changes in environmental conditions such as variations in pH, temperature, and the redox state [6–8]. Detailed studies on enzyme activities and electron transfer rates based on the static and dynamic structures determined by X-ray crystallography and solution NMR spectroscopy have increased our understanding of the molecular mechanisms underlying electron flow and enzymatic activities in photosynthesis and respiration [3,9–12]. Solution NMR spectroscopy and calorimetry have provided further information on the dynamic structures of proteins and molecular origins of intermolecular interactions for protein functions [3,13].

Several key electron-carrying proteins, such as plastocyanin and ferredoxin (Fd), have been identified in the chloroplasts of higher plants for photosynthesis [14,15]. Electron carrier proteins transport an electron to their physiological redox partner molecules in a manner that has been shown to depend on differences in redox potential [16]. On the other hand, well-regulated protein–protein interactions between electron-carrier proteins and redox partner proteins/enzymes were found to maximize efficient intermolecular electron transfer and relayed enzymatic reactions [8], which emphasized the consequences of the formation of electron transport-competent protein complexes. However, the dominant factors controlling interprotein interactions have not yet been examined in detail from the viewpoints of enzymatic kinetics and binding thermodynamics together with the determination of an available complex structure.

Fd is considered to be a good model protein because it transfers an electron obtained from photosystem I to several target enzymes, including ferredoxin-NADP$^+$ reductase (FNR), sulfite reductase (SiR), nitrite reductase (NiR), and hydrogenase [17], through the formation of electron transfer protein complexes [9,11,18]. Fd is a small acidic protein (~10.5 kDa) that accommodates the redox center of the [2Fe–2S] cluster [5]. Previous studies suggested that the negatively-charged residues of Fd stabilized a complex through complementary electrostatic interactions with the positively-charged residues of partner enzymes, as previously reported in Fd and FNR binding in photosynthesis and Fd and SiR binding in sulfur assimilation [11,18,19].

Although diverse biochemical methods are useful for indirectly elucidating the interprotein electrostatic interactions of Fd with several enzymes [20,21], the three-dimensional structure of the complex provides straightforward information for identifying interprotein interactions at the atomic level [22]. The complex structure between maize leaf Fd and FNR, which was the only available structure among several complexes between Fd and partner enzymes in plants, showed that interfaces mostly consisted of electrostatic interactions, including five salt bridges, a large number of hydrogen bonds, and hydrophobic contacts [22,23]. FNR is a relatively large multidomain enzyme (~35.5 kDa) that reduces NADP$^+$ to NADPH by transferring two electrons via flavin adenine dinucleotide (FAD) in FNR and hydride [23–25]. Solution NMRbased investigations on Fd further supported electrostatic interactions between the oppositely-charged residues of Fd and FNR [20,22,26].

A recent thermodynamic study using solution NMR spectroscopy and calorimetry reported that increases in the FNR backbone flexibility of regions remote from interfaces and dehydration from both apolar and polar surfaces were important for the formation of the Fd:FNR complex [3,22]. These findings indicated the contribution of hydrophobic interactions, which have received less attention than electrostatic contributions, to FNR activity. The strong potential for charge clusters on the surfaces of electron transfer proteins [25,27] and NMR invisible hydrophobic regions of Fd due to paramagnetic relaxation enhancements from the unpaired electrons of iron [9] may have led to the biased interpretation of electrostatic interactions by masking hydrophobic contributions.

By using the biochemical approaches of systematic site-directed mutagenesis and activity measurements in combination with the biophysical methods of isothermal titration calorimetry, solution NMR spectroscopy, and docking simulations, I herein investigated the contribution of hydrophobic interactions between Fd and FNR to FNR activity together with charge–charge interactions. I showed that the hydrophobic forces of Fd were also key to FNR activity together with conventional electrostatic forces, and that the delicate balance between these two forces regulated FNR activity by controlling interprotein interactions between Fd and FNR.

2. Materials and methods

2.1. Preparation of proteins

All site-directed Fd mutants on the hydrophobic surfaces of maize leaf-type Fd (Fd I) were prepared using a QuikChange Lightning Site Directed mutagenesis kit (Agilent Technologies, USA) and recombinant maize-FdI plasmid DNA as a template [28]. The mutation sites and sequence integrity of the entire coding region were confirmed by DNA sequencing. Wild-type and mutant Fds were expressed from Escherichia coli BL21 (DE3) cells and purified according to previously described methods [29].

The preparation of recombinant maize leaf FNR (L-FNR I) and 15N-labeled FNR was based on previous studies [19,30]. Fd and FNR concentrations were determined using the molar extinction coeffi- cients of 9680 M^{-1} cm^{-1} at 423 nm and 10,000 M^{-1} cm^{-1} at 460 nm, respectively.

2.2. Assay for electron transfer activity of FNR

The nicotinamide adenine dinucleotide phosphate (NADPH)-dependent reduction of Fd by FNR was measured at 298 K, as described previously [19], by monitoring increases in reduced cytochrome c (Nacalai Tesque, Japan) at 550 nm in an assay mixture of 50 mM Tris–HCl buffer (pH 7.5) containing 50 µM NADPH, 20 nM FNR, 2.5 µM (Fig. 1C) or 1.25 µM Fd (Fig. 1E), and 200 µM cytochrome c, which represented the NADPH-generating system. The Michaelis constant (K_m) at 298 K and turnover number (k_{cat}) at various temperatures (288, 293, 298, and 303 K) were calculated by fitting to the following Michaelis– Menten equation:

$$v = \frac{k_{cat}[\mathrm{FNR}]_0[\mathrm{Fd}]}{[\mathrm{Fd}] + K_m}$$

Equation (1)

where v indicates the initial velocity of the catalytic reaction of FNR, and $[\mathrm{FNR}]_0$ and [Fd] indicate the concentrations of FNR and Fd in the reaction mixture, respectively.

2.3. Assay for electron transfer activity of SiR

Fd-dependent sulfite reduction by SiR was assayed by monitoring the final product of cysteine using a reconstituted electron transfer system [11]. Reaction mixtures in 50 mM Tris–HCl (pH 7.5) consisted of 200 nM SiR, 2 mM $Na_2SO_3^{2-}$, 0.4 units of cysteine synthase, O-acetyl serine, and 10 µM (Fig. 1D) or 20 µM Fd (Fig. 1F). SiR reduction was initiated by an intermolecular electron transfer from Fd, which was reduced by $Na_2S_2O_4$. Reduced SiR sequentially converted sulfite to sulfide. Cysteine synthase, in the presence of O-acetyl serine, produced cysteine from sulfide. The reaction was stopped 0, 3, 6, and 9 min after reducing SiR by the addition of trichloroacetic acid at a final concentration of 20% (v/v). The solution was promptly centrifuged at 15,000 rpm for 3 min and 150 µl of the supernatant was collected. After the addition of 150 µl acetic acid and 150 µl acid-ninhydrin reagent to the supernatant, the solution was heated at 95 °C for 10 min. The addition of 450 µl ethanol to the solution allowed the production of cysteine to be monitored by increases in absorption intensity at 546 nm. Specific activity was obtained by the slope of time-dependent activity at each incubation time.

2.4. Circular dichroism (CD) measurements

All CD measurements of Fd solutions were performed in 50 mM Tris–HCl buffer (pH 7.5) using a J720 spectropolarimeter (Jasco, Japan) at 25 °C. Far-UV CD spectra at 0.2 mg ml^{-1} Fd (~20 µM) were recorded using a quartz cuvette with a 1-mm path length. Near-UV and visible CD spectra with 1 mg ml^{-1} Fd (~100 µM) were obtained using a quartz cuvette with a 1-cm path length. Spectra were expressed as mean residue ellipticity, [θ] (deg cm^2 dmol^{-1}), after subtracting the solvent background.

2.5. Isothermal titration calorimetry (ITC) measurements

Protein solutions were dialyzed against 50 mM Tris–HCl (pH 7.5) and degassed for 3 min before being loaded into the calorimeter. Calorimetric experiments were performed with a VP-ITC instrument (GEHealthcare Biosciences, USA) at 288, 293, 298, and 303 K. In the injection syringe, 1 mM FNR was titrated into 50 μM wild-type or mutant Fds in the ITC cell. Titration experiments consisted of 40 injections spaced at intervals of 400–500 s. The injection volume was 7 μl and the cell was continuously stirred at 264 rpm [3].

Observed enthalpy changes (ΔH_{bind}) for binding and the dissociation constant (K_{d}) were directly calculated from the integrated heat using the one-set of independent binding sites model supplied by the MicroCal Origin 7.0 software. The equation of this binding model was:

$$Q=\frac{\mathrm{n}[P]_{\mathrm{t}}\Delta H_{\mathrm{bind}}V_0}{2}\left[1+\frac{L_{\mathrm{R}}}{\mathrm{n}}+\frac{K_{\mathrm{d}}}{\mathrm{n}[P]_{\mathrm{t}}}-\sqrt{\left(1+\frac{L_{\mathrm{R}}}{\mathrm{n}}+\frac{K_{\mathrm{d}}}{\mathrm{n}[P]_{\mathrm{t}}}\right)^2-\frac{4L_{\mathrm{R}}}{\mathrm{n}}}\right]$$

Equation (2)

where Q is the change in heat in the system, V_0 is the effective volume of the calorimeter cell (1.43 ml), L_{R} is the ratio of the total Fd concentration to total FNR concentration ($[\mathrm{P}]_{\mathrm{t}}$) at any given point during the titration, and n is the binding stoichiometry of Fd per FNR. Using ΔH_{bind} and K_{d}, the observed Gibbs energy change for binding (ΔG_{bind}) and observed

$$\Delta G_{\mathrm{bind}}=RT\ln K_{\mathrm{d}}$$

Equation (3)

$$\Delta G_{\mathrm{bind}}=\Delta H_{\mathrm{bind}}-T\Delta S_{\mathrm{bind}}$$

Equation (4)

where R is the gas constant and T is the temperature in Kelvins.

2.6. Solution NMR measurements of FNR

FNR samples uniformly labeled with ^{15}N were prepared using 50 mM Tris–HCl buffer (pH 7.5) containing 10% D_2O for ^{1}H–^{15}N heteronuclear single quantum correlation (HSQC) measurements. All HSQC spectra of 0.2 mM ^{15}N-labeled FNR in the absence and presence of 0.4 mM wild-type or mutant Fd (S43W and S43D) were obtained at 25 °C in an AVANCE-III H/D 800 spectrometer equipped with a cryogenic probe (Bruker BioSpin, Germany). Data were processed by NMRPipe and analyzed by Sparky [31].

A chemical shift perturbation ($\Delta\delta_{tot}$) in the cross-peaks of FNR by the addition of Fd was calculated using the relationship:

$$\Delta\delta_{tot} = \left[(\Delta\delta_{H}) + (\Delta\delta_{N} \times 0.158)^{2}\right]^{0.5}$$

Equation (5)

where $\Delta\delta_H$ and $\Delta\delta_N$ are the changes in the ^{1}H and ^{15}N chemical shifts in ppm, respectively. The weighting factor of 0.158 was used to adjust the relative magnitudes of the amide nitrogen chemical shift range and amide proton chemical shift range.

2.7. Computational docking simulation between FNR and Fd

Homology modeling of S43W- (S43W) and S43D-substituted Fd (S43D) was performed using the Modeller program v9.11 and crystal structure of wild-type Fd (PDB/3B2F) [12] for a template structure. The qualities of the modeled structures of the Fd mutants were con- firmed using the VERIFY3D program [32].

The docking simulation between Fd (wild-type, S43W, or S43D) and FNR was performed using the HADDOCK easy interface server with semi-flexible refinements. Active residues for interaction restraints were defined based on the chemical shift perturbation data observed in our present and previous NMR studies [33] and were filtered for the accessible surface area calculated by VARDAR (version 1.8) [34]. The active residues of Fd and FNR obtained are listed in Table S1. Passive residues were defined automatically around the active residues. A total of 40 possible Fd:FNR complexes were obtained (see the Supplementary data section).

3. Results

3.1. Interface mutations differentially affected enzymatic activity between FNR and SiR

In order to examine the contribution of hydrophobic forces around serine 38 to 46 on the interface of Fd for FNR and SiR to enzymatic activities, I constructed six Fd mutants in which hydrophobicity was increased (S38W, R40W, A41W, S43W, S45W, and S46W) on the basis of our previous FNR-bound Fd structure (Fig. 1A and B), and performed FNR and SiR activity assays (Fig. 1C and D).

The mutants exhibited various activity changes. The SiR and FNR activities of R40W and S43W mutants were opposite (here designated as a partner enzyme-dependent activity change): R40W and S43W mutants exhibited an increase and decrease in SiR activity (Fig. 1D) and a decrease and increase in FNR activity (Fig. 1C), respectively. No recognizable activity changes were observed among the other mutants; however, the FNR activity of the S46W mutant increased (Fig. 1C).

Based on the largest change in activities depending on enzymes, high conservation in higher plants (Fig. S1), and locational importance for electron transfer between the [2Fe–2S] cluster in Fd and FAD in FNR, we focused on mutagenic analyses of serine 43. In order to obtain a more general insight into the effects of physicochemical properties on enzymatic activity, more Fd mutants were prepared in terms of hydrophobic and electrostatic natures: S43L, S43H, S43F, S43Y, and S43D.

The hydrophobic mutants, S43F, S43Y, and S43W, exhibited marked increases in FNR activities, whereas that of the S43D mutant was markedly decreased by increases in acidity, and the remaining mutants did not show significant activity changes (Fig. 1E). The SiR activities of the S43H, S43F, and S43Y mutants decreased and that of S43W was markedly reduced. However, no significant activity changes were observed with the S43L and S43D mutants (Fig. 1F).

3.2. NADPH-dependent FNR activity using wild-type and mutant Fds

I measured the steady-state kinetics of reductions in cytochrome c in order to determine the effects of site-directed mutations in Fd on FNR activity. I selected the two mutants, S43W and S43D because their enzyme activities markedly differed in a partner enzymedependent manner, i.e., a partner enzyme-dependent activity change (Fig. 1E and F). The

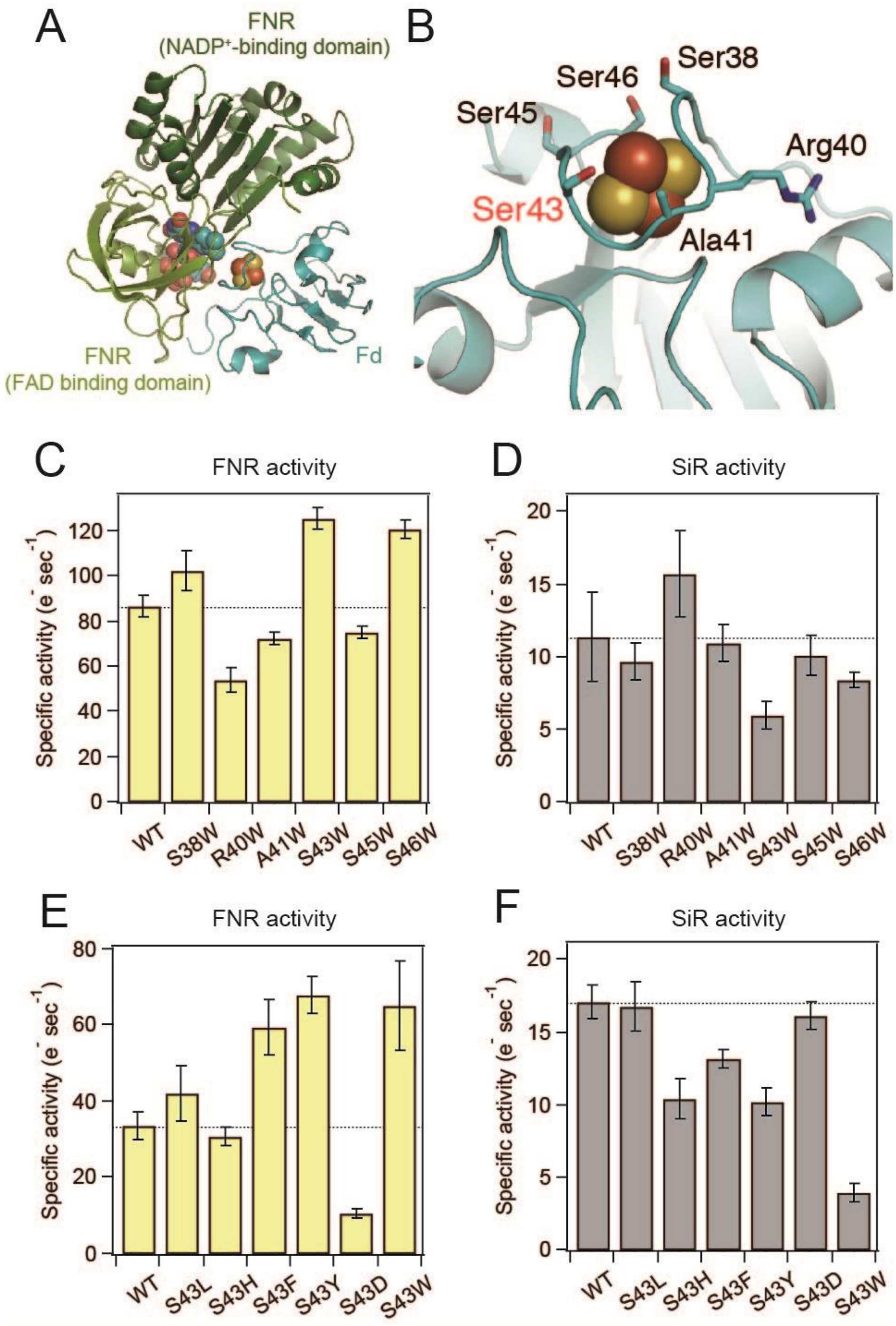

Fig. 1. Structure-based mutagenesis of Fd and enzymatic activity.

(A–B) The structure of the Fd:FNR complex (PDB /1GAQ) (A) and position of Fd residues for mutations (B) are shown. FNR and Fd are displayed in green and light blue colors, respectively. FAD- and NADP⁺-binding domains are shown in light and dark green, respectively. Red and yellow spheres in Fd represent iron and sulfur, respectively. Magenta sticks in FNR indicate FAD. (C–F) The results of the activity assay for FNR (C, E) and SiR (D, F) are shown with bar graphs.

maximum velocity (*v*) for reductions in cytochrome c at various concentrations of wild-type Fd was saturated at a low Fd concentration (less than 5 μM) at 298 K (25 °C) (Fig. 2A), indicating steadystate kinetics with the formation of the Fd:FNR complex. Thus, data were fit using the Michaelis–Menten equation (see the Materials and Methods section). The Michaelis constant (K_m) and turnover number (k_{cat}) were 2.1 μM and 53.5 s^{-1}, respectively (Table 1). The results obtained for the two variants also showed Michaelis–Menten kinetics. Although no significant changes were observed in k_{cat}, K_m values increased to 0.8 μM for S43W and 9.0 μM for S43D (Table 1).

The temperature dependence of kcat was then examined. The kcat values with wild-type Fd increased from 37.8 to 72.5 s^{-1} with elevations in temperature from 288 to 303 K (15 to 30 °C) (Fig. 2B and Table 1). The k_{cat} values with Fd variants showed a very similar temperature dependence to wild-type Fd. Accordingly, activation energy (E_a), which was deduced from the Arrhenius equation, was similar regardless of the types of Fds (Fig. 2C and Table 1). On the other hand, although the K_m values for wild-type and S43W Fds did not show a notable dependency on temperature, that for S43D varied in an opposite manner to the temperature increase (Fig. 2D and Table 1).

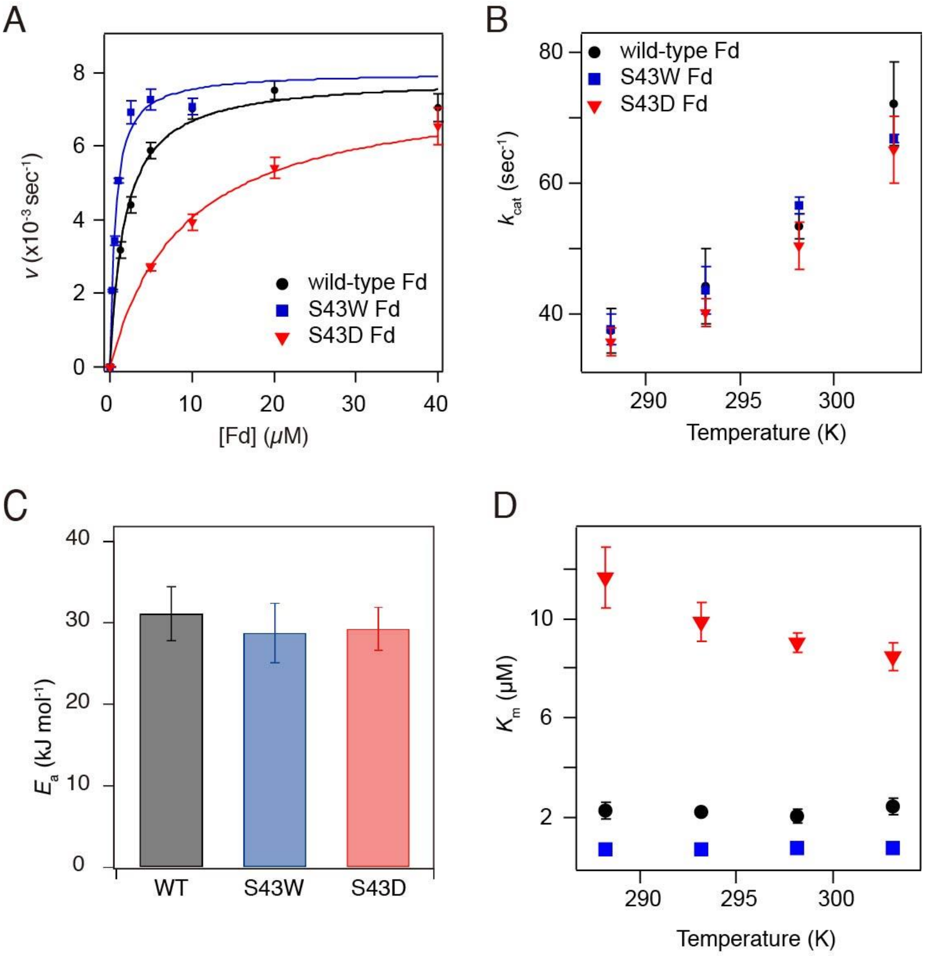

Fig. 2. FNR activity depended on mutations and temperature.

(A) The steady-state kinetics of FNR based on the reduction of cytochrome c at 298 K (25 °C) are shown. The concentrations of wildtype Fd used were 1.25, 2.5, 5, 10, 20, and 40 μM while those of S43W Fd were 0.25, 0.5, 1, 2.5, 5, and 10 μM. S43D Fd was used at concentrations of 5, 10, 20, and 40 μM. The continuous lines indicate the fitting curves based on the Michaelis–Menten equation. (B) k_{cat} values were plotted against temperature. (C) Schematic bar presentations of activation energies (E_a). (D) Temperature dependence of K_m values. Values corresponding to wide-type, S43W, and S43D Fds are shown in black, blue, and red, respectively

Table 1. Summary of various parameters of FNR enzymatic activity obtained by steady-state kinetics. The average and error values were obtained from measurements in triplicate.

Temperature (K)	Wild-type Fd		S43W Fd		S43D Fd	
	K_m (μM)	k_{cat} (s^{-1})	K_m (μM)	k_{cat} (s^{-1})	K_m (μM)	k_{cat} (s^{-1})
288	2.3 ± 0.3	37.8 ± 3.5	0.7 ± 0.0	37.8 ± 2.4	11.6 ± 1.2	35.9 ± 2.2
293	2.2 ± 0.2	44.7 ± 5.8	0.7 ± 0.0	43.9 ± 3.6	9.9 ± 0.8	40.5 ± 2.2
298	2.2 ± 0.3	53.5 ± 1.8	0.8 ± 0.0	56.8 ± 1.4	9.0 ± 0.4	50.7 ± 3.6
303	2.4 ± 0.3	72.5 ± 6.4	0.8 ± 0.1	66.9 ± 0.5	8.5 ± 0.5	65.5 ± 5.0
E_a (kJ mol^{-1})	31.1 ± 3.3		28.7 ± 3.7		29.3 ± 2.6	

3.3. Investigation of structural changes in Fd mutants by various spectroscopies

I demonstrated whether structural changes were caused by substitution mutations using CD and absorption spectroscopy. In CD spectroscopy, I performed measurements at three regions of wavelengths: far-UV (195–250 nm) to examine the secondary structure (Fig. S2A), near-UV (250–300 nm) for the structure near aromatic residues (Fig. S2B), and visible (300–600 nm) regions for [2Fe–2S] for environment-containing clusters (Fig. S2C).

No significant changes were observed in the far-UV CD spectra of the three types of Fds (wild-type, S43W, and S43D), which indicated that the content of alpha helices, beta strands, and random coils was constant in all Fd variants. In the near-UV region, no significant differences were noted in the CD spectra among Fds. Only slight changes were observed in the visible-spectra near 500, 375, and 325 nm. This result indicated that appreciable geometry changes did not occur around the [2Fe–2S] clusters, which was further supported by absorbance spectra. Each of the absorbance spectra of the Fd variants was similar, except for the region near 280 nm of S43W (Fig. S2D), and was mainly attributed to the substitution of tryptophan, showing absorption near 280 nm.

I defined the mutation effects on Fd structures negligible for activities between FNR and each Fd variant. However, I did not exclude the possibility that mutations may have caused changes in midpoint potentials in free Fd and/or FNR-bound Fd that may, in turn, have affected activities. A previous study reported that a mutation in S47A in Anabaena Fd, which corresponded to S45 in maize Fd, markedly affected the midpoint redox potential and rate of FNR reduction [35].

3.4. Thermodynamic characterization of Fd:FNR interactions monitored by calorimetry

I performed ITC measurements using three types of Fds (wild-type, S43W, and S43D) and FNR (Fig. 3) in order to examine thermodynamically interprotein interactions between Fd and FNR at the molecular level in solution.

The titration of wild-type Fd to FNR at 298 K showed a series of positive heat peaks, which indicated complex formation with heat uptake (Fig. 3A) and was consistent with our previous findings [3]. The change in enthalpy (ΔH_{bind}) was calculated as 32.6 kJ mol^{-1} based on an integration of the peak area (Table 2). The positive ΔH_{bind} value displayed energetically unfavorable endothermic binding reactions. The dissociation constant (K_d) obtained by fitting to the binding isotherm (see the

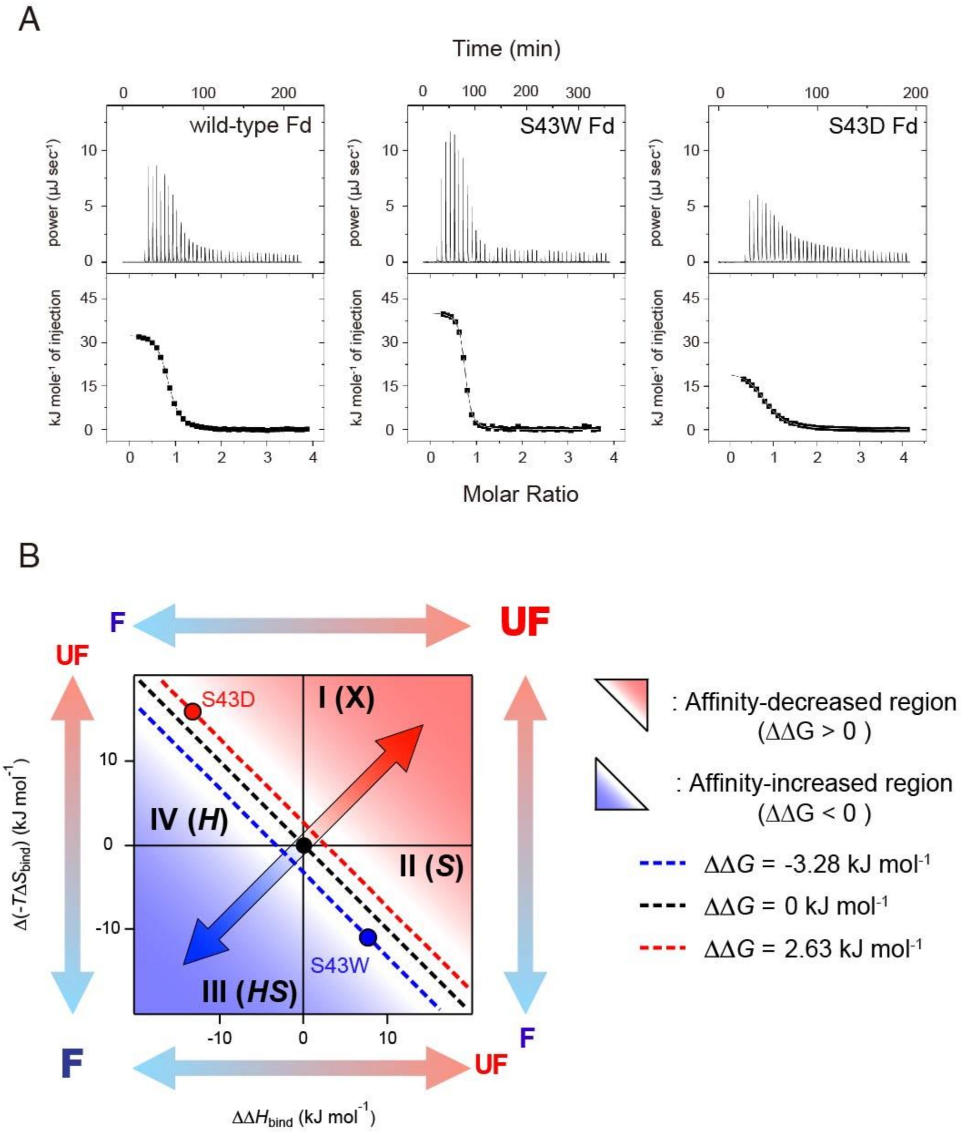

Fig. 3. Thermodynamic characterization of binding reactions between Fd and FNR using ITC and a driving force plot.

(A) ITC thermograms of the titration of wild-type Fd (left), S43W Fd (middle), and S43D Fd (right) to FNR are shown in the upper panel. Normalized heat values were plotted against the molar ratio ([Fd]/[FNR]) in the lower panel. Fitted curves are exhibited using continuous lines. (B) Changes in the driving force (ΔH_{bind} and $-T\Delta S_{\mathrm{bind}}$) and ΔG_{bind} value after the formation of each complex are shown. The broken diagonal lines in black, red, and blue signify the $\Delta\Delta G_{\mathrm{bind}}$ lines of 0, 2.63, and −3.28 kJ mol^{-1}, respectively. Thermodynamically favorable and unfavorable directions on mutation are guided by blue arrows and "F" and red arrows and "UF", respectively, in and out of the panel. The blue and red triangular regions indicate increases and decreases in affinity. Transverse and longitudinal axes indicate $\Delta\Delta H_{\mathrm{bind}}$ and $\Delta(-T\Delta S_{\mathrm{bind}})$, respectively. The black sphere indicates no change in ΔG_{bind} (i.e., $\Delta\Delta G_{\mathrm{bind}} = 0$). Red and blue spheres show $\Delta\Delta G_{\mathrm{bind}}$ following changes in ΔG_{bind} with the mutation of serine at 43 to tryptophan (i.e., S43W) or aspartic acid (i.e., S43D), respectively. The four rectangular regions were classified by driving forces: region "I" (upper right), region "II" (lower right), region "III" (lower left), and region "IV" (upper left). In each region, a thermodynamically favorable driving force is indicated in parentheses. "I(X)" represents no driving force for favoring binding reactions.

Materials and Methods section) was 1.0 ± 0.1 μM (Table 2), which was similar to the value of K_{m} (Fig. S3A). The n value of approximately 0.8 suggested one-to-one binding stoichiometry between Fd and FNR. By using thermodynamic relationships, I obtained changes in free energy (ΔG_{bind}) and entropy ($-T\Delta S_{\mathrm{bind}}$) (Table 2). Negative ΔG_{bind} (−34.2 ± 0.2 kJ

mol^{-1}) and $-T\Delta S_{\text{bind}}$ (-66.8 ± 0.4 kJ mol^{-1}) indicated spontaneous Fd:FNR complex formation driven purely by positive ΔS_{bind}.

ITC measurements at 298 K were performed for S43W and S43D and endothermic binding heat was also detected (Fig. 3A). The thermodynamic and physical parameters analyzed (ΔH_{bind}, K_d, ΔG_{bind}, $-T\Delta S_{\text{bind}}$, and n) were summarized in Table 2. K_d values were similar to K_m: the K_d values of S43W (0.3 ± 0.1 μM) and S43D (3.0 ± 0.4 μM) were lower and higher than that of wildtype Fd (1.0 ± 0.1 μM), respectively (Fig. S3A). Therefore, the order of ΔG_{bind} was S43D (-31.6 ± 0.3 kJ mol^{-1}) > wild-type (-34.2 ± 0.2 kJ mol^{-1}) > S43W (-37.5 ± 0.7 kJ mol^{-1}) (Fig. S3B). The complex formation of FNR with Fd variants was also only favored by the positive entropy change (Fig. S3B). The ΔH_{bind} value was in the order of S43W (40.3 ± 0.5 kJ mol^{-1}) > wild-type (32.6 ± 0.2 kJ mol^{-1}) > S43D (19.4 ± 0.2 kJ mol^{-1}), and S43D (-51.0 ± 0.2 kJ mol^{-1}) > wild-type (-66.8 ± 0.4 kJ mol^{-1}) > S43W (-77.8 ± 0.3 kJ mol^{-1}) for the $-T\Delta S_{\text{bind}}$ value.]

3.5. Temperature dependence of thermodynamic parameters for Fd:FNR complexation

The thermodynamic properties of interprotein interactions are a function of temperature. Thus, temperature-dependent changes in thermodynamic parameters reflect the influences of physicochemical properties on intermolecular interactions.

Therefore, I examined changes in various thermodynamic parameters for the interactions between wild-type Fd and FNR in the range of 288 to 303 K (15 to 30 °C) (Fig. 4). K_d values decreased from 1.5 ± 0.4 to 0.9 ± 0.2 μM with an increase in temperature from 288 to 303 K (15 to 30 °C) (Table 2). As observed for K_m values, K_d values also decreased from 1.5 ± 0.4 to 0.9 ± 0.2 μM with increases in temperature from 288 to 303 K (15 to 30 °C) (Table 2), indicating an increase in interprotein affinity with a decrease in ΔG_{bind} by -3.1 kJ mol^{-1} (Fig. 4A). ΔH_{bind} and $-T\Delta S_{\text{bind}}$ both became gradually favorable with increases in temperature from 32.1 ± 0.6 kJ mol^{-1} at 288 K (25 °C) to 30.7 ± 0.0 kJ mol^{-1} at 303 K (30 °C) and from -64.2 ± 0.1 kJ mol^{-1} at 288 K (25 °C) to -65.9 ± 0.6 kJ mol^{-1} at 303 K (30 °C), respectively. These results revealed that the two energetic terms were stabilizers for the Fd:FNR complex regardless of the temperatures examined here.

Table 2. Summary of various thermodynamics parameters of complex formation between Fd and FNR obtained by ITC. The average and error values were obtained from measurements in duplicate.

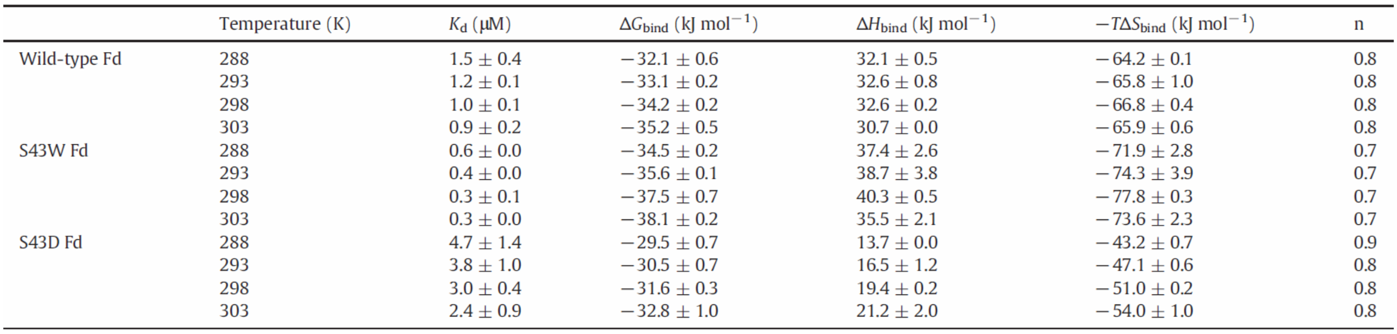

	Temperature (K)	K_d (μM)	ΔG_{bind} (kJ mol^{-1})	ΔH_{bind} (kJ mol^{-1})	$-T\Delta S_{\text{bind}}$ (kJ mol^{-1})	n
Wild-type Fd	288	1.5 ± 0.4	-32.1 ± 0.6	32.1 ± 0.5	-64.2 ± 0.1	0.8
	293	1.2 ± 0.1	-33.1 ± 0.2	32.6 ± 0.8	-65.8 ± 1.0	0.8
	298	1.0 ± 0.1	-34.2 ± 0.2	32.6 ± 0.2	-66.8 ± 0.4	0.8
	303	0.9 ± 0.2	-35.2 ± 0.5	30.7 ± 0.0	-65.9 ± 0.6	0.8
S43W Fd	288	0.6 ± 0.0	-34.5 ± 0.2	37.4 ± 2.6	-71.9 ± 2.8	0.7
	293	0.4 ± 0.0	-35.6 ± 0.1	38.7 ± 3.8	-74.3 ± 3.9	0.7
	298	0.3 ± 0.1	-37.5 ± 0.7	40.3 ± 0.5	-77.8 ± 0.3	0.7
	303	0.3 ± 0.0	-38.1 ± 0.2	35.5 ± 2.1	-73.6 ± 2.3	0.7
S43D Fd	288	4.7 ± 1.4	-29.5 ± 0.7	13.7 ± 0.0	-43.2 ± 0.7	0.9
	293	3.8 ± 1.0	-30.5 ± 0.7	16.5 ± 1.2	-47.1 ± 0.6	0.8
	298	3.0 ± 0.4	-31.6 ± 0.3	19.4 ± 0.2	-51.0 ± 0.2	0.8
	303	2.4 ± 0.9	-32.8 ± 1.0	21.2 ± 2.0	-54.0 ± 1.0	0.8

The binding of S43W to FNR showed similar temperature responses to those of wild-type Fd. However, the temperature dependence of ΔH_{bind} and $-T\Delta S_{\mathrm{bind}}$ for S43D binding was markedly different. ΔH_{bind} values markedly increased from 13.7 ± 0.0 kJ mol^{-1} at 288 K (25 °C) to 21.2 ± 2.0 kJ mol^{-1} at 303 K (30 °C) (Fig. 4C), whereas and $-T\Delta S_{\mathrm{bind}}$ values markedly decreased from −43.2 ± 0.7 kJ mol^{-1} at 288 K (25 °C) to −54.0 ± 1.0 kJ mol^{-1} at 303 K (30 °C) (Fig. 4B).

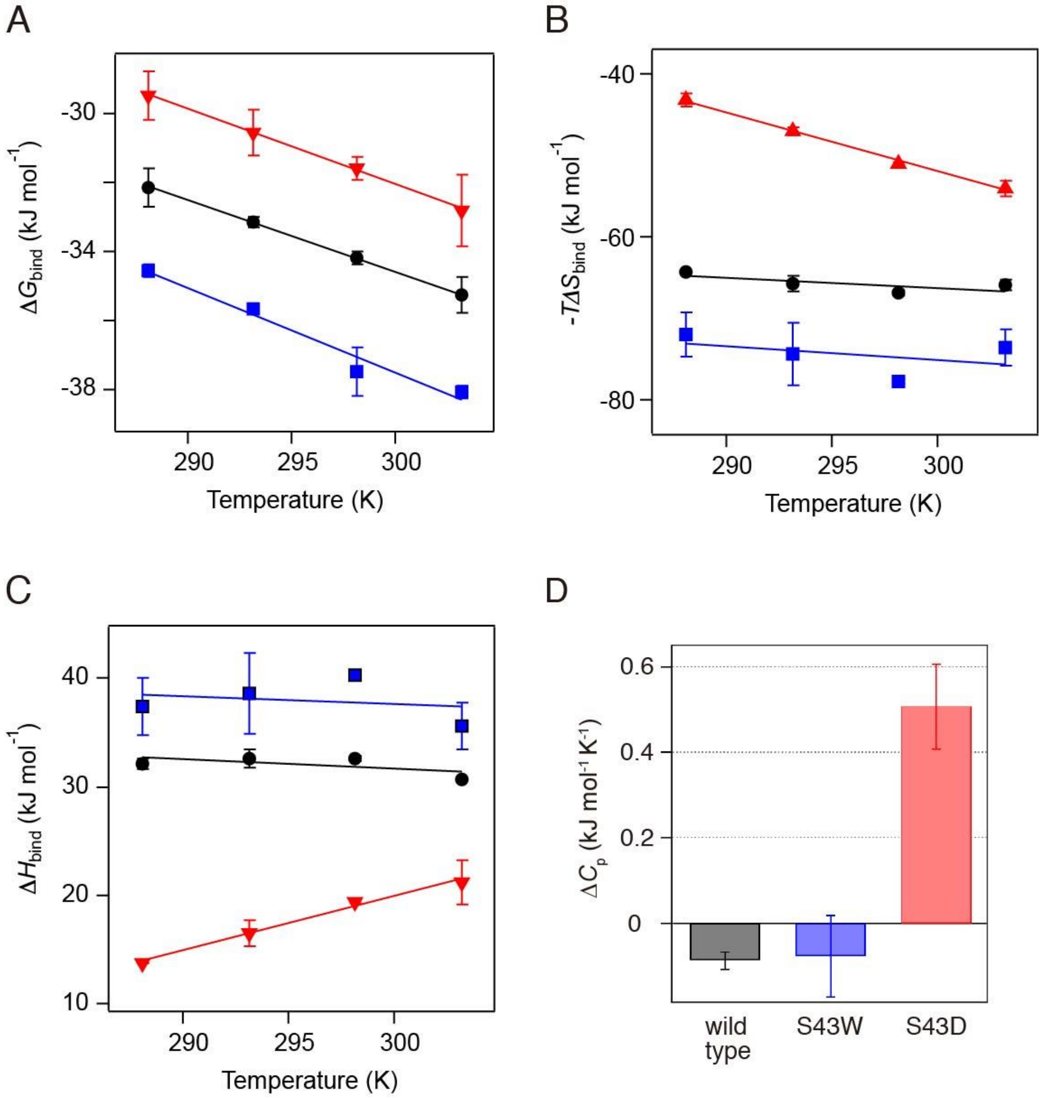

Fig. 4. Temperature-dependent thermodynamic parameters.

(A–C) The values of ΔG_{bind} (A), $-T\Delta S_{\mathrm{bind}}$ (B), and ΔH_{bind} (C) were plotted as a function of temperature. (D) The ΔC_{p} values of wild-type, S43W, and S43D Fds are shown. Thermodynamic parameters for FNR binding to wild-type, S43W, and S43D Fds are shown in black, blue, and red, respectively.

The change in heat capacity (ΔC_{p}) was obtained from the slope of the temperature dependence of ΔH_{bind} (i.e., $\partial\Delta H_{\mathrm{bind}}/\partial T$). Although the ΔC_{p} values of wild-type and S43W binding to FNR were similar to each other, that of S43D binding was largely distinct. The ΔC_{p} values for the binding of wild-type Fd, S43W, and S43D to FNR were −87, −76, and 507 J mol^{-1} K^{-1} , respectively (Fig. 4D and Table 2).

No clear decrease was observed in K_{m} for wild-type and S43W Fds with increases in temperature (Table 1); however, increases in temperature led to reductions in K_{d} for all three types of Fds (Table 2). Although the underlying mechanism and

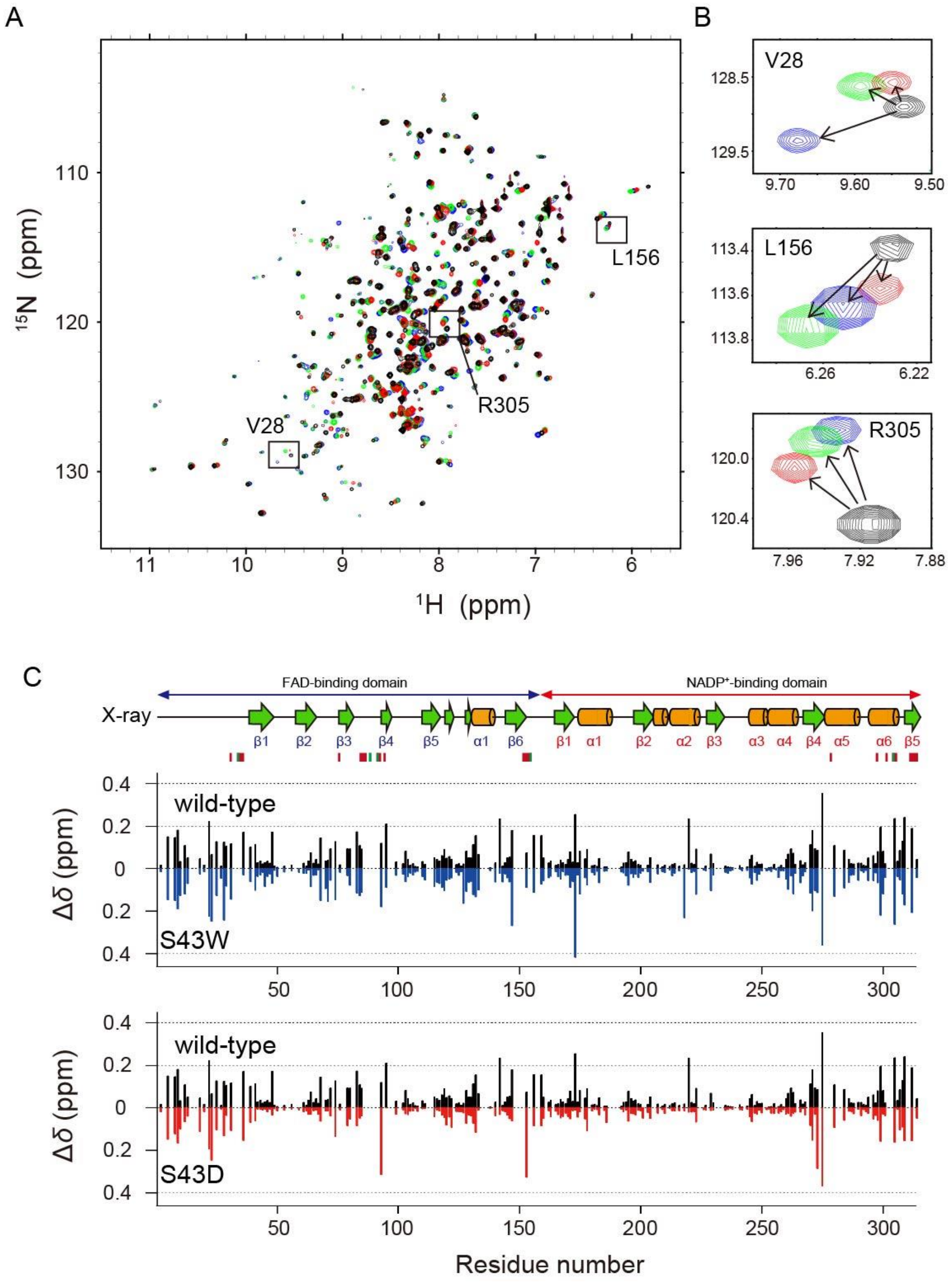

Fig. 5. NMR spectroscopy of 15N-labeled FNR with and without Fd and chemical shift perturbation analyses. (A) The superposition of ^{1}H–^{15}N HSQC spectra of FNR without Fd (black) and with wild-type (green), S43W (blue), or S43D Fds (red). (B) Shifts in the peak (V28, L156, and R305) are representatively magnified. (C) Chemical shift perturbations with the addition of each type of Fd were plotted against the residue number of FNR. The secondary structure elements determined from the X-ray structure (PDB/1GAW) are displayed in the top part. Alphahelices and beta-strands are colored in orange and green, respectively. The residues of FNR interacting with Fd are shown by the colored rectangles below the secondary structure elements. Green and red indicate positively-charged and non-charged residues, respectively

reason for these discrepancies remain unclear, the physical binding properties of K_d between complexes and free proteins directly obtained by the thermodynamic measurement of ITC may not be always consistent with K_m obtained from Michaelis–

Menten kinetics depending on changes in temperature. The components present in reconstituted activity assay systems, but absent in ITC measurement systems, such as cytochrome *c*, may be involved in distinct responses between K_d and K_m at different temperatures. Alternatively, the distinct approaches utilized produced different values to some extent, which is often observed in K_d values obtained by different methods such as ITC, NMR, and surface plasmon resonance [36,37].

3.6. Residue-based investigation of Fd–FNR interactions using NMR spectroscopy

In order to obtain more detailed information on the binding mode and interfaces of FNR for Fds at the residue level, two-dimensional ^{1}H–^{15}N HSQC measurements on uniformly-labeled FNR with ^{15}N were performed in the absence and presence of Fds (wild-type, S43W, and S43D) (Fig. 5A).

The NMR cross-peaks of FNR in the absence of Fd were sharp and widely dispersed, which indicated the well-folded state of FNR. Based on the K_d values obtained from ITC measurements, the amounts of Fd added were 2-fold that of FNR in order to saturate FNR with Fd. The population of each Fd:FNR complex was close to 100%. The addition of each Fd changed a large number of the NMR peak positions of FNR without significantly altering the number of peaks in the absence of Fds (Fig. 5A). This result indicated the formation of individual Fd:FNR complexes and a fast exchange regime of interactions between each Fd and FNR.

Although the direction of changes in peak shifts depended on the types of Fd (Fig. 5B), the overall perturbed regions of FNR were all similar, as shown by the plot of the chemical shift perturbation (CSP) (Fig. 5C) and mapping of CSP values on a crystal structure of FNR (Fig. S4). These results were consistent with our previous findings [18]. Perturbed residues were mainly located in the N-terminal and β2–β3 (around K88 and K91) regions on the FAD-binding domain, the interdomain region around D154, and the β1–α1 (around G173), β4–α5 (around K275), and C-terminal (around K304) regions on the NADP^{+}-binding domain, which is in accordance with those suggested by the crystal structure of the wild-type Fd:FNR complex [22]. The hydrophobic residues of I68, V83, I147, and L156 and polar residues of T29, Q74, and C132 also showed perturbations.

The representative residues that showed large perturbations regardless of the types of Fd were in the N- and C-terminal regions and also in the β4–α5 region around K275. R93 and K153 of FNR in the presence of S43D showed larger CSP values than those in the presence of wild-type Fd.

4. Discussion

4.1. Importance of hydrophobic and electrostatic residues of Fd for activities of partner enzymes

The electrostatic interaction between Fd and a partner enzyme has predominantly been reasoned as a key contributor to the efficient activity of a partner enzyme. However, I questioned this interpretation because the buried nonpolar surface area of the Fd:FNR complex was previously shown to account for approximately 50% of the total buried apolar surface area [22]. Therefore, I focused on the effects of the physicochemical properties of interfacial residues around the [2Fe–2S] cluster from the viewpoint of enzyme activity by addressing hydrophobic and electrostatic contributions.

Partner enzyme-dependent activity changes in most of the tryptophan mutants, except for S45W (Fig. 1C and D), demonstrated that hydrophobic interactions on binding interfaces around S38 to S46 of Fd, which have not received much attention, were essential for the regulation of FNR and SiR activities. A set of S43 mutants also showed the contribution of hydrophobic forces to changes in activity depending on partner enzymes. A similar finding was also reported in the plant-type photosynthetic electron transport ferredoxin (PETF) [17]. The PETF mutants, D19A and D58A, exhibited the differential recognition and activity between FNR and hydrogenase HYDA1.

Partner enzyme-dependent activity changes in S43 mutants (S43H and S43D) provided further insights into electrostatic contributions (Fig. 1E and F). S43H, which increased the repulsive charge–charge interaction with Fd, decreased SiR activity, but had no effects on FNR activity. In contrast to the general expectation that attractive electrostatic interactions increase activity, S43D exhibited a decrease in FNR activity without a change in SiR activity.

Taken together, our results suggested that activity changes were not always predictable by the general electrostatic contribution alone, and the physicochemical properties of hydrophobic and electrostatic residues on interprotein interfaces were important in the regulation of FNR and SiR activities.

4.2. Interprotein interactions dominated FNR activity

The overall activity of FNR comprised physical processes including intermolecular interactions among Fd, FNR, and the substrate of $NADP^+$ as well as the chemical reactions of electron and hydride transfer.

In order to identify the dominant factor regulating FNR activity, I introduced a site-directed mutation to Fd because a

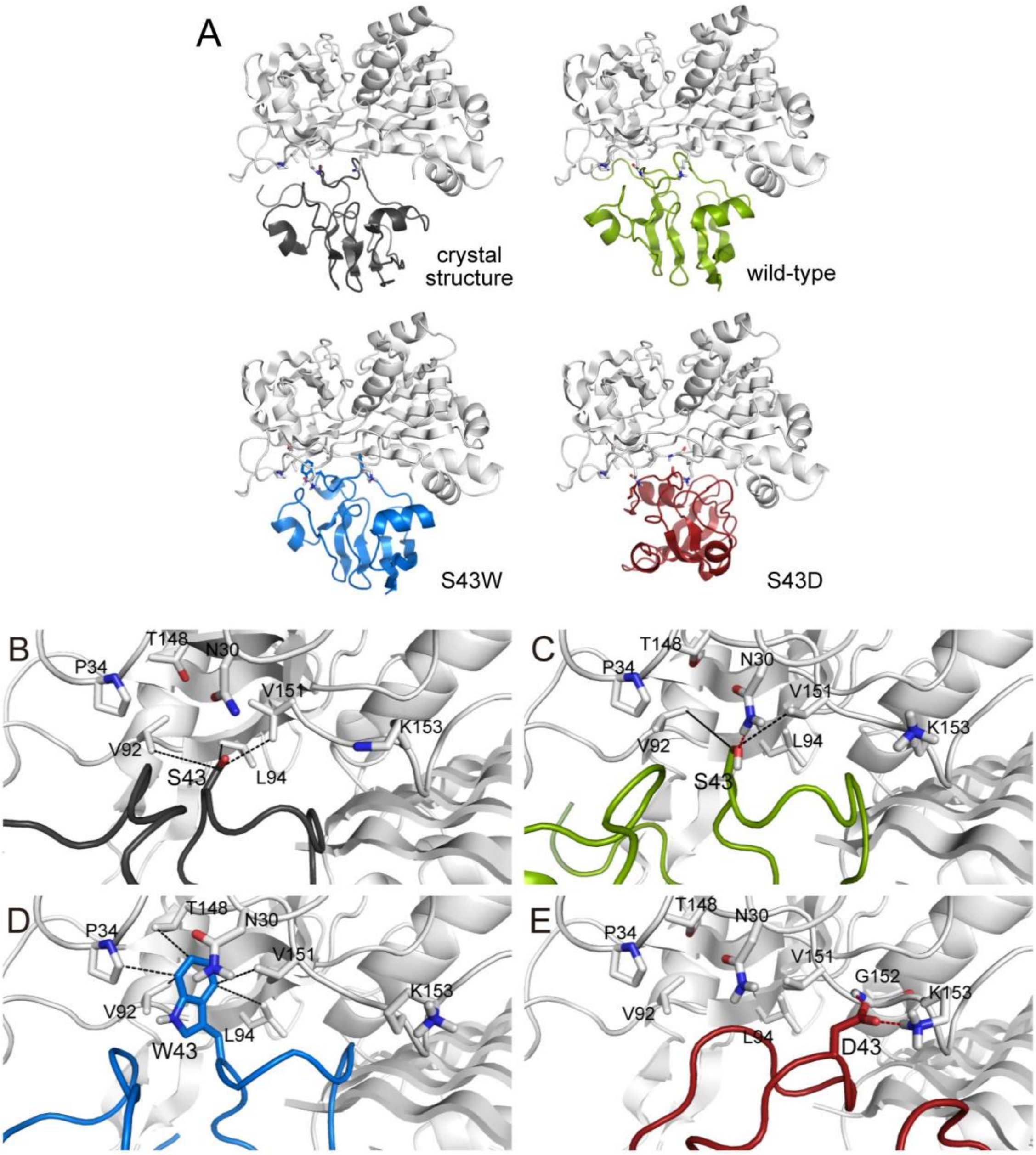
A
crystal structure
wild-type
S43W
S43D
B
T148
N30
P34
V151
K153
V92
S43
L94
C
T148
N30
P34
V151
K153
V92
L94
S43
D
T148
N30
P34
V151
K153
V92
L94
W43
E
T148
N30
P34
V151
G152
K153
V92
L94
D43

Fig. 6. Modeled Fd:FNR complexes and their binding interfaces.

(A) The complex structures of wild-type Fd and FNR determined by X-ray crystallography and three docking simulation structures with HADDOCK in combination with NMR data are shown. Each complex, which showed the lowest energy, was selected from 40 complexes. FNR is colored in gray. Wild-type, S43W, and S43D Fds are shown in green, blue, and red, respectively. Magenta sticks in FNR indicate FAD. Red and yellow spheres in Fd represent iron and sulfur, respectively. The distance between FAD and iron guided by the broken line is shown in parentheses. (B, C) Interprotein surfaces between FNR and wild-type Fd determined by X-ray crystallography (B) and a docking simulation with HADDOCK in combination with NMR data (C) are magnified for comparisons. (D, E) The interacting surfaces between FNR and S43W Fd (D) or S43D Fd (E), as modeled by HADDOCK, are also shown.

mutation in FNR may include changes in the intrinsic catalytic capability of FNR as well as in the intermolecular interaction with Fd and NADP$^+$. By mutating Fd, I expected a simpler system that predominantly reflected a mutation effect stemming from interprotein interactions directly linked to interprotein electron flow from FNR to Fd.

I again selected the two mutants of Fd that displayed the most prominent changes in enzymatic activity (Fig. 1E and F), S43W and S43D. Although no appreciable alternations were observed in the chemical reaction (k_{cat}) or activation energy (E_a) for S43W and S43D (Fig. 2B and C), physical changes identified in K_m indicated that the interprotein interaction was a dominant factor controlling the overall activity of FNR (Fig. 2). The similar dependence of changes in enzymatic activities due to interprotein interactions was observed in other electron transfer proteins. I previously reported that changes in enzymatic activities by the neutralization of acidic residues on the binding surfaces of Fd for SiR [24] and NiR [9] primarily depended on K_m values, not k_{cat} values. Similar findings were also found in cytochrome *c*-related electron transfer and activity assays [38].

Our results and previous findings demonstrated that physicochemical properties at the location of 43 on the interface of Fd were important for determining overall FNR activity by adjusting interprotein interactions between Fd and FNR. Furthermore, I suggested that this concept may be applicable to other enzyme activity studies utilizing electrontransport proteins.

4.3. Fd–FNR interactions under thermodynamic controls

Since physical interactions between Fd and FNR regulated FNR activity and interprotein interactions were fundamentally under thermodynamic control, binding energetics between two proteins were characterized at the molecular level using ITC (Figs. 3 and 4). ITC is one of the most powerful approaches for elucidating the physical, mechanical, and energetic natures of binding systems including molecular association mechanisms, binding modes, and driving forces for complexation [2,3,39].

Complexation-interrupting positive ΔH_{bind} values were detected in all complexes formed as a result of energy costs for the dehydration of charged residues, which drove complex formation solely with entropy (Fig. S3B) [3]. The higher affinity of S43W for FNR than the wild-type was attributed to the gain of entropy (increases in ΔS_{bind}), which overwhelmed the unfavorable enthalpic loss (increases in ΔH_{bind}) (Fig. S3B), as shown in the driving force plot (Fig. 3B). The dehydration of water from hydrophobic regions around the tryptophan residue, i.e., the hydrophobic effect, and electrostatic/polar regions may have largely stabilized the Fd:FNR complex.

The driving force plot rationalized the weakened affinity of S43D for FNR with the loss of $\Delta\Delta G$ = 2.63 kJ mol−1 in terms of the penalty of entropy (Figs. 3B and S3B). The formation of an electrostatic and hydrogen bond network around the negative charge of the aspartic acid at 43 (Fig. 3B) may have engendered favorable contributions to the formation of the

S43D:FNR complex by reducing ΔH_{bind}. Furthermore, since attractive intermolecular interactions have been shown to promote molecular recognition [40], a decrease in affinity may also be kinetically explained by a markedly faster dissociation rate than association rate.

Electrostatic and hydrophobic interactions are a function of temperature. Elevations in temperature are generally accepted to be accompanied by reductions in electrostatic forces and the reinforcement of hydrophobic forces [41,42]. Hence, perturbations to a binding system by changes in temperature support an informative measure of the relative contributions of these two intermolecular forces to complex formation. In all three binding systems, ΔG_{bind} decreased linearly with increases in temperature (Fig. 4A). Furthermore, ΔC_{p}, a thermodynamic indicator of physicochemical properties for the buried surface area, showed small negative values for wild-type Fd:FNR binding and S43W:FNR binding, which demonstrated that the thermodynamic contributions of buried hydrophobic surface areas were slightly more dominant than those of electrostatic/polar surface areas. These results indicated the thermodynamic importance of hydrophobic forces in stabilizing the Fd:FNR complex (Fig. 4D). A positive ΔC_{p} value was obtained for S43D:FNR binding, which was suggestive of the large contribution of the burial of electrostatic/polar surface areas. A positive ΔC_{p} was previously observed in binding reactions between nucleic acids and proteins or in protein misfolding and aggregation due to the burial of charges [43].

Distinct individual thermodynamic parameters for complexation depending on the type of Fds proposed different binding modes and/or orientations of individual Fds to FNR, which were fit toward maximizing energetic merits for physical interactions between proteins under given conditions. Our comprehensive driving force plot showed the capability of proteins for thermodynamic trades based on enthalpy–entropy compensation, which may be one of the properties of evolution pressure (Fig. 3B).

4.4. Interfacial physicochemical properties determined the physical binding mode between Fd and FNR

A residue-based investigation with NMR spectroscopy provided further insights into interprotein interactions. Although the plotting and mapping of CSP indicated the similar binding interfaces of FNR for each Fd (Figs. 5C and S4), the direction of shifts in many peaks such as V28, L156, and R305 differed depending on the type of Fd (Fig. 5B). This was mostly attributed to the distinct strength of hydrogen bonds, backbone dihedral angles, and influences of surrounding residues [44], which reflected an alternative binding mode and/or orientation between proteins.

The visualization of the three Fd:FNR complexes by a docking simulation with the incorporation of the CSP of NMR as a restraint (Fig. 6A) revealed detailed images of binding interfaces (Fig. 6B–E). Binding interfaces between wild-type Fd and

FNR consisted of electrostatic and hydrophobic interactions together with polar interactions including several H-bonds (Fig. 6C). Serine at 43 of Fd formed several hydrogen bonds with the neighboring residues of V92, L94, and V151 of FNR. Although interactions between interfacial residues were similar in solutions (Fig. 6C) and crystals (Fig. 6B), the binding interfaces in solutions were wider to some extent than those in crystals (Figs. 5C and 6A–C), which implicated the more flexible binding of Fd and FNR in solution in favor of matching and tuning courses for a preferable complex conformation.

The binding interface of the S43W:FNR complex showed the insertion of the indole side chain of tryptophan at 43 of Fd to a small binding cavity of FNR through various non-covalent interactions with the side chains of FNR; however, the orientation of Fd differed from that of wild-type Fd (Fig. 6D).

Although interacting sites between the surface of S43D around an aspartic acid at 43 and FNR led to predominant electrostatic interactions (Fig. 6E), the interacting site of FNR for Fd shifted to a more central part of FNR, a loop between the FAD- and NADP$^+$-binding domains, than wild-type Fd and S43W binding. The negative charge of aspartic acid at 43 formed a salt bridge with the positive charge of a lysine residue (K153) and a hydrogen bond with the backbone of a glycine (G152). These intermolecular electrostatic networks provide a clue for the positive value of ΔC_p due to the burial of charges (Fig. 4D).

The orientation between Fd and FNR was appropriate for interprotein electron transfer. The distance between the isoalloxazine ring in FAD and iron in the [2Fe–2S] cluster in each Fd:FNR complex was sufficiently small in all cases (6.3 Å–9.1 Å) (Fig. 6A–D) for electron transfer to not be rate-limiting. These results suggested that the binding mode and orientation of each Fd to FNR were different at the residue level and this physical interprotein binding was changeable through alternations in the physicochemical properties of the interfacial residues of Fd by means of varying electrostatic and hydrophobic natures.

4.5. Thermodynamic and physical balances of non-covalent intermolecular interactions limited FNR activity

I previously demonstrated that the entropic gain from conformational flexibility and dehydration was the only driving force for the complex formation of Fd and FNR under mildly acidic conditions in spite of the formation of five salt bridges [3]. I herein obtained a more detailed rationale by combining biochemical and biophysical approaches as well as an improved understanding of the molecular origins of the regulation of FNR activity.

Large increases in favorable electrostatic interactions may be disadvantageous for the best orientation for intermolecular electron transfer and/or weakened interprotein affinity, thereby decreasing activity, as observed in the binding of S43D with

FNR (Figs. 3B and 6E). On the one hand, large increases in hydrophobicity may promote faster sampling of the conformational space of complex structures by taking advantage of short-range hydrophobic interactions and, in turn, reaching a more optimal complex structure with high stability, thereby enhancing FNR activity by increasing the rate of electron transfer and interprotein affinity (Figs. 2, 3B, and 6D).

Therefore, even a single mutation in a hydrophobic environment without the disruption of Fd integrity is sufficient to limit overall FNR activity through the delicate balance of enthalpy and entropy in the form of non-covalent interactions and dehydration, which determines interprotein affinity and orientation (Fig. 3B). Further systematic studies using SiR and/or SiR and FNR mutants are required to obtain more general conclusions.

I suggest that proteins sensitively cope with changes in environmental conditions and spontaneous mutations in a thermodynamically favorable way to reduce global energy. However, an enzyme responds in a functionally favorable way, including thermodynamics and kinetics.

Supplementary information

Table S1. Active residues of Fd and FNR used for HADDOCK calculations.

	Wild-type Fd:FNR	S43W Fd:FNR	S43D Fd:FNR
Active residues of FNR	A5, V8, E9, A12, K22, E25, V28, T29, L31, E36, V39, R41, I48, I68, E72, Q74, I79, V83, D84, R93, Y95, G106, V131, C132, G142, I147, L156, K159, G173, K220, Y270, M271, C272, K275, G280, Y299, R305, Q308, W309, E312	A5, V8, E9, A10, A12, K22, Q23, E25, V28, L31, R41, I68, Y70, R71, Q74, V83, D84, K85, R93, I119, I127, V128, V131, C132, S133, I147, L156, A175, K218, A223, D230, L261, K263, Y270, M271, C272, G273, K275, G280, Y299, K300, R305, Q308, W309, E312	A5, V8, E9, A10, K18, K22, Q23, E25, V28, L31, E36, Q74, R93, C132, K153, R178, M271, G273, K275, G280, Y299, R305, D307, W309, E312
Active residues of Fd	E30, Y37, S38, C39, R40, A41, S43, D60, S62, Y63, D65, G97, A98	E30, Y37, S38, C39, R40, A41, W43, D60, S62, Y63, D65, G97, A98	E30, Y37, S38, C39, R40, A41, D43, D60, S62, Y63, D65, G97, A98

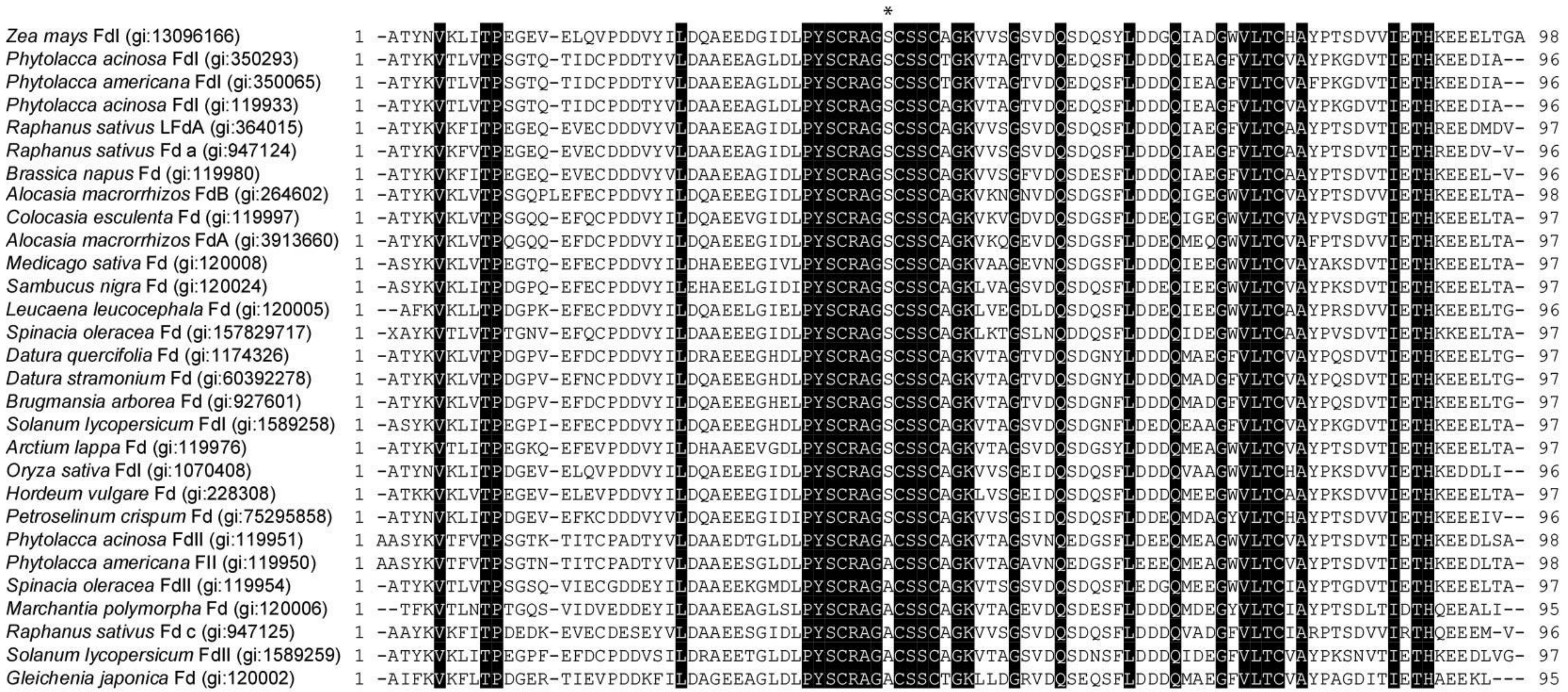

```
                                                                                     *
Zea mays FdI (gi:13096166)             1 -ATYNVKLITPEGEV-ELQVPDDVYILDQAEEDGIDLPYSCRAGSCSSCAGKVVSGSVDQSDQSYLDDGQIADGWVLTCHAYPTSDVVIETHKEEELTGA 98
Phytolacca acinosa FdI (gi:350293)     1 -ATYKVTLVTPSGTQ-TIDCPDDTYVLDAAEEAGLDLPYSCRAGSCSSCTGKVTAGTVDQEDQSFLDDDQIEAGFVLTCVAYPKGDVTIETHKEEDIA-- 96
Phytolacca americana FdI (gi:350065)   1 -ATYKVTLVTPSGTQ-TIDCPDDTYVLDAAEEAGLDLPYSCRAGSCSSCTGKVTAGTVDQEDQSFLDDDQIEAGFVLTCVAFPKGDVTIETHKEEDIA-- 96
Phytolacca acinosa FdI (gi:119933)     1 -ATYKVTLVTPSGTQ-TIDCPDDTYVLDAAEEAGLDLPYSCRAGSCSSCAGKVTAGTVDQEDQSFLDDDQIEAGFVLTCVAYPKGDVTIETHKEEDIA-- 96
Raphanus sativus LFdA (gi:364015)      1 -ATYKVKFITPEGEQ-EVECDDDVYVLDAAEEAGIDLPYSCRAGSCSSCAGKVVSGSVDQSDQSFLDDDQIAEGFVLTCAAYPTSDVTIETHREEDMDV- 97
Raphanus sativus Fd a (gi:947124)      1 -ATYKVKFVTPEGEQ-EVECDDDVYVLDAAEEAGIDLPYSCRAGSCSSCAGKVVSGSVDQSDQSFLDDDQIAEGFVLTCAAYPTSDVTIETHREEDV-V- 96
Brassica napus Fd (gi:119980)          1 -ATYKVKFITPEGEQ-EVECDDDVYVLDAAEEAGIDLPYSCRAGSCSSCAGKVVSGFVDQSDESFLDDDQIAEGFVLTCAAYPTSDVTIETHKEEEL-V- 96
Alocasia macrorrhizos FdB (gi:264602)  1 -ATYKVKLVTPSGQPLEFECPDDVYILDQAEEEGIDLPYSCRAGSCSSCAGKVKNGNVDQSDGSFLDDDQIGEGWVLTCVAYPTSDVVIETHKEEELTA- 98
Colocasia esculenta Fd (gi:119997)     1 -ATYKVKLVTPSGQQ-EFQCPDDVYILDQAEEVGIDLPYSCRAGSCSSCAGKVKVGDVDQSDGSFLDDEQIGEGWVLTCVAYPVSDGTIETHKEEELTA- 97
Alocasia macrorrhizos FdA (gi:3913660) 1 -ATYKVKLVTPQGQQ-EFDCPDDVYILDQAEEEGIDLPYSCRAGSCSSCAGKVKQGEVDQSDGSFLDDEQMEQGWVLTCVAFPTSDVVIETHKEEELTA- 97
Medicago sativa Fd (gi:120008)         1 -ASYKVKLVTPEGTQ-EFECPDDVYILDHAEEEGIVLPYSCRAGSCSSCAGKVAAGEVNQSDGSFLDDDQIEEGWVLTCVAYAKSDVTIETHKEEELTA- 97
Sambucus nigra Fd (gi:120024)          1 -ASYKVKLITPDGPQ-EFECPDDVYILEHAEELGIDIPYSCRAGSCSSCAGKLVAGSVDQSDQSFLDDEQIEEGWVLTCVAYPKSDVTIETHKEEELTA- 97
Leucaena leucocephala Fd (gi:120005)   1 --AFKVKLLTPDGPK-EFECPDDVYILDQAEELGIELPYSCRAGSCSSCAGKLVEGDLDQSDQSFLDDEQIEEGWVLTCAAYPRSDVVIETHKEEELTG- 96
Spinacia oleracea Fd (gi:157829717)    1 -XAYKVTLVTPTGNV-EFQCPDDVYILDAAEEEGIDLPYSCRAGSCSSCAGKLKTGSLNQDDQSFLDDDQIDEGWVLTCAAYPVSDVTIETHKKEELTA- 97
Datura quercifolia Fd (gi:1174326)     1 -ATYKVKLVTPDGPV-EFDCPDDVYILDRAEEEGHDLPYSCRAGSCSSCAGKVTAGTVDQSDGNYLDDDQMAEGFVLTCVAYPQSDVTIETHKEEELTG- 97
Datura stramonium Fd (gi:60392278)     1 -ATYKVKLVTPDGPV-EFNCPDDVYILDQAEEEGHDLPYSCRAGSCSSCAGKVTAGTVDQSDGNYLDDDQMADGFVLTCVAYPQSDVTIETHKEEELTG- 97
Brugmansia arborea Fd (gi:927601)      1 -ATYKVKLVTPDGPV-EFDCPDDVYILDQAEEEGHELPYSCRAGSCSSCAGKVTAGTVDQSDGNFLDDDQMADGFVLTCVAYPQSDVTIETHKEEELTG- 97
Solanum lycopersicum FdI (gi:1589258)  1 -ASYKVKLITPEGPI-EFECPDDVYILDQAEEEGHDLPYSCRAGSCSSCAGKVTAGSVDQSDGNFLDEDQEAAGFVLTCVAYPKGDVTIETHKEEELTA- 97
Arctium lappa Fd (gi:119976)           1 -ATYKVTLITPEGKQ-EFEVPDDVYILDHAAEEVGDLPYSCRAGSCSSCAGKVTAGSVDQSDGSYLDDDQMEAGWVLTCVAYPTSDVTIETHKEEELTA- 97
Oryza sativa FdI (gi:1070408)          1 -ATYNVKLITPDGEV-ELQVPDDVYILDQAEEEGIDLPYSCRAGSCSSCAGKVVSGEIDQSDQSFLDDDQVAAGWVLTCHAYPKSDVVIETHKEDDLI-- 96
Hordeum vulgare Fd (gi:228308)         1 -ATKKVKLVTPEGEV-ELEVPDDVYILDQAEEEGIDLPYSCRAGSCSSCAGKLVSGEIDQSDQSFLDDDQMEEGWVLTCAAYPKSDVVIETHKEEELTA- 97
Petroselinum crispum Fd (gi:75295858)  1 -ATYNVKLITPDGEV-EFKCDDDVYVLDQAEEEGIDIPYSCRAGSCSSCAGKVVSGSIDQSDQSFLDDEQMDAGYVLTCHAYPTSDVVIETHKEEEIV-- 96
Phytolacca acinosa FdII (gi:119951)    1 AASYKVTFVTPSGTK-TITCPADTYVLDAAEDTGLDLPYSCRAGACSSCAGKVTAGSVNQEDGSFLDEEQMEAGWVLTCVAYPTSDVTIETHKEEDLSA- 98
Phytolacca americana FII (gi:119950)   1 AASYKVTFVTPSGTN-TITCPADTYVLDAAEESGLDLPYSCRAGACSSCAGKVTAGAVNQEDGSFLEEEQMEAGWVLTCVAYPTSDVTIETHKEEDLTA- 98
Spinacia oleracea FdII (gi:119954)     1 -ATYKVTLVTPSGSQ-VIECGDDEYILDAAEEKGMDLPYSCRAGACSSCAGKVTSGSVDQSDQSFLEDGQMEEGWVLTCIAYPTGDVTIETHKEEELTA- 97
Marchantia polymorpha Fd (gi:120006)   1 --TFKVTLNTPTGQS-VIDVEDDEYILDAAEEAGLSLPYSCRAGACSSCAGKVTAGEVDQSDESFLDDDQMDEGYVLTCIAYPTSDLTIDTHQEEALI-- 95
Raphanus sativus Fd c (gi:947125)      1 -AAYKVKFITPDEDK-EVECDESEYVLDAAEESGIDLPYSCRAGACSSCAGKVVSGSVDQSDQSFLDDDQVADGFVLTCIARPTSDVVIRTHQEEEM-V- 96
Solanum lycopersicum FdII (gi:1589259) 1 -ATYKVKLITPEGPF-EFDCPDDVSILDRAEETGLDLPYSCRAGACSSCAGKVTAGSVDQSDNSFLDDDQIDEGFVLTCVAYPKSNVTIETHKEEDLVG- 97
Gleichenia japonica Fd (gi:120002)     1 -AIFKVKFLTPDGER-TIEVPDDKFILDAGEEAGLDLPYSCRAGACSSCTGKLLDGRVDQSEQSFLDDDQMAEGFVLTCVAYPAGDITIETHAEEKL--- 95
```

Fig. S1. Representation of the conserved residues of Fd in plants.

Sequence alignments of amino acid residues of various Fds are shown. The conserved residues are shown with black. An asterisk indicates serine 43 of maize Fd.

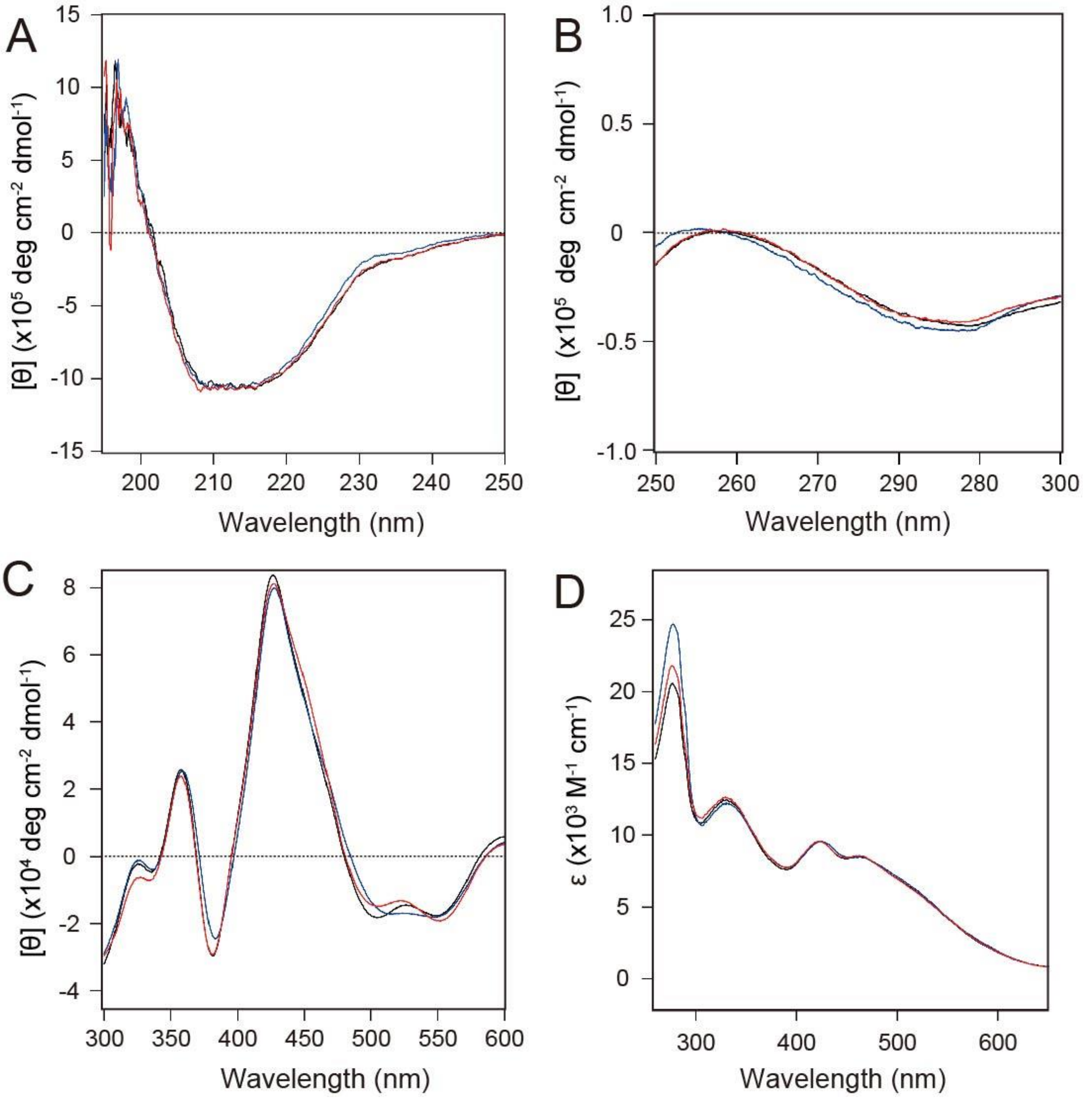

Fig. S2. Structural comparison of wild-type Fd and mutant Fds using various spectroscopies.

(A) Far-UV CD spectra. (B) Near-UV spectra. (C) CD spectra of the visible region. (D) UV-visible absorption spectra. The CD and absorption spectra of wild-type Fd (black), S43W Fd (blue), and S43D Fd (red) are shown.

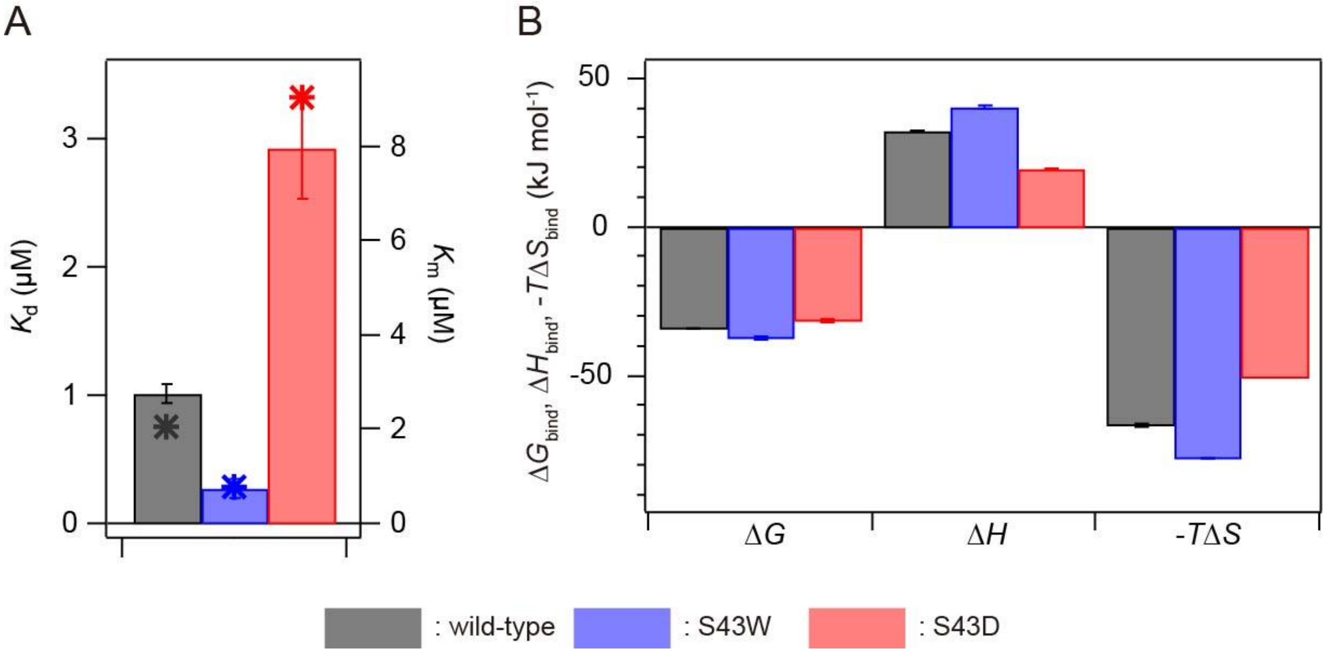

Fig. S3. Thermodynamic parameters of binding reactions between Fd and FNR obtained from ITC.

(A, B) The values of K_d (A) and various thermodynamic parameters (ΔG_{bind}, ΔH_{bind}, and $-T\Delta S_{bind}$) (B) for FNR binding to wild-type (black), S43W (blue), and S43D Fds (red) are schematically shown by the colored bars. The values of Km obtained by fitting to the Michaelis-Menten equation are indicated with asterisks in (A).

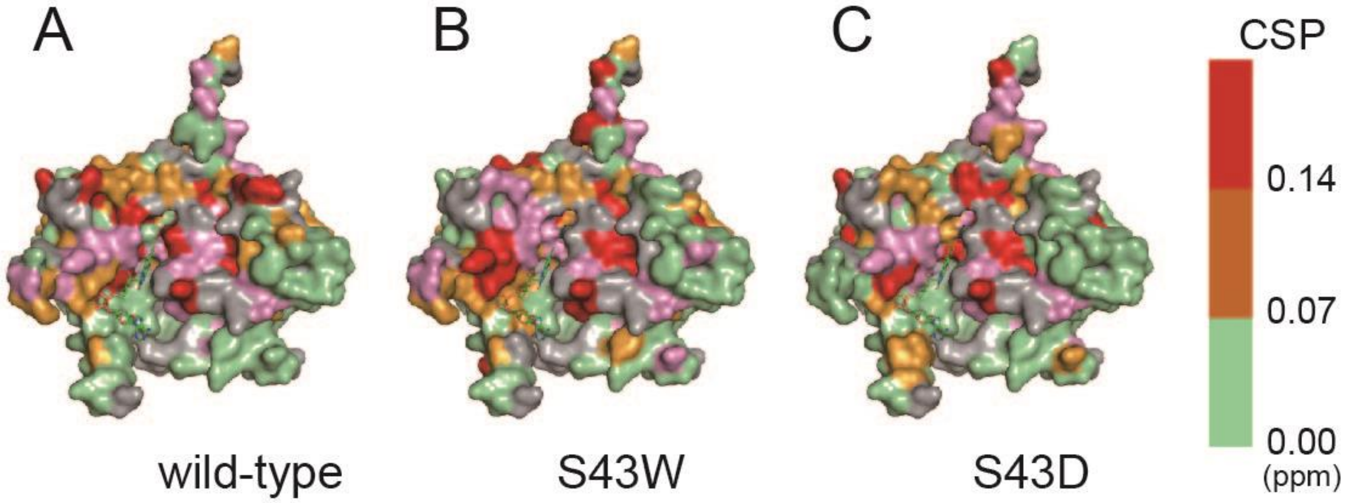

Fig. S4. Mapping of chemical shift perturbation onto the X-ray crystal structure of FNR.

(A-C) The degree of the chemical shift perturbation (CSP) was mapped onto the crystal structure of FNR (PDB/1GAQ) in the presence of wild-type (A), S43W (B), and S43D Fd (C). The color code represents as follows: Red, CSP > 0.14; orange, 0.14 > CSP > 0.07; light green, CSP < 0.07. The unassigned residues due to ambiguity of assignments are shown by pink.

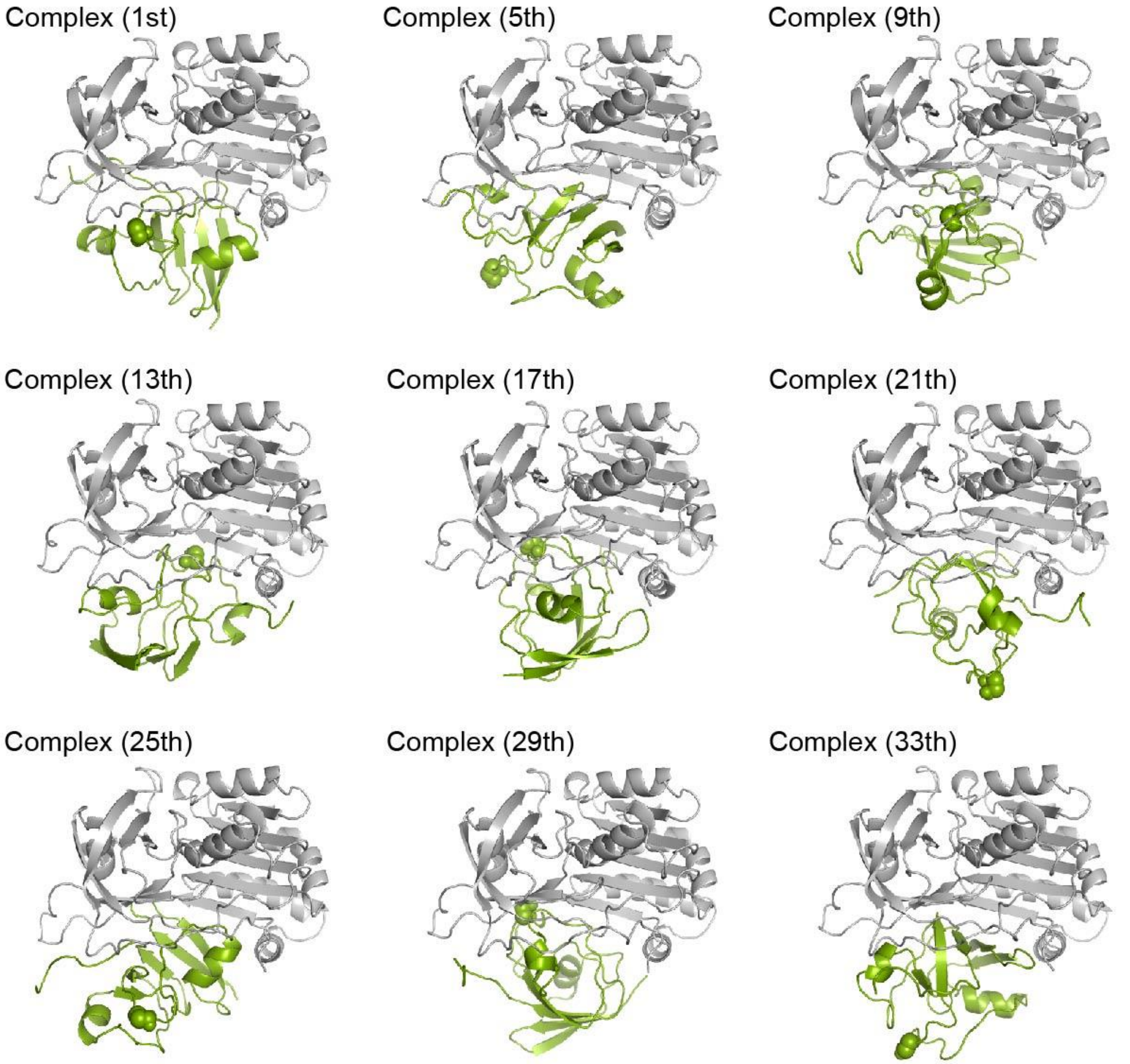
Complex (1st)
Complex (5th)
Complex (9th)
Complex (13th)
Complex (17th)
Complex (21th)
Complex (25th)
Complex (29th)
Complex (33th)

Fig. S5. Modeled wild-type Fd:FNR complexes.

The complex structures of wildtype Fd and FNR predicted by a docking simulation with HADDOCK in combination with NMR data are shown. Wild-type Fd and FNR are shown by green and gray, respectively. The likelihood of complex structures among 40 complexes obtained is this order of Complex (1st) > Complex (5th) > Complex (9th) > Complex (13th) > Complex (17th) > Complex (21th) > Complex (25th) > Complex (29th) > Complex (33th). The modeled structure of Complex (1th) is used in Figure 6.

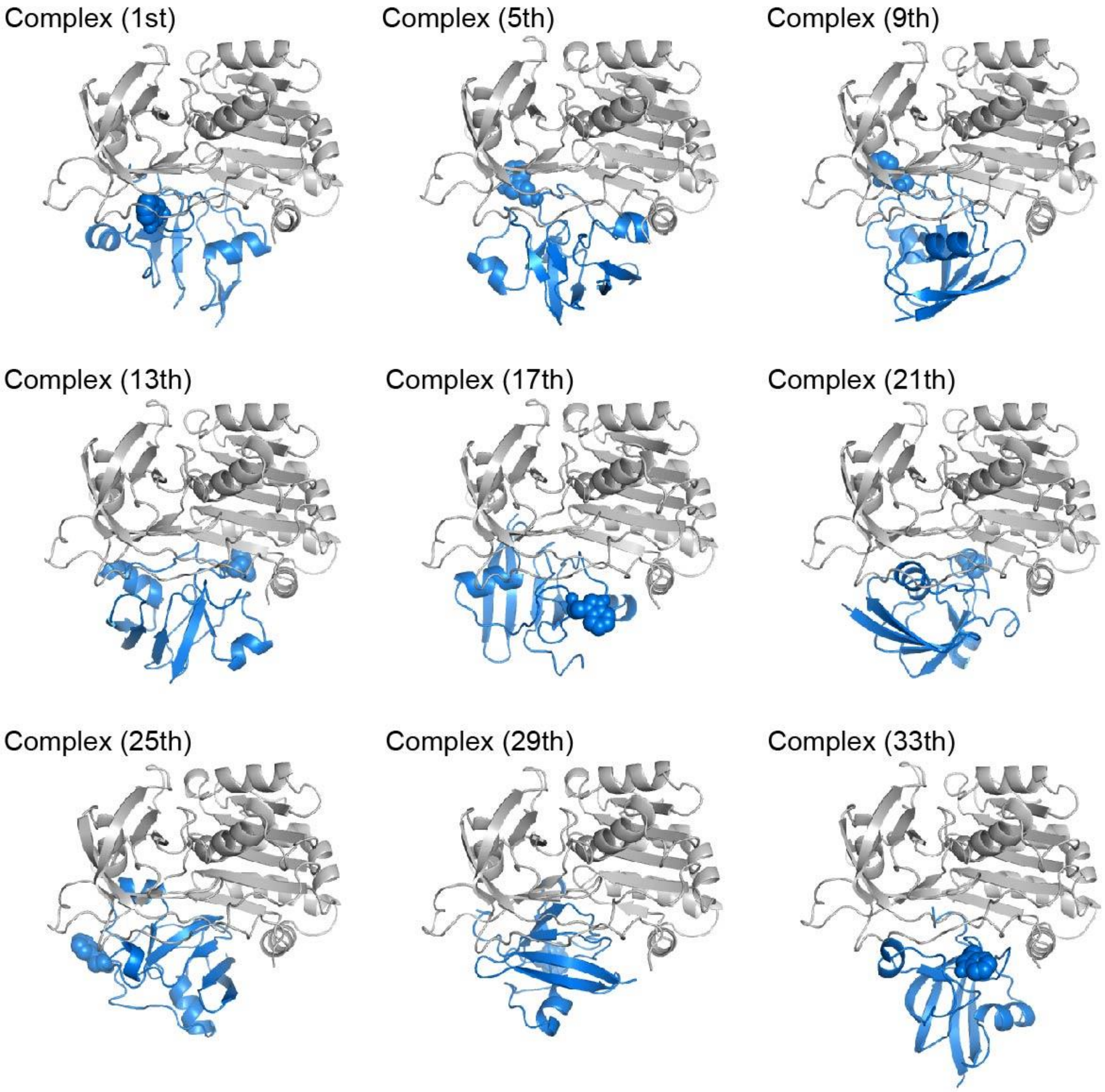
Complex (1st)
Complex (5th)
Complex (9th)
Complex (13th)
Complex (17th)
Complex (21th)
Complex (25th)
Complex (29th)
Complex (33th)

Fig. S6. Modeled S43W Fd:FNR complexes.

The complex structures of S43W Fd and FNR predicted by a docking simulation with HADDOCK in combination with NMR data are shown. S43W Fd and FNR are shown by blue and gray, respectively. The likelihood of complex structures among 40 complexes obtained is this order of Complex (1st) > Complex (5th) > Complex (9th) > Complex (13th) > Complex (17th) > Complex (21th) > Complex (25th) > Complex (29th) > Complex (33th). The modeled structure of Complex (1th) is used in Figure 6.

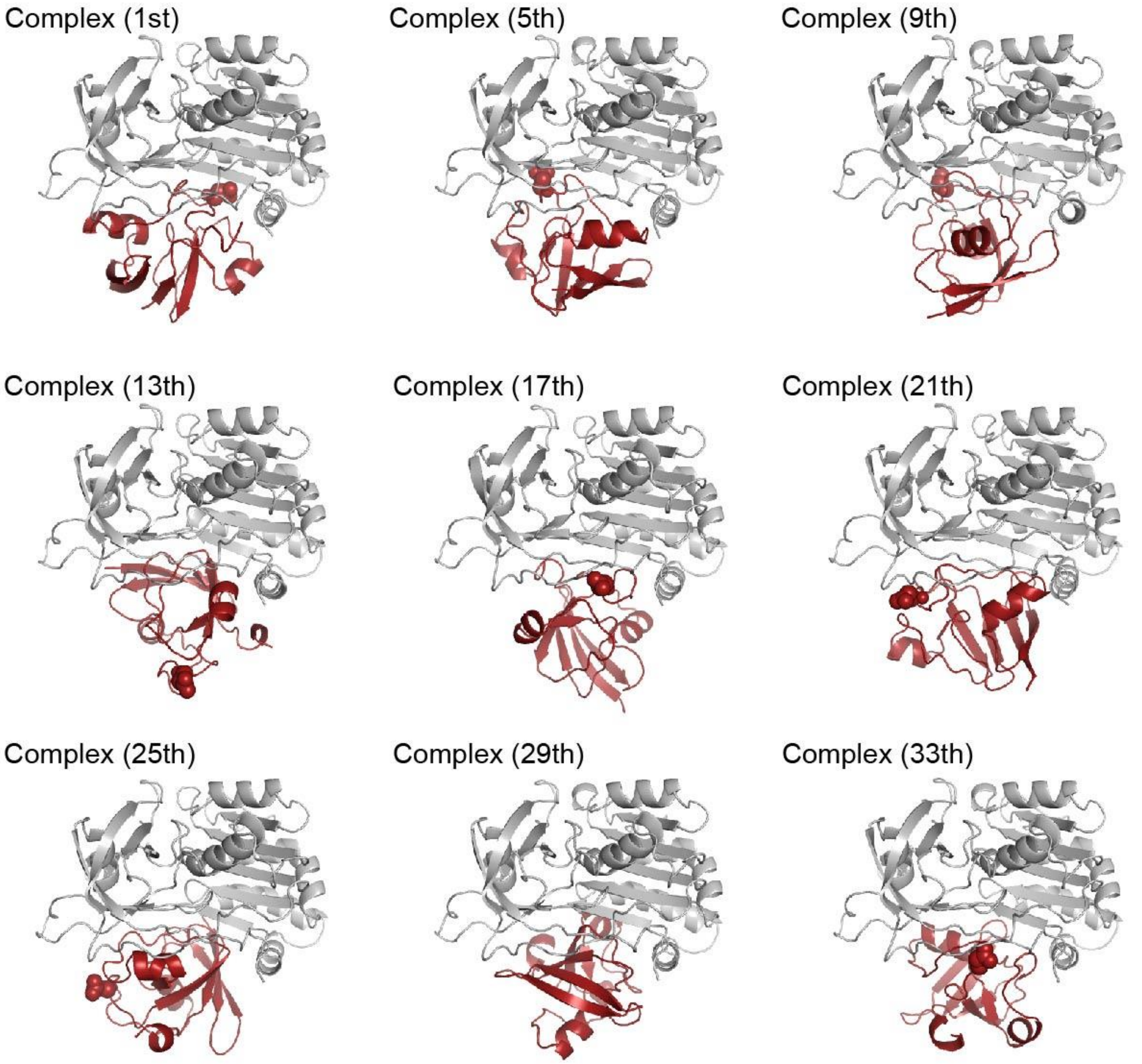
Complex (1st)
Complex (5th)
Complex (9th)
Complex (13th)
Complex (17th)
Complex (21th)
Complex (25th)
Complex (29th)
Complex (33th)

Fig. S7. Modeled S43D Fd:FNR complexes.

The complex structures of S43D Fd and FNR predicted by a docking simulation with HADDOCK in combination with NMR data are shown. S43D Fd and FNR are shown by red and gray, respectively. The likelihood of complex structures among 40 complexes obtained is this order of Complex (1st) > Complex (5th) > Complex (9th) > Complex (13th) > Complex (17th) > Complex (21th) > Complex (25th) > Complex (29th) > Complex (33th). The modeled structure of Complex (1th) is used in Figure 6.

References

[1] R. Gilli, D. Lafitte, C. Lopez, M. Kilhoffer, A. Makarov, C. Briand, J. Haiech, Thermodynamic analysis of calcium and magnesium binding to calmodulin, Biochemistry 37 (1998) 5450–5456.

[2] S. Kume, Y.H. Lee, M. Nakatsuji, Y. Teraoka, K. Yamaguchi, Y. Goto, T. Inui, Fine-tuned broad binding capability of human lipocalin-type prostaglandin D synthase for various small lipophilic ligands, FEBS Lett. 588 (2014) 962–969.

[3] Y.H. Lee, T. Ikegami, D.M. Standley, K. Sakurai, T. Hase, Y. Goto, Binding energetics of ferredoxin-NADP$^+$ reductase with ferredoxin and its relation to function, Chembiochem 12 (2011) 2062–2070.

[4] D. Eisenberg, M. Jucker, The amyloid state of proteins in human diseases, Cell 148 (2012) 1188–1203.

[5] G. Hanke, P. Mulo, Plant type ferredoxins and ferredoxin-dependent metabolism, Plant Cell Environ. 36 (2013) 1071–1084.

[6] C.J. Batie, H. Kamin, Electron transfer by ferredoxin:NADP$^+$ reductase. Rapid reaction evidence for participation of a ternary complex, J. Biol. Chem. 259 (1984) 11976–11985.

[7] D.G. Bishop, K.S. Andersen, R.M. Smillie, pH Dependence and cofactor requirements of photochemical reactions in maize chloroplasts, Plant Physiol. 50 (1972) 774–777.

[8] A. Sanchez-Azqueta, M. Martinez-Julvez, M. Hervas, J.A. Navarro, M. Medina, External loops at the ferredoxin-NADP(+) reductase protein-partner binding cavity contribute to substrates allocation, Biochim. Biophys. Acta 1837 (2014) 296–305.

[9] Y. Sakakibara, H. Kimura, A. Iwamura, T. Saitoh, T. Ikegami, G. Kurisu, T. Hase, A new structural insight into differential interaction of cyanobacterial and plant ferredoxins with nitrite reductase as revealed by NMR and X-ray crystallographic studies, J. Biochem. 151 (2012) 483–492.

[10] P. Mulo, Chloroplast-targeted ferredoxin-NADP(+) oxidoreductase (FNR): structure, function and location, Biochim. Biophys. Acta 1807 (2011) 927–934.

[11] T. Saitoh, T. Ikegami, M. Nakayama, K. Teshima, H. Akutsu, T. Hase, NMR study of the electron transfer complex of plant ferredoxin and sulfite reductase: mapping the interaction sites of ferredoxin, J. Biol. Chem. 281 (2006) 10482–10488.

[12] A. Sali, Comparative protein modeling by satisfaction of spatial restraints, Mol. Med. Today 1 (1995) 270–277.

[13] S.R. Tzeng, C.G. Kalodimos, Protein activity regulation by conformational entropy, Nature 488 (2012) 236–240.

[14] R.V. Duran, M. Hervas, M.A. De La Rosa, J.A. Navarro, The efficient functioning of photosynthesis and respiration in

Synechocystis sp. PCC 6803 strictly requires the presence of either cytochrome c6 or plastocyanin, J. Biol. Chem. 279 (2004) 7229–7233.

[15] M. Hippler, J. Reichert, M. Sutter, E. Zak, L. Altschmied, U. Schroer, R.G. Herrmann, W. Haehnel, The plastocyanin binding domain of photosystem I, EMBO J. 15 (1996)6374–6384.

[16] J.B. Asbury, E. Hao, Y. Wang, H.N. Ghosh, T. Lian, Ultrafast electron transfer dynamics from molecular adsorbates to semiconductor nanocrystalline thin films, J. Phys. Chem. B 105 (2001) 4545–4557.

[17] S. Rumpel, J.F. Siebel, C. Fares, J. Duan, E. Reijerse, T. Happe, W. Lubitz, M. Winkler, Enhancing hydrogen production of microalgae by redirecting electrons from photosystem I to hydrogenase, Energy Environ. Sci. 7 (2014) 3296–3301.

[18] M. Maeda, Y.H. Lee, T. Ikegami, K. Tamura, M. Hoshino, T. Yamazaki, M. Nakayama, T. Hase, Y. Goto, Identification of the N- and C-terminal substrate binding segments of ferredoxin-NADP+ reductase by NMR, Biochemistry 44 (2005) 10644–10653.

[19] Y. Onda, T. Matsumura, Y. Kimata-Ariga, H. Sakakibara, T. Sugiyama, T. Hase, Differential interaction of maize root ferredoxin:NADP(+) oxidoreductase with photosynthetic and non-photosynthetic ferredoxin isoproteins, Plant Physiol. 123 (2000) 1037–1045.

[20] G.T. Hanke, Y. Satomi, K. Shinmura, T. Takao, T. Hase, A screen for potential ferredoxin electron transfer partners uncovers new, redox dependent interactions, Biochim. Biophys. Acta 1814 (2011) 366–374.

[21] D.B. Knaff, M. Hirasawa, Ferredoxin-dependent chloroplast enzymes, Biochim. Biophys. Acta 1056 (1991) 93–125.

[22] G. Kurisu, M. Kusunoki, E. Katoh, T. Yamazaki, K. Teshima, Y. Onda, Y. Kimata-Ariga, T. Hase, Structure of the electron transfer complex between ferredoxin and ferredoxin-NADP(+) reductase, Nat. Struct. Mol. Biol. 8 (2001) 117–121.

[23] P.A. Karplus, M.J. Daniels, J.R. Herriott, Atomic structure of ferredoxin-NADP+ reductase: prototype for a structurally novel flavoenzyme family, Science 251 (1991) 60–66.

[24] M. Nakayama, T. Akashi, T. Hase, Plant sulfite reductase: molecular structure, catalytic function and interaction with ferredoxin, J. Inorg. Biochem. 82 (2000) 27–32.

[25] M. Martinez-Julvez, M. Medina, A. Velazquez-Campoy, Binding thermodynamics of ferredoxin:NADP+ reductase: two different protein substrates and one energetics, Biophys. J. 96 (2009) 4966–4975.

[26] A. Aliverti, M.E. Corrado, G. Zanetti, Involvement of lysine-88 of spinach ferredoxinNADP+ reductase in the interaction with ferredoxin, FEBS Lett. 343 (1994) 247–250.

[27] F.J. Enguita, E. Pohl, D.L. Turner, H. Santos, M.A. Carrondo, Structural evidence for a proton transfer pathway coupled

with haem reduction of cytochrome c from Methylophilus methylotrophus, J. Biol. Inorg. Chem. 11 (2006) 189–196.

[28] T. Hase, S. Mizutani, Y. Mukohata, Expression of maize ferredoxin cDNA in Escherichia coli: comparison of photosynthetic and nonphotosynthetic ferredoxin isoproteins and their chimeric molecule, Plant Physiol. 97 (1991) 1395–1401.

[29] T. Matsumura, Y. Kimata-Ariga, H. Sakakibara, T. Sugiyama, H. Murata, T. Takao, Y. Shimonishi, T. Hase, Complementary DNA cloning and characterization of ferredoxin localized in bundle-sheath cells of maize leaves, Plant Physiol. 119 (1999) 481–488.

[30] Y.H. Lee, K. Tamura, M. Maeda, M. Hoshino, K. Sakurai, S. Takahashi, T. Ikegami, T. Hase, Y. Goto, Cores and pH-dependent dynamics of ferredoxin-NADP+ reductase revealed by hydrogen/deuterium exchange, J. Biol. Chem. 282 (2007) 5959–5967.

[31] W. Lee, M. Tonelli, J.L. Markley, NMRFAM-SPARKY: enhanced software for biomolecular NMR spectroscopy, Bioinformatics 31 (2014) 1325–1327.

[32] R. Luthy, J.U. Bowie, D. Eisenberg, Assessment of protein models with threedimensional profiles, Nature 356 (1992) 83–85.

[33] C. Dominguez, R. Boelens, A.M. Bonvin, HADDOCK: a protein–protein docking approach based on biochemical or biophysical information, J. Am. Chem. Soc. 125 (2003) 1731–1737.

[34] L. Willard, A. Ranjan, H. Zhang, H. Monzavi, R.F. Boyko, B.D. Sykes, D.S. Wishart, VADAR: a web server for quantitative evaluation of protein structure quality, Nucleic Acids Res. 31 (2003) 3316–3319.

[35] J.K. Hurley, A.M. Weber-Main, M.T. Stankovich, M.M. Benning, J.B. Thoden, J.L. Vanhooke, H.M. Holden, Y.K. Chae, B. Xia, H. Cheng, J.L. Markley, M. MartinezJulvez, C. Gomez-Moreno, J.L. Schmeits, G. Tollin, Structure–function relationships in Anabaena ferredoxin: correlations between X-ray crystal structures, reduction potentials, and rate constants of electron transfer to ferredoxin:NADP$^+$ reductase for site-specific ferredoxin mutants, Biochemistry 36 (1997) 11100–11117.

[36] S. Chhabra, O. Dolezal, B.M. Collins, J. Newman, J.S. Simpson, I.G. Macreadie, R. Fernley, T.S. Peat, J.D. Swarbrick, Structure of S. aureus HPPK and the discovery of a new substrate site inhibitor, PLoS ONE 7 (2012) e29444.

[37] E. Meiby, H. Simmonite, L. le Strat, B. Davis, N. Matassova, J.D. Moore, M. Mrosek, J. Murray, R.E. Hubbard, S. Ohlson, Fragment screening by weak affinity chromatography: comparison with established techniques for screening against HSP90, Anal. Chem. 85 (2013) 6756–6766.

[38] Y. Zhen, C.W. Hoganson, G.T. Babcock, S. Ferguson-Miller, Definition of the interaction domain for cytochrome c on cytochrome c oxidase. I. Biochemical, spectral, and kinetic characterization of surface mutants in subunit ii of Rhodobacter sphaeroides cytochrome aa3, J. Biol. Chem. 274 (1999) 38032–38041.

[39] V. Ball, C. Maechling, Isothermal microcalorimetry to investigate non specific interactions in biophysical chemistry, Int. J. Mol. Sci. 10 (2009) 3283–3315.

[40] H.X. Zhou, Disparate ionic-strength dependencies of on and off rates in protein–protein association, Biopolymers 59 (2001) 427–433.

[41] K. Koga, Osmotic second virial coefficient of methane in water, J. Phys. Chem. B 117 (2013) 12619–12624.

[42] S. Kumar, R. Nussinov, Different roles of electrostatics in heat and in cold: adaptation by citrate synthase, Chembiochem 5 (2004) 280–290.

[43] T. Ikenoue, Y.H. Lee, J. Kardos, H. Yagi, T. Ikegami, H. Naiki, Y. Goto, Heat of supersaturation-limited amyloid burst directly monitored by isothermal titration calorimetry, Proc. Natl. Acad. Sci. 111 (2014) 6654–6659.

[44] S. Neal, A.M. Nip, H. Zhang, D.S. Wishart, Rapid and accurate calculation of protein ^{1}H, ^{13}C and ^{15}N chemical shifts, J. Biomol. NMR 26 (2003) 215–240.

Chapter 3

Energetic basis on interactions between ferredoxin and ferredoxin NADP$^+$ reductase at varying physiological conditions.

Abstract

In spite of a number of studies to characterize ferredoxin (Fd):ferredoxin NADP$^+$ reductase (FNR) interactions at limited conditions, detailed energetic investigation on how these proteins interact under near physiological conditions and its linkage to FNR activity are still lacking. I herein performed systematic Fd:FNR binding thermodynamics using isothermal titration calorimetry (ITC) at distinct pH (6.0 and 8.0), NaCl concentrations (0-200 mM), and temperatures (19-28°C) for mimicking physiological conditions in chloroplasts. Energetically unfavorable endothermic enthalpy changes were accompanied by Fd:FNR complexation at all conditions. This energetic cost was compensated by favorable entropy changes, balanced by conformational and hydrational entropy. Increases in the NaCl concentration and pH weakened interprotein affinity due to the less contribution of favorable entropy change regardless of energetic gains from enthalpy changes, suggesting that entropy drove complexation and modulated affinity. Effects of temperature on binding thermodynamics were much smaller than those of pH and NaCl. NaCl concentration and pH-dependent enthalpy and heat capacity changes provided clues for distinct binding modes. Moreover, decreases in the enthalpy level in the Hammond's postulate-based energy landscape implicated kinetic advantages for FNR activity. All these energetic interplays were comprehensively demonstrated by the driving force plot with the enthalpy-entropy compensation which may serve as an energetic buffer against outer stresses. I propose that high affinity at pH 6.0 may be beneficial for protection from proteolysis of Fd and FNR in rest states, and moderate affinity at pH 8.0 and proper NaCl concentrations with smaller endothermic enthalpy changes may contribute to increase FNR activity.

1. Introduction

Enzymes function through not only physical binding reactions between enzymes and binding partners including substrates but also catalysis of chemical reactions in enzymes. Thus, the binding reaction of enzymes with partner molecules, i.e., complex formation, is the most underlying process for enzymatic activity [1,2,3,4]. Formation of complexes and molecular recognition depend on environmental conditions such as ionic strength, temperature, pH, or crowders [2,3,4,5,6]. Decreases in the intermolecular binding affinity or the alternation of the binding mode due to changes in ambient conditions and mutation often leads to inactivation of enzymes without the impairment of intrinsic catalytic power of enzymes [3,4,6].

All of intermolecular interactions including protein complex formation are controlled by thermodynamics. Thus, thermodynamics provide useful information on the formation of protein complexes for enzymatic activity depending on conditions. Isothermal titration calorimetry (ITC) is the most efficient approach to thermodynamically investigate binding systems at diverse conditions by taking advantages of direct detection of reaction heat [2,3,4,7,8,9].

I previously examined binding thermodynamics between ferredoxin (Fd) and either ferredoxin-NADP$^+$ reductase (FNR) [2,3,10,11] or sulfite reductase (SiR) [4] using ITC at limited conditions. Fd:FNR and Fd:SiR complex formation have shown similar interprotein affinity with distinct favorable driving forces, which indicated the importance of ITC-based thermodynamics to reveal binding properties in solution.

In order to improve our understanding on how Fd and Fd-dependent enzymes such as FNR, SiR, nitrite reductase, or glutamate synthase [12,13] interact energetically for enzyme activity, I herein performed in-depth thermodynamic study on the complex formation between Fd and FNR from derived from maize leaf using ITC at biologically relevant conditions.

Fd is a small acidic electron-carrying proteins and distributes electrons to many enzymes [12]. FNR is a relatively large multi-domain enzyme and catalyzes the reduction of NADP$^+$ to NADPH for the Calvin cycle during photosynthesis using electrons transferred from Fd [2,3,5,10,11,14,15]. Thus, the formation of an electron transfer complex between Fd and FNR is a prerequisite for FNR activity. In our previous studies, it was revealed that one Fd bound to one FNR using X-ray crystallography, analytical ultracentrifugation, solution NMR spectroscopy, and ITC [2,3,14,15]. Fd and FNR provide an excellent *in vitro* model system for examining binding thermodynamics at physiologically relevant experimental conditions because two proteins interact in the chloroplast stroma where pH, ionic strength, and temperature vary [4,15,16,17,18].

I describe ITC-based thermodynamics on Fd:FNR complex formation at changing pH, NaCl concentration, and temperature for mimicking physiological environments, and discuss how energetic interplay in response to external stresses plays a role in the Fd:FNR interaction and FNR activity. The current study will be particularly useful for energetic insights into electron transfer complex formation and their relation to enzyme function.

2. Materials and Methods

2.1. Preparation of Fd and FNR

Recombinant Fd and FNR from the maize leaf were overexpressed in *Escherichia coli* strain JM109 and TG1 cells, respectively, at 37 ºC using Luria-Bertani medium. Detailed methods for purification of Fd and FNR are described in the supplementary data.

2.2. Isothermal titration calorimetry (ITC) measurements

Protein solutions were dialyzed against 20 mM sodium phosphate buffer (pH 6.0) or 50 mM Tris-HCl (pH 8.0) and degassed for 3 min before being loaded into the calorimeter. Calorimetric experiments were performed with a PEAQ-ITC instrument (Malvern Instruments, UK) at the various temperature (19, 22, 25, and 28 °C) and the NaCl concentration (0, 30, 60, 100, and 200 mM) at pH 6.0 and 8.0. Fd at 1-2 mM in the injection syringe was titrated into 50 μM FNR in the ITC cell. Titration experiments consisted of 19 or 27 injections spaced at intervals of 100 sec. The injection volume was 0.1 or 1.5 μL and the cell was continuously stirred at 750 rpm. Differential power was set to 5 μcal sec^{-1}. Thermodynamic parameters were calculated as described in the supplementary data.

3. Results and Discussion

3.1. Observation of heat for the Fd:FNR complex formation by ITC

I performed systematic ITC measurements for complex formation between oppositely-charged Fd and FNR (**Fig. S1**) at pH 6.0 and 8.0 by increasing the NaCl concentration from 0 to 200 mM and temperature from 19 to 28°C (**Figs. 1** and **S2**). All of ITC thermograms for Fd titration to FNR showed positive ITC peaks and their saturation to the level of small heat of dilution, which suggested that Fd bound to FNR by uptaking of heat, i.e., an endothermic reaction, and Fd:FNR binding ended within the molar ratio set (**Figs. 2** and **S3**). Observed endothermic heat was susceptible to the change in conditions. The increase in the NaCl concentration or pH decreased the magnitude of endothermic heat although temperature change caused slight variation of the amplitude of heat.

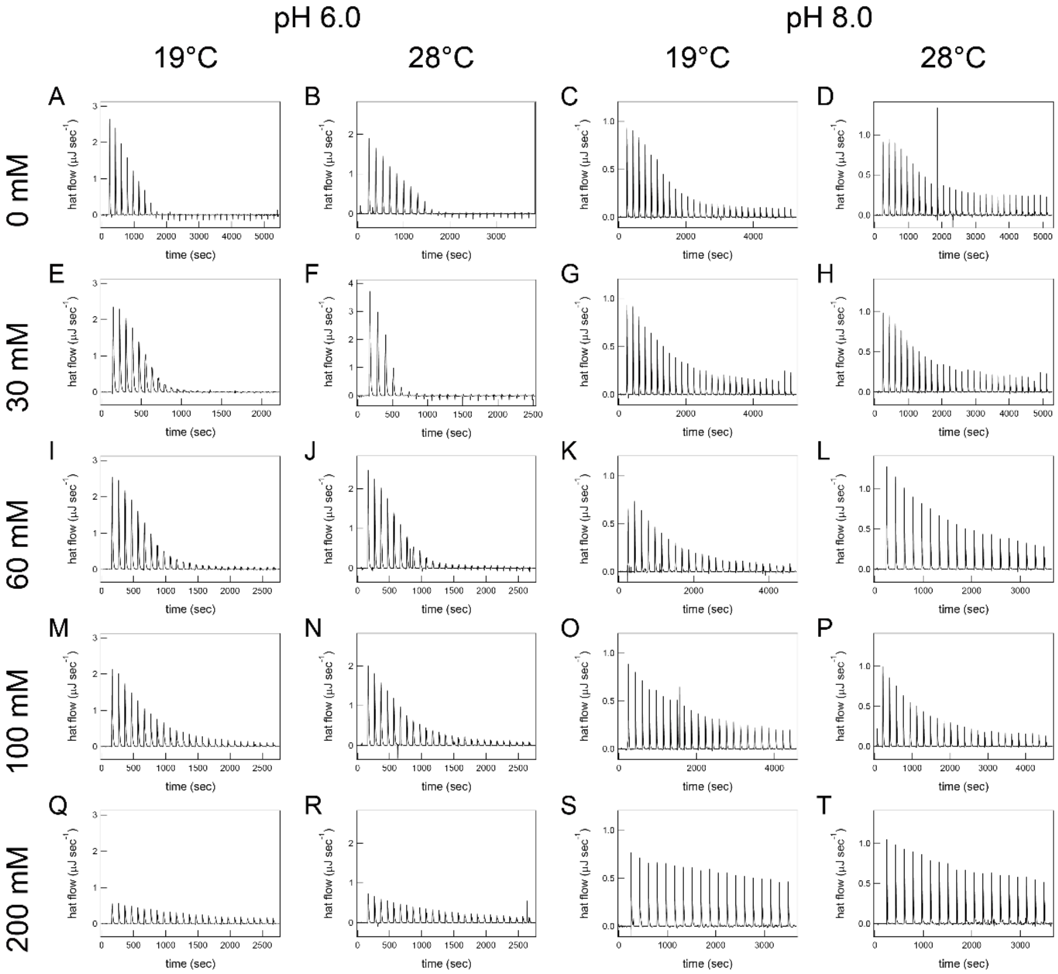

Fig. 1. ITC thermograms of Fd titration to FNR at various conditions.

ITC thermograms of the titration of Fd to FNR obtained at 19 (A, C, E, G, I, K, M, O, Q, and S), 28°C (B, D, F, H, J, L, N, P, R, and T) under distinct pH values (pH 6.0 (A, B, E, F, I, J, M, N, Q, and R) and 8.0 (C, D, G, H, K, L, O, P, S, and T)) in the presence of 0 (A-D), 30 (E-H), 60 (I-L), 100 (M-P), and 200 mM NaCl (Q-T).

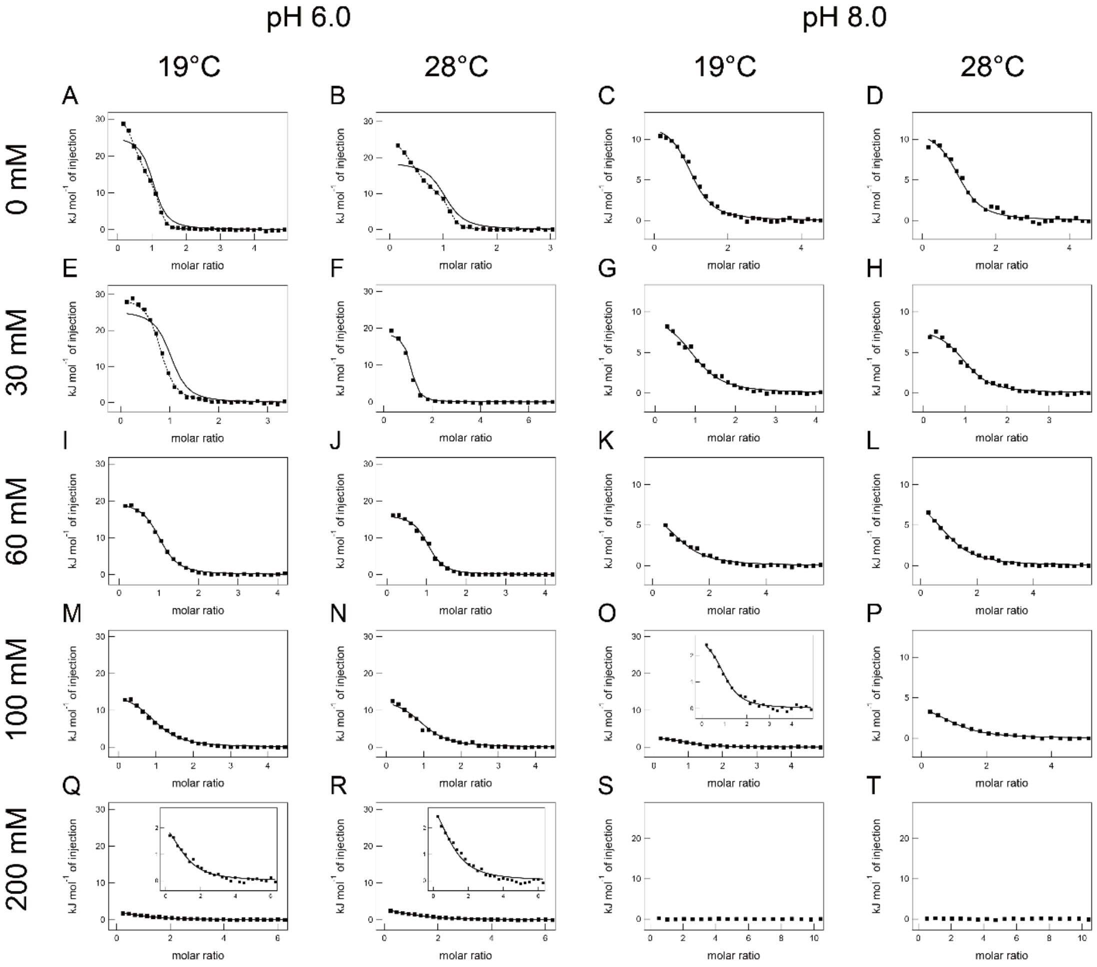

Fig. 2. Fd:FNR binding isotherms obtained using ITC at various conditions.

Fd:FNR binding isotherms obtained at 19 (A, C, E, G, I, K, M, O, Q, and S), 28 °C (B, D, F, H, J, L, N, P, R, and T) under distinct pH values (pH 6.0 (A, B, E, F, I, J, M, N, Q, and R) and 8.0 (C, D, G, H, K, L, O, P, S, and T)) in the presence of 0 (A-D), 30 (E-H), 60 (I-L), 100 (M-P), and 200 mM NaCl (Q-T). Fit curves based on one-to-one and one-to-two binding models between Fd and FNR are shown with solid and dotted lines. Normalized values and fit curves in O, Q, and R magnified are shown in insets.

3.2. Energetic cost of enthalpy for complex formation and its possible biological role

The enthalpy change (ΔH_{bind}) for the Fd:FNR complex formation was first calculated, which is one of the two driving forces, ΔH and the change in entropy (ΔS). As expected from upward ITC peaks, positive ΔH_{bind} for endothermic complex formation was obtained at all conditions. ΔH_{bind} values depended on the conditions and ranged from ~2 to ~30 kJ $\mathrm{mol^{-1}}$ (Fig. 3A, B and Tables S1, S2). Thermodynamic analyses at pH 8.0 and all temperature in the presence of 200 mM NaCl were hampered by gradual decreases in heat with small magnitudes.

These results indicated obviously that enthalpy is thermodynamically unfavorable for the complex formation. The increase in the NaCl concentration and pH decreased the magnitude of positive ΔH_{bind}, indicating that disadvantageous enthalpic contributions became energetically preferable at higher NaCl concentrations and pH. The variation in ΔH_{bind} depending on temperature was small, which indicated that enthalpy for the complex formation responds more sensitively to the NaCl concentration and pH than temperature.

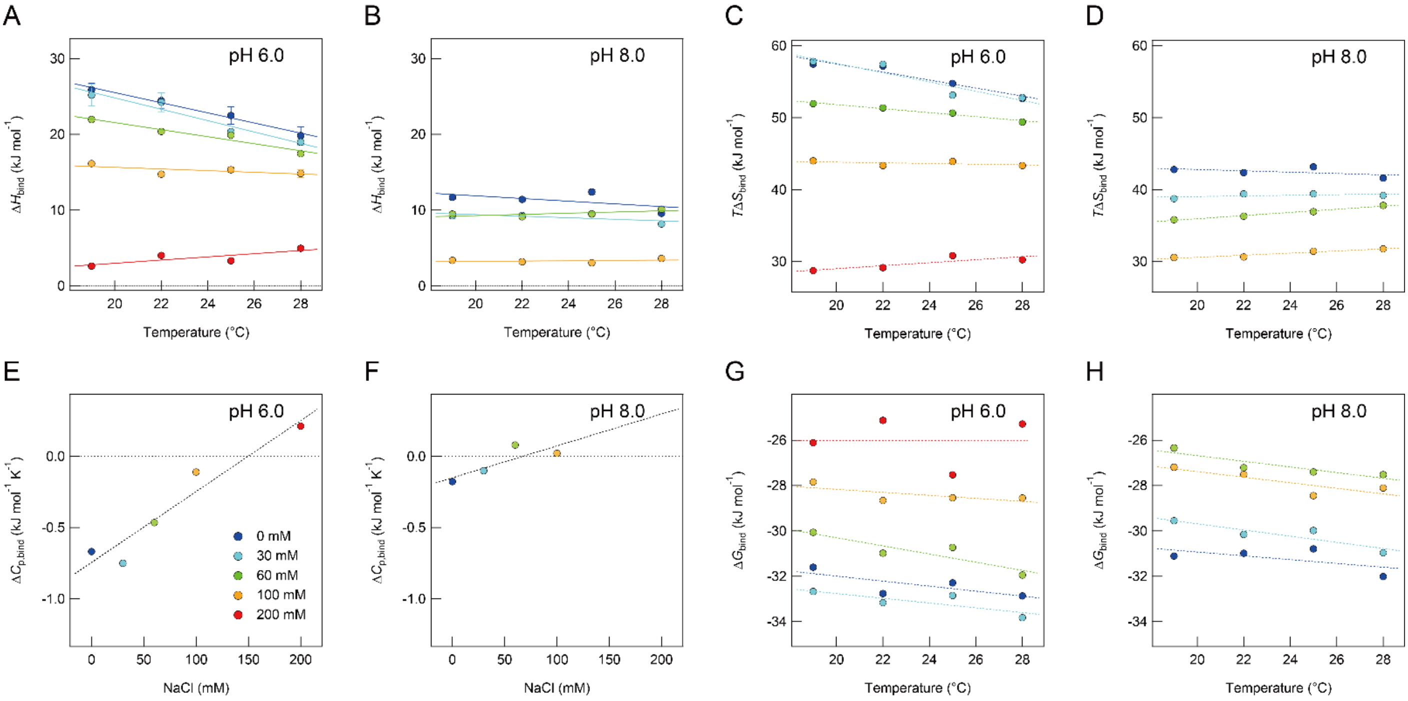

Fig. 3. Thermodynamic parameters of the formation of the Fd:FNR complex at various conditions.
The change in enthalpy (ΔH_{bind}) (A and B), entropy (ΔS_{bind}) (C and D), heat capacity ($\Delta C_{\mathrm{p,bind}}$) (E and F), and Gibbs free energy (ΔG_{bind}) (G and H) at pH 6.0 (A, C, E, and G) and 8.0 (B, D, F, and H) were plotted against the temperature. Data obtained at distinct NaCl concentrations are represented with the color code. In A and B, fitted curves for $\Delta C_{\mathrm{p,bind}}$ are indicated with straight lines. Dotted lines in C-H were drawn for showing comprehensively a trend in changes.

I consider a biological role of enthalpy and endothermic Fd:FNR complexation as follows. First, from the viewpoint of thermodynamics, a positive enthalpy change is an inhibitor for the complex formation which in turn blocks the interprotein electron transfer for FNR activity. However, enthalpy may play a role in tuning of the conformation or configuration of a protein complex (e.g., orientation of each protein in a complex) for enzymatic activity in the NaCl concentration or pH-dependent way (Fig. 4A and C, right cartoon) as enthalpy reflects heat responsible for direct molecular contacts at protein interfaces including formation of intermolecular hydrogen bonds and salt bridges as well as van der Waals interactions.

The concept of energetic tuning is also supported by the distinct value and sign of the change in heat capacity (ΔC_p) at the distinct NaCl concentration and pH (refer to the next section) (Fig. 4A and C, right cartoon) and by our previous thermodynamic studies on interactions of Fd with its partner enzymes [2,3,4]. Strong electrostatic interactions between molecules are readily expected to be an exothermic reaction. Thus, interactions between negatively-charged Fd and positively-charged patches of FNR [2,3,14,19] or SiR [6] (Fig. S1) were both expected to be exothermic. However, the binding of the same Fd to FNR or SiR, even with similar binding sites of Fd [4,6,14,20], resulted in an opposite sign of ΔH_{bind}: endothermic Fd:FNR complex formation (Tables S1 and S2) [2,3] and exothermic Fd:SiR complex formation [4], indicating that enthalpy is a sensitive energetic probe for detecting even subtle differences in binding modes.

Second, in order to relate thermodynamics to kinetics for enzymatic function, the Hammond's postulate-based energy landscape was constructed (Fig. 4A and C). This hypothesis provided that, in an endothermic reaction, the energy level of Fd:FNR complex is higher than that in free states in terms of thermodynamics, and the high activation energy barrier for complexation exists in terms of kinetics. As the NaCl concentration (Fig. 4A) or pH (Fig. 4C) increases, the extent of positive ΔH_{bind} and activation energy (E_a) diminishes (Fig. 4A and C, middle) with distinct final complex configurations due to tuning as mentioned above (Fig. 4A and C, right cartoon). Hence, the association rate between Fd and FNR may become faster due to the decrease in E_a, which may enhance overall activity of FNR at pH 8.0 and higher NaCl concentrations since faster association between electron transport proteins has shown to increase electron transfer rates [21].

However, it should be noted that tuning and kinetic effects are only valid when interprotein affinity is recognizable since too high pH and NaCl concentrations disturb significantly binding events themselves.

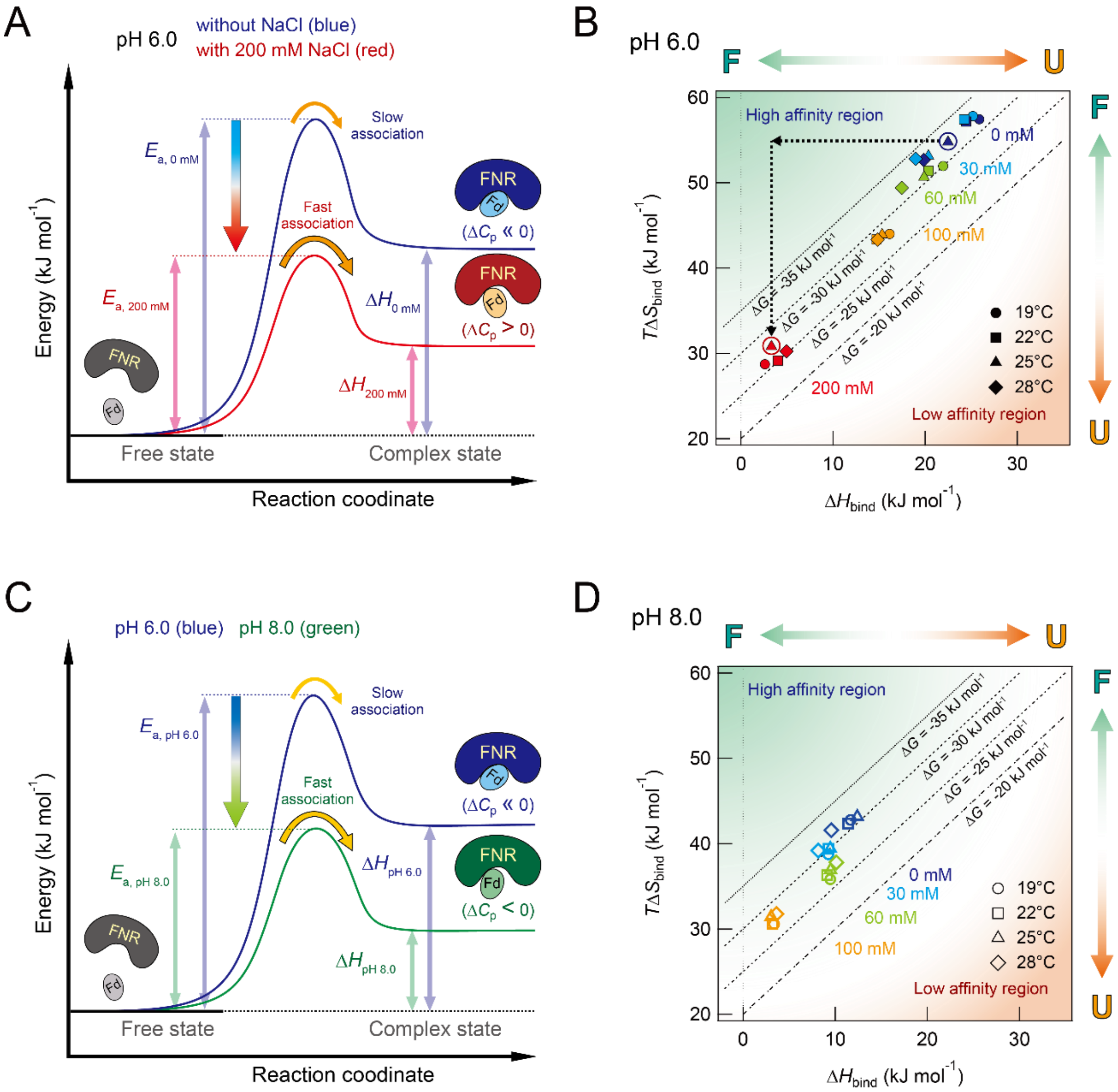

Fig. 4. Hammond's postulate-based energy landscape and driving force plot for the Fd:FNR complex formation.

(A and C) Energy landscapes based on the Hammond's postulate at pH 6.0 with (red landscape) and without 200 mM NaCl (blue landscape) (A) and at pH 6.0 (blue landscape) and 8.0 without NaCl (green landscape) (C) are shown. Fd and FNR in free states (left) and the Fd:FNR complex (right) are schematically represented. Distinct binding modes of complexes at each condition are also illustrated. Signs of ΔC_p are shown based on values obtained from ITC measurements (Tables S1 and S2). In A, $E_{a,\,0\ mM}$ and $E_{a,\,200\ mM}$ represent the activation energy at 0 and 200 mM NaCl, respectively. $\Delta H_{0\ mM}$ and $\Delta H_{200\ mM}$ indicate endothermic enthalpy changes at 0 and 200 mM NaCl, respectively. In C, $E_{a,\,pH\ 6.0}$ and $E_{a,\,pH\ 8.0}$ represent the activation energy at pH 6.0 and 8.0, respectively. $\Delta H_{pH\ 6.0}$ and $\Delta H_{pH\ 8.0}$ indicate endothermic enthalpy changes at pH 6.0 and 8.0, respectively, without NaCl. (B and D) Driving forces for Fd:FNR complex formation at pH 6.0 (closed symbols) (B) and 8.0 (open symbols) (D) with various NaCl concentration and temperature were plotted. Diagonal broken lines indicate ΔG_{bind} of -35, -30, -25, and -20 kJ mol^{-1} (from the left line). Increases and decreases in affinity are also colored by green and orange, respectively, inside the panel. Favorable and unfavorable directions for complexation are shown with F and U, respectively, outside the panel. In B, the change in affinity at pH 6.0 and 25°C on increasing NaCl concentration from 0 to 200 mM is energetically explained with guidance of dotted line and arrow.

3.3. Heat capacity change reflects binding modes between Fd and FNR

ΔC_p is also a key thermodynamic parameter which provides information on interprotein interactions since ΔC_p in a biomolecular system is mostly interpreted by the change in the accessible surface area (ASA) buried on protein complex formation [2,3,6,7,8,22]. The burial of polar and apolar ASA has been considered to increase and decrease ΔC_p, respectively. Although this is not always applicable to protein-protein interaction systems, the sign and magnitude of ΔC_p are still useful criteria for comparing binding modes between proteins at different conditions.

I obtained $\Delta C_\mathrm{p,bind}$ for Fd:FNR binding (Tables S1 and S2) from the linear dependence of ΔH against temperature (Fig. 3A and B). $\Delta C_\mathrm{p,bind}$ changed dynamically and ranged from -0.75 to 0.21 kJ mol^{-1} K^{-1} (Fig. 3E and F). At pH 6.0 with increasing the NaCl concentration, negative $\Delta C_\mathrm{p,bind}$ decreased its magnitude and was converted to a positive value over 100 mM NaCl (Fig. 3E). Although the magnitude of $\Delta C_\mathrm{p,bind}$ was different, a similar response of $\Delta C_\mathrm{p,bind}$ to the NaCl perturbation was also detected at pH 8.0 (Fig. 3F).

These thermodynamic findings implicated that structural rearrangements at interfaces in the Fd:FNR complex may occur because the same binding modes with the same ΔASA should show the same $\Delta C_\mathrm{p,bind}$ values. Therefore, distinct binding modes at the different NaCl concentration and pH (Fig. 4A and C, right cartoon) were expected as described in the previous section, which may be involved in the control of overall FNR activity since the complex configuration affects electron transport rates [23] and enzyme activity [4].

3.4. Purely entropy-driven formation of the Fd:FNR complex through the balance between protein flexibility and dehydration

Complex formation and affinity are limited by the change in Gibbs free energy (ΔG), which is balanced by ΔH and (-)$T\Delta S$. Due to energetically unfavorable positive ΔH for the complex formation at all conditions, Fd:FNR complex formation was expected to be driven by only positive ΔS_bind. Indeed, ΔS_bind was all positive (Fig. 3C, D and Tables S1, S2) and $T\Delta S_\mathrm{bind}$ ranged from ~29 to ~58 kJ mol^{-1}, demonstrating that ΔS_bind overcame energetically disfavored ΔH_bind and stabilized the Fd:FNR complex with generating negative ΔG_bind (Fig. 3G, H and Tables S1, S2). Negative ΔG_bind decreased its degree upon the increase in the NaCl concentration and pH and no significant temperature dependence was observed (Fig. 3G and H). The entropic contribution to complex formation was more prominent at the lower pH and the NaCl concentration. There were also no significant temperature dependences in $T\Delta S_\mathrm{bind}$ although slight decreases in $T\Delta S_\mathrm{bind}$ at pH 6.0 were observed at 0 and 30 mM NaCl concentrations (Fig. 3C).

In order to clarify entropic roles in more detail, I dissected the net ΔS (ΔS_{bind}) directly obtained from ITC measurements to the three ΔS terms [2], the change in mixing (${}^{\mathrm{mix}}\Delta S_{\mathrm{bind}}$), dehydration (${}^{\mathrm{dehyd}}\Delta S_{\mathrm{bind}}$), and conformation (${}^{\mathrm{conf}}\Delta S_{\mathrm{bind}}$) (Fig. S4 and Tables S3, S4). Since the Fd:FNR complex formation decreases the number of molecules in a system, $(T)^{\mathrm{mix}}\Delta S_{\mathrm{bind}}$ values were negative and energetically unfavorable (Tables S3 and S4). Meanwhile, the contribution of $(T)^{\mathrm{dehyd}}\Delta S_{\mathrm{bind}}$, which reflects the change in the number of free water [2], and $(T)^{\mathrm{conf}}\Delta S_{\mathrm{bind}}$, which is responsible for the change in protein dynamics [2,24], was largely dependent on the NaCl concentration and pH (Fig. S4A and B). $(T)^{\mathrm{dehyd}}\Delta S_{\mathrm{bind}}$ and $(T)^{\mathrm{conf}}\Delta S_{\mathrm{bind}}$ at pH 6.0 showed larger distribution than those at pH 8.0. Positive $(T)^{\mathrm{dehyd}}\Delta S_{\mathrm{bind}}$ at pH 6.0 was changed to negative values over 100 mM NaCl. $(T)^{\mathrm{conf}}\Delta S_{\mathrm{bind}}$ was found to be positive at both pH except for negative $(T)^{\mathrm{conf}}\Delta S_{\mathrm{bind}}$ at 0 and 60 mM NaCl and pH 6.0 (Fig. S4C and D). Unfavorable changes of $(T)^{\mathrm{dehyd}}\Delta S_{\mathrm{bind}}$ at increasing NaCl concentrations were compensated by favorable changes of $(T)^{\mathrm{conf}}\Delta S_{\mathrm{bind}}$.

These findings suggested that entropic contributions of protein dynamics are essential for forming the Fd:FNR complex together with water detached from Fd and FNR on complexation, and revealed the entropic crosstalk between water and protein dynamics under varying NaCl and H^+ amounts. Information on energetic roles of protein dynamics and dehydration obtained from ITC is markedly important with that obtained from the NMR spectroscopy [24].

3.5. Context-dependent energetic interplay characterized by the driving force plot and its biological relevance

I have shown that the driving force plot is an understandable way to describe how driving forces contribute to ΔG of complex formation particularly when many binding systems are simultaneously compared [3,4,9].

All ΔH_{bind} and ΔS_{bind} obtained at pH 6.0 (Fig. 4B) and 8.0 (Fig. 4D) under the varying NaCl concentration and temperature were plotted to construct the driving force plot for Fd:FNR complexation. Increases in the NaCl concentration and pH decreased the interprotein affinity (i.e., decreases in the magnitude of negative ΔG_{bind}) by guiding unfavorable positive ΔH_{bind} to a favorable direction ("F" in Fig. 4B and D) as well as by shifting favorable positive $T\Delta S_{\mathrm{bind}}$ to an unfavorable direction ("U" in Fig. 4B and D), which suggests that entropy is an energetic modulator for affinity. Meanwhile, effects of the change in temperature on affinity and driving forces were minimal as shown in clustering of data points with the same colors.

Interestingly, driving forces were not distributed vertically or transversely. They lay between ΔG_{bind} lines of -25 and -35 kJ mol^{-1} with strong positive correlations ($R = 0.99$ and $p < 0.01$ at pH 6.0; $R = 0.93$ and $p < 0.01$ at pH 8.0) (Fig. S5) as a result of the enthalpy-entropy compensation. Energetic adaptation to keep the enthalpy-entropy compensation against the change in environmental conditions may produce these correlations. Therefore, the enthalpy-entropy compensation may act as an energetic buffer although too strong perturbation breaks this compensating capacity as observed at pH 8.0 in the presence of 200 mM NaCl.

I discuss thermodynamic findings and functions of Fd and FNR based on physiological situations. The change in pH was the most effective perturbation to alter the affinity and thermodynamic properties than the other exterior stresses within the range of the current study. NaCl was more effective than temperature. At pH 6.0 which corresponds to night where no photosynthesis occurs [17], FNR activity is low and Fd and FNR are both in rest states [15]. I speculate that the formation of the stable complex (i.e., high affinity) at pH 6.0 with ΔG_{bind} of ~-30 kJ mol^{-1} is beneficial from proteolysis. Intrinsically disordered N-terminal region of FNR, susceptible to proteolysis in the chloroplast stroma [25], may be particularly protected as intrinsically disordered proteins form complexes with binding partners to avoid proteolysis [26].

Meanwhile, on a pH increase to 8.0, Fd sequestered by FNR through a strong affinity may be released by a decreased affinity (less than ~-30 kJ mol^{-1} in magnitude) due to entropy losses by ~10-~20 kJ mol^{-1} in spite of enthalpy gains of ~10-~15 kJ mol^{-1}. At pH 7.0-8.0 which is a daytime condition [17], Fd and FNR are active for photosynthesis [15]. Thus, moderately weak interprotein interactions would be advantageous for not only the turnover rate of FNR but also electron distribution by Fd to various Fd-dependent enzymes in chloroplasts [12]. Smaller endothermic enthalpy changes at pH 8.0 (Fig. 4C) than at pH 6.0 by ~10-~15 kJ mol^{-1} would contribute kinetically to FNR activity.

Daily and seasonal temperature differences [18] may influence binding affinity although no significant change in affinity was detected in ranging from 19 to 28 °C. Increases in the NaCl concentration at pH 6.0 still showed relatively strong affinity; however, increasing NaCl concentration to 200 mM at pH 8.0 weakened markedly interactions between Fd and FNR. It is conceivable that moderate NaCl concentrations less than 200 mM at pH 8.0 is more effective for enhancing FNR activity as a result of optimized kinetics and complex configuration as observed in a bell-shaped SiR activity and a monotonic decrease in Fd:SiR affinity depending on the increase in the NaCl concentration [4]. Too strong or weak interprotein interactions would not be effective for enzymatic interactions.

References

[1] M. Winkler, S. Kuhlgert, M. Hippler, T. Happe, Characterization of the key step for light-driven hydrogen evolution in green algae, J. Biol. Chem. 284 (2009) 36620-36627.

[2] Y.H. Lee, T. Ikegami, D.M. Standley, K. Sakurai, T. Hase, Y. Goto, Binding energetics of ferredoxin-NADP$^+$ reductase with ferredoxin and its relation to function, Chembiochem 12 (2011) 2062-2070.

[3] M. Kinoshita, J.Y. Kim, S. Kume, Y. Sakakibara, T. Sugiki, C. Kojima, G. Kurisu, T. Ikegami, T. Hase, Y. Kimata-Ariga, Y.H. Lee, Physicochemical nature of interfaces controlling ferredoxin NADP($^+$) reductase activity through its interprotein interactions with ferredoxin, Biochim. Biophys. Acta. 1847 (2015) 1200-1211.

[4] J.Y. Kim, M. Kinoshita, S. Kume, H. Gt, T. Sugiki, J.E. Ladbury, C. Kojima, T. Ikegami, G. Kurisu, Y. Goto, T. Hase, Y.H. Lee, Non-covalent forces tune the electron transfer complex between ferredoxin and sulfite reductase to optimize enzymatic activity, Biochem. J. 473 (2016) 3837-3854.

[5] J.K. Hurley, M. Faro, T.B. Brodie, J.T. Hazzard, M. Medina, C. Gomez-Moreno, G. Tollin, Highly nonproductive complexes with Anabaena ferredoxin at low ionic strength are induced by nonconservative amino acid substitutions at Glu139 in Anabaena ferredoxin:NADP$^+$ reductase, Biochemistry 39 (2000) 13695-13702.

[6] J.Y. Kim, M. Nakayama, H. Toyota, G. Kurisu, T. Hase, Structural and mutational studies of an electron transfer complex of maize sulfite reductase and ferredoxin, J. Biochem. 160 (2016) 101-109.

[7] I. Jelesarov, H.R. Bosshard, Isothermal titration calorimetry and differential scanning calorimetry as complementary tools to investigate the energetics of biomolecular recognition, J. Mol. Recognit. 12 (1999) 3-18.

[8] T.S. Olsson, M.A. Williams, W.R. Pitt, J.E. Ladbury, The thermodynamics of protein-ligand interaction and solvation: insights for ligand design, J. Mol. Biol. 384 (2008) 1002-1017.

[9] S. Kume, Y.H. Lee, M. Nakatsuji, Y. Teraoka, K. Yamaguchi, Y. Goto, T. Inui, Fine-tuned broad binding capability of human lipocalin-type prostaglandin D synthase for various small lipophilic ligands, FEBS Lett. 588 (2014) 962-969.

[10] P.A. Karplus, M.J. Daniels, J.R. Herriott, Atomic structure of ferredoxin-NADP$^+$ reductase: prototype for a structurally novel flavoenzyme family, Science 251 (1991) 60-66.

[11] P. Mulo, Chloroplast-targeted ferredoxin-NADP($^+$) oxidoreductase (FNR): structure, function and location, Biochim. Biophys. Acta. 1807 (2011) 927-934.

[12] M. Nakayama, T. Akashi, T. Hase, Plant sulfite reductase: molecular structure, catalytic function and interaction with ferredoxin, J. Inorg. Biochem. 82 (2000) 27-32.

[13] A.P. Srivastava, M. Hirasawa, M. Bhalla, J.S. Chung, J.P. Allen, M.K. Johnson, J.N. Tripathy, L.M. Rubio, B. Vaccaro, S. Subramanian, E. Flores, M. Zabet-Moghaddam, K. Stitle, D.B. Knaff, Roles of four conserved basic amino acids in a ferredoxin-dependent cyanobacterial nitrate reductase, Biochemistry 52 (2013) 4343-4353.

[14] G. Kurisu, M. Kusunoki, E. Katoh, T. Yamazaki, K. Teshima, Y. Onda, Y. Kimata-Ariga, T. Hase, Structure of the electron transfer complex between ferredoxin and ferredoxin-NADP($^+$) reductase, Nat. Struct. Biol. 8 (2001) 117-121.

[15] Y.H. Lee, K. Tamura, M. Maeda, M. Hoshino, K. Sakurai, S. Takahashi, T. Ikegami, T. Hase, Y. Goto, Cores and pH-dependent dynamics of ferredoxin-NADP$^+$ reductase revealed by hydrogen/deuterium exchange, J. Biol. Chem. 282 (2007) 5959-5967.

[16] G.M. Soriano, M.V. Ponamarev, G.S. Tae, W.A. Cramer, Effect of the interdomain basic region of cytochrome f on its redox reactions in vivo, Biochemistry 35 (1996) 14590-14598.

[17] A.N. Tikhonov, Energetic and regulatory role of proton potential in chloroplasts, Biochemistry (Mosc) 77 (2012) 956-974.

[18] X.W. Zhang, J.R. Wang, M.F. Ji, R.I. Milne, M.H. Wang, J.Q. Liu, S. Shi, S.L. Yang, C.M. Zhao, Higher thermal acclimation potential of respiration but not photosynthesis in two alpine Picea taxa in contrast to two lowland congeners, PLoS One 10 (2015) e0123248.

[19] M. Maeda, Y.H. Lee, T. Ikegami, K. Tamura, M. Hoshino, T. Yamazaki, M. Nakayama, T. Hase, Y. Goto, Identification of the N- and C-terminal substrate binding segments of ferredoxin-NADP$^+$ reductase by NMR, Biochemistry 44 (2005) 10644-10653.

[20] T. Saitoh, T. Ikegami, M. Nakayama, K. Teshima, H. Akutsu, T. Hase, NMR study of the electron transfer complex of plant ferredoxin and sulfite reductase: mapping the interaction sites of ferredoxin, J. Biol. Chem. 281 (2006) 10482-10488.

[21] G. Schreiber, Kinetic studies of protein-protein interactions, Curr. Opin. Struct. Biol. 12 (2002) 41-47.

[22] M. Aoki, K. Ishimori, H. Fukada, K. Takahashi, I. Morishima, Isothermal titration calorimetric studies on the associations of putidaredoxin to NADH-putidaredoxin reductase and P450cam, Biochim. Biophys. Acta. 1384 (1998) 180-188.

[23] L.J. Jeuken, Conformational reorganisation in interfacial protein electron transfer, Biochim. Biophys. Acta. 1604 (2003) 67-76.

[24] S.R. Tzeng, C.G. Kalodimos, Protein activity regulation by conformational entropy, Nature 488 (2012) 236-240.

[25] W. Sakamoto, Protein degradation machineries in plastids, Annu Rev Plant Biol 57 (2006) 599-621.

[26] C.J. Oldfield, A.K. Dunker, Intrinsically disordered proteins and intrinsically disordered protein regions, Annu. Rev. Biochem. 83 (2014) 553-584.

Supplementary information

Supplementary Results and Discussion

Weak and strong interactions between Fd and FNR where electrostatic interactions are strong.

In order to obtain thermodynamic parameters for the Fd:FNR complex formation, I analyzed almost all data using the one-to-one binding stoichiometry. Interestingly, however, at pH 6.0 with the low ionic strength and temperature at 0 mM NaCl and 19-28°C as well as at 30 mM NaCl and 19-22°C, binding isotherms were best fit to a two-site binding model (**Figs. 2A, B, E** and **S3A, B, E**), which indicated that FNR accommodates two binding sites for Fd. Strong and weak binding were both endothermic in nature, thus, ΔH_{bind} values ranged from 6.9 and 25.5 kJ mol^{-1} for weak binding and from 28.4 and 33.0 kJ mol^{-1} for strong binding (**Table S1**). Thus, complexes were purely driven by positive entropy changes with showing 39.5-72.7 kJ mol^{-1}.

Electrostatic interactions between negatively-charged residues in Fd and positively-charged residues in the N-terminal part of FNR are most likely ascribed to the generation of a weak binding. The long N-terminal part (~40 a.a.) is intrinsically disordered and contains several positively-charged residues conserved among species such as lysine residues at positions 15, 17, 18, 21, 22, and 35. I previously demonstrated that these charged N-terminal residues in FNR are also important for interactions with Fd [2].

Since increasing the salt concentration and temperature weakens electrostatic interactions, the weak binding involved in an N-terminal part becomes abolished by the addition of NaCl more than 30 mM at higher temperatures than 25°C. I observed similar interactions between Fd and sulfite reductase (SiR), one of Fd-dependent enzymes, using ITC [1]. At the low ionic strength, ITC results revealed that several small Fd molecules (~11 kDa) interacts weakly and strongly with one large SiR (~66 kDa) through attractive electrostatic interactions. Increasing a NaCl concentration from 0 to 25 mM led to the dissociation of Fd from weak binding sites on SiR due to wakened intermolecular electrostatic forces.

Supplementary Table

Table S1. Summary of thermodynamic parameters of Fd:FNR complex formation at pH 6.0.

NaCl (mM)	Temperature (˚C)	K_d (μM)	ΔH_bind (kJ mol^{-1})	$T\Delta S_\mathrm{bind}$ (kJ mol^{-1})	ΔG_bind (kJ mol^{-1})	$\Delta C_\mathrm{p,bind}$ (kJ mol^{-1} K^{-1})
0	19	[a]2.2	[a]25.9	[a]57.5	[a]-31.6	-0.67
		[b]0.7	[b]11.8	[b]46.3	[b]-34.5	
		[c]0.1	[c]33.0	[c]72.7	[c]-39.7	
	22	[a]1.6	[a]24.5	[a]57.2	[a]-32.7	
		[b]0.6	[b]11.6	[b]46.7	[b]-35.1	
		[c]0.05	[c]28.4	[c]69.8	[c]-41.4	
	25	[a]2.2	[a]22.5	[a]54.8	[a]-32.3	
		[b]0.4	[b]9.6	[b]46.3	[b]-36.7	
		[c]0.05	[c]31.1	[c]72.6	[c]-41.5	
	28	[a]2.0	[a]19.8	[a]52.7	[a]-32.8	
		[b]0.4	[b]8.1	[b]45.0	[b]-36.9	
		[c]0.06	[c]28.4	[c]70.3	[c]-41.9	
30	19	[a]1.4	[a]25.2	[a]57.8	[a]-32.6	-0.75
		[b]1.4	[b]25.5	[b]58.2	[b]-32.7	
		[c]1.43	[c]31.9	[c]64.5	[c]-32.6	
	22	[a]1.4	[a]24.2	[a]57.4	[a]-33.2	
		[b]1.6	[b]6.9	[b]39.5	[b]-32.7	
		[c]0.89	[c]31.0	[c]65.2	[c]-34.2	
	25	1.8	20.4	53.1	-32.8	
	28	1.4	19.0	52.8	-33.8	
60	19	4.2	21.9	52.0	-30.0	-0.47
	22	3.3	20.4	51.4	-31.0	
	25	4.1	19.9	50.6	-30.8	
	28	2.9	17.5	49.4	-31.9	
100	19	10.5	16.1	44.0	-27.9	-0.11
	22	8.5	14.7	43.3	-28.6	
	25	10.0	15.3	43.9	-28.6	

	28	11.2	14.8	43.3	-28.5	
200	19	21.4	2.6	28.7	-26.1	0.21
	22	35.7	4.0	29.1	-25.1	
	25	15.0	3.3	30.8	-27.5	
	28	41.2	5.0	30.2	-25.3	

[a] Values obtained using a one-to-one binding model between Fd and FNR.

[b] Values at the weak binding site obtained using a one (FNR)-to-two (Fd) binding model.

[c] Values at the strong binding site obtained using a one (FNR)-to-two (Fd) binding model.

Table S2. Summary of thermodynamic parameters of Fd:FNR complex formation at pH 8.0.

NaCl (mM)	Temperature (˚C)	K_d (μM)	ΔH_{bind} (kJ mol^{-1})	$T\Delta S_{bind}$ (kJ mol^{-1})	ΔG_{bind} (kJ mol^{-1})	$\Delta C_{p,bind}$ (kJ mol^{-1} K^{-1})
0	19	2.7	11.7	42.8	-31.1	-0.18
	22	3.3	11.4	42.4	-31.0	
	25	4.0	12.4	43.2	-30.8	
	28	2.8	9.6	41.6	-32.0	
30	19	5.2	9.3	38.7	-29.5	-0.10
	22	4.6	9.3	39.4	-30.1	
	25	5.6	9.5	39.4	-30.0	
	28	4.3	8.2	39.2	-31.0	
60	19	19.5	9.5	35.8	-26.3	0.08
	22	15.3	9.1	36.3	-27.2	
	25	15.8	9.5	36.9	-27.4	
	28	16.9	10.1	37.8	-27.7	
100	19	13.8	3.4	30.6	-27.2	0.02
	22	13.5	3.2	30.6	-27.4	
	25	10.4	3.0	31.4	-28.4	
	28	13.3	3.6	31.8	-28.1	

Table S3. Dissection of entropy changes for Fd:FNR complex formation at pH 6.0.

NaCl (mM)	Temperature (˚C)	$T\Delta^{\mathrm{mix}}S_{\mathrm{bind}}$ (kJ mol^{-1})	$T\Delta^{\mathrm{dehyd}}S_{\mathrm{bind}}$ (kJ mol^{-1})	$T\Delta^{\mathrm{conf}}S_{\mathrm{bind}}$ (kJ mol^{-1})
0	19	-9.8	73.4	-6.2
	22	-9.9	71.4	-4.4
	25	-10.0	69.4	-4.7
	28	-10.1	67.4	-4.7
30	19	-9.8	82.4	-14.8
	22	-9.9	80.2	-12.9
	25	-10.0	77.9	-14.8
	28	-10.1	75.7	-12.8
60	19	-9.8	51.1	10.6
	22	-9.9	49.7	11.5
	25	-10.0	48.4	12.3
	28	-10.1	47.0	12.5
100	19	-9.8	12.2	41.6
	22	-9.9	11.9	41.4
	25	-10.0	11.5	42.4
	28	-10.1	11.2	42.2
200	19	-9.8	-23.2	61.7
	22	-9.9	-22.6	61.6
	25	-10.0	-21.9	62.7
	28	-10.1	-21.3	61.6

$T\Delta S_{\mathrm{bind}}$ and $T\Delta^{\mathrm{mix}}S_{\mathrm{bind}}$ were calculated based on results of direct ITC measurements and entropy of mixing, respectively. $T\Delta^{\mathrm{dehyd}}S_{\mathrm{bind}}$ was obtained using the change in heat capacity (ΔC_{p}) and the relationship, $\Delta^{\mathrm{dehyd}}S_{\mathrm{bind}} = 1.35\Delta C_{\mathrm{p}}\ln(T/386)$ [3], where R is the gas constant and T is the absolute temperature. $T\Delta^{\mathrm{conf}}S_{\mathrm{bind}}$ was calculated using the relationship [3], $T\Delta S_{\mathrm{bind}} = T\Delta^{\mathrm{mix}}S_{\mathrm{bind}} + T\Delta^{\mathrm{dehyd}}S_{\mathrm{bind}} + T\Delta^{\mathrm{conf}}S_{\mathrm{bind}}$ with known values of $T\Delta S_{\mathrm{bind}}$, $T\Delta^{\mathrm{mix}}S_{\mathrm{bind}}$, and $T\Delta^{\mathrm{dehyd}}S_{\mathrm{bind}}$.

Table S4. Dissection of entropy changes for Fd:FNR complex formation at pH 8.0.

NaCl (mM)	Temperature (˚C)	$T\Delta^{\mathrm{mix}}S_{\mathrm{bind}}$ (kJ mol^{-1})	$T\Delta^{\mathrm{dehyd}}S_{\mathrm{bind}}$ (kJ mol^{-1})	$T\Delta^{\mathrm{conf}}S_{\mathrm{bind}}$ (kJ mol^{-1})
0	19	-9.8	19.5	33.0
	22	-9.9	19.0	33.2
	25	-10.0	18.5	34.7
	28	-10.1	17.9	33.7
30	19	-9.8	11.2	36.2
	22	-9.9	10.9	37.6
	25	-10.0	10.6	38.4
	28	-10.1	10.3	39.0
60	19	-9.8	-8.6	53.1
	22	-9.9	-8.4	53.9
	25	-10.0	-8.1	54.7
	28	-10.1	-7.9	55.8
100	19	-9.8	-2.2	41.6
	22	-9.9	-2.1	42.0
	25	-10.0	-2.1	43.2
	28	-10.1	-2.0	43.9

ΔS_{bind} and $T\Delta^{\mathrm{mix}}S_{\mathrm{bind}}$ were calculated based on results of direct ITC measurements and entropy of mixing, respectively. $T\Delta^{\mathrm{dehyd}}S_{\mathrm{bind}}$ was obtained using the change in heat capacity (ΔC_{p}) and the relationship, $\Delta^{\mathrm{dehyd}}S_{\mathrm{bind}} = 1.35\Delta C_{\mathrm{p}}\ln(T/386)$ [3], where R is the gas constant and T is the absolute temperature. $T\Delta^{\mathrm{conf}}S_{\mathrm{bind}}$ was calculated using the relationship [3], $T\Delta S_{\mathrm{bind}} = T\Delta^{\mathrm{mix}}S_{\mathrm{bind}} + T\Delta^{\mathrm{dehyd}}S_{\mathrm{bind}} + T\Delta^{\mathrm{conf}}S_{\mathrm{bind}}$ with known values of $T\Delta S_{\mathrm{bind}}$, $T\Delta^{\mathrm{mix}}S_{\mathrm{bind}}$, and $T\Delta^{\mathrm{dehyd}}S_{\mathrm{bind}}$.

Supplementary Figure

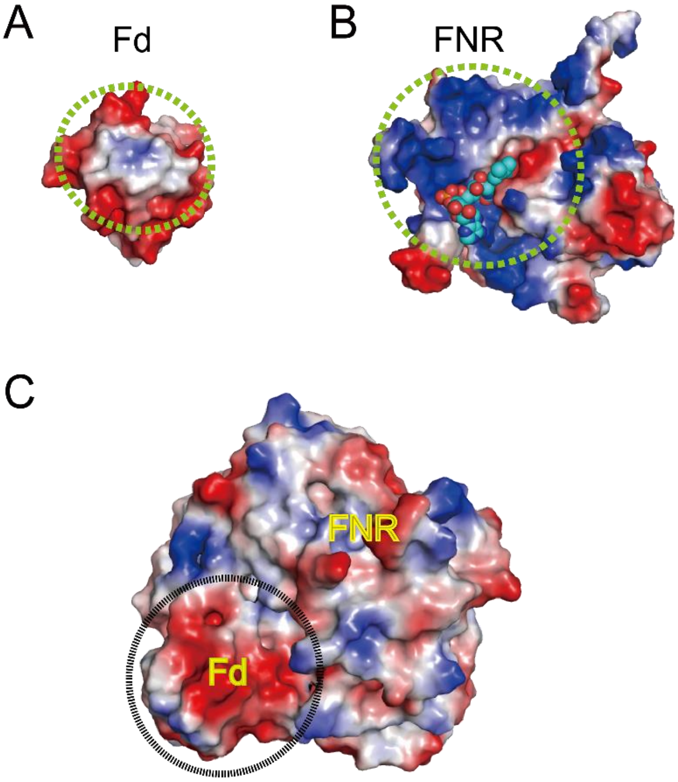

Fig. S1. Crystal structures of Fd and FNR in free and complex states.

Three dimensional structures of Fd (1GAW) (A) and FNR (1GAW) (B) in free states and the Fd:FNR complex (1GAQ) (C) are shown with space-filling models [4]. Positive and negative electrostatic surface potentials are colored in blue and red, respectively. Binding sites on Fd for FNR and on FNR for Fd are indicated with broken circles in each free structure. FNR-bound Fd is also indicated using the broken circle in C.

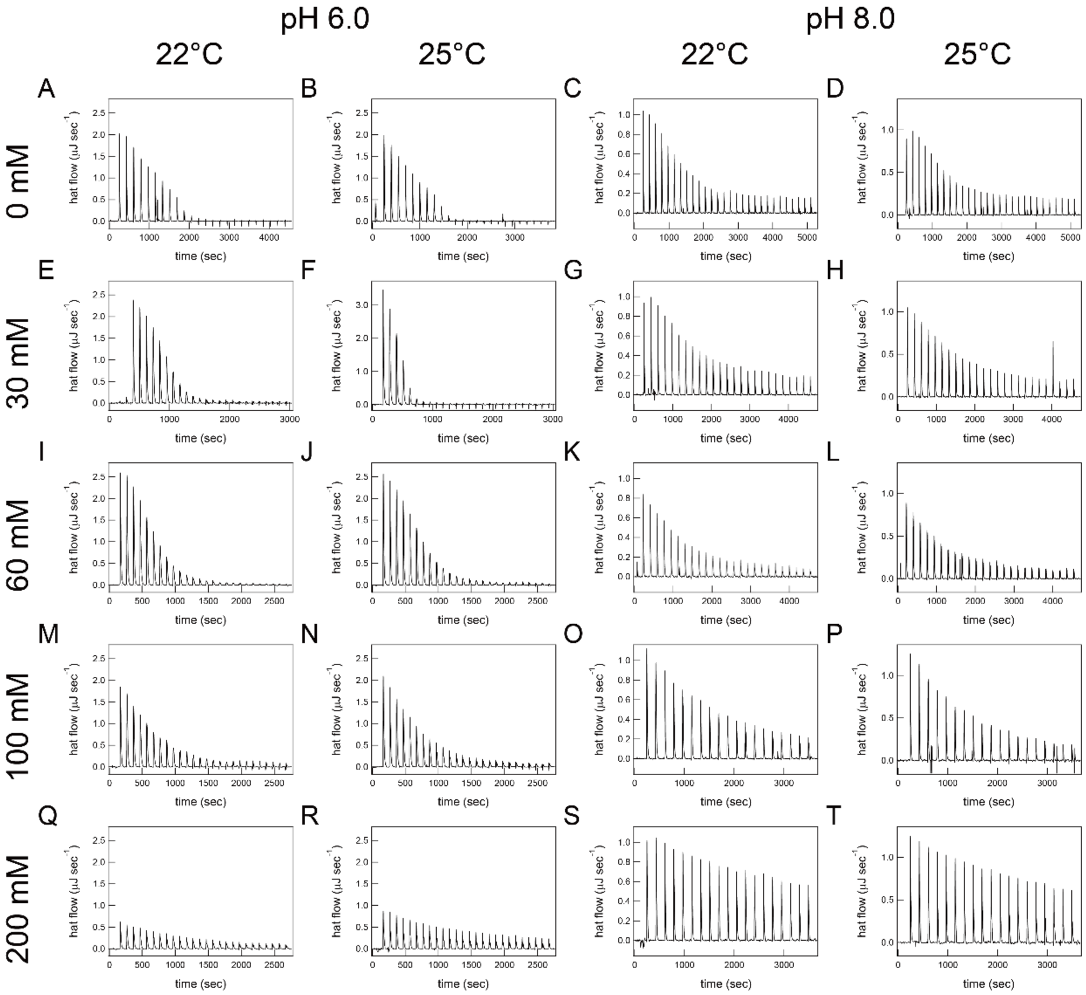

Fig. S2. ITC thermograms of Fd titration to FNR at various conditions.

ITC thermograms of the titration of Fd to FNR obtained at 22 (A, C, E, G, I, K, M, O, Q, and S), 25°C (B, D, F, H, J, L, N, P, R, and T) under distinct pH values (pH 6.0 (A, B, E, F, I, J, M, N, Q, and R) and 8.0 (C, D, G, H, K, L, O, P, S, and T)) in the presence of 0 (A-D), 30 (E-H), 60 (I-L), 100 (M-P), and 200 mM NaCl (Q-T).

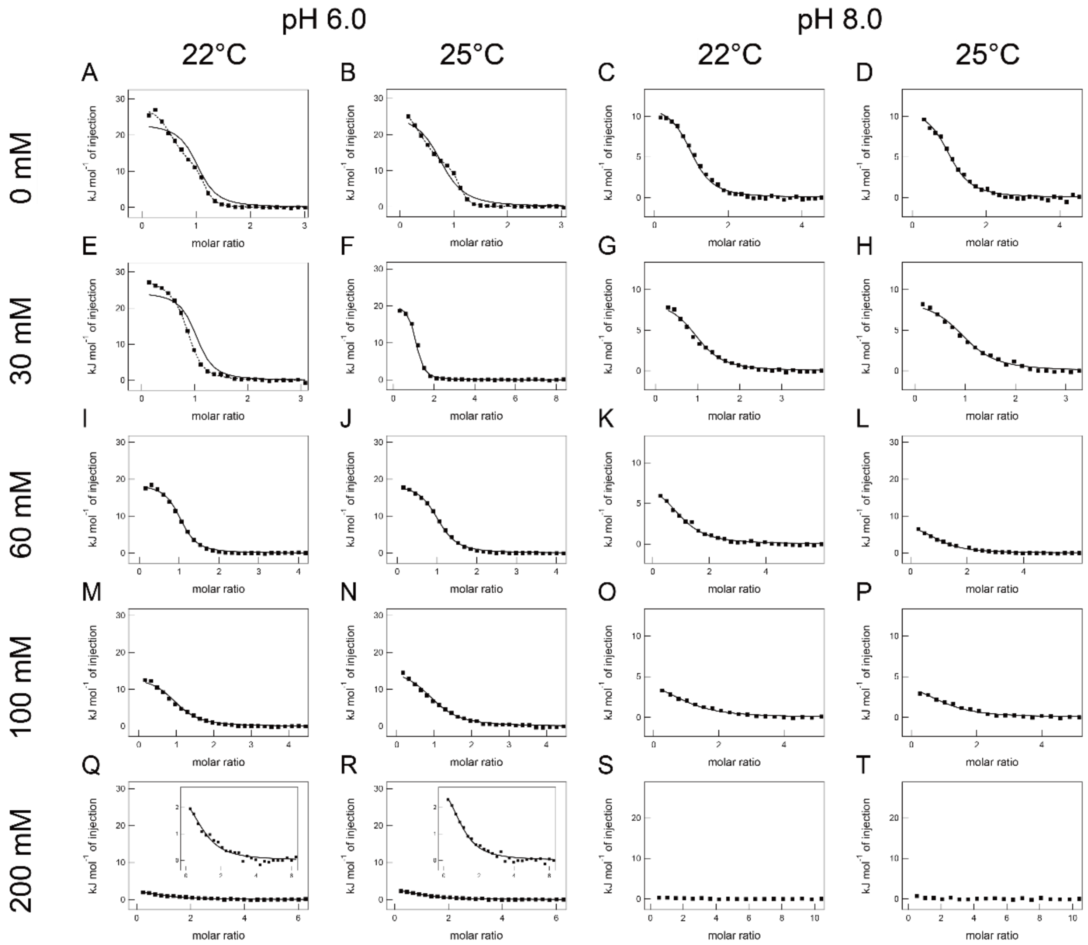

Fig. S3. Fd:FNR binding isotherms obtained using ITC at various conditions.

Fd:FNR binding isotherms obtained at 22 (A, C, E, G, I, K, M, O, Q, and S), 25°C (B, D, F, H, J, L, N, P, R, and T) under distinct pH values (pH 6.0 (A, B, E, F, I, J, M, N, Q, and R) and 8.0 (C, D, G, H, K, L, O, P, S, and T)) in the presence of 0 (A-D), 30 (E-H), 60 (I-L), 100 (M-P), and 200 mM NaCl (Q-T). Fit curves based on one-to-one and one-to-two binding models between Fd and FNR are shown with solid and dotted lines. Normalized values and fit curves in Q and R magnified are shown in insets.

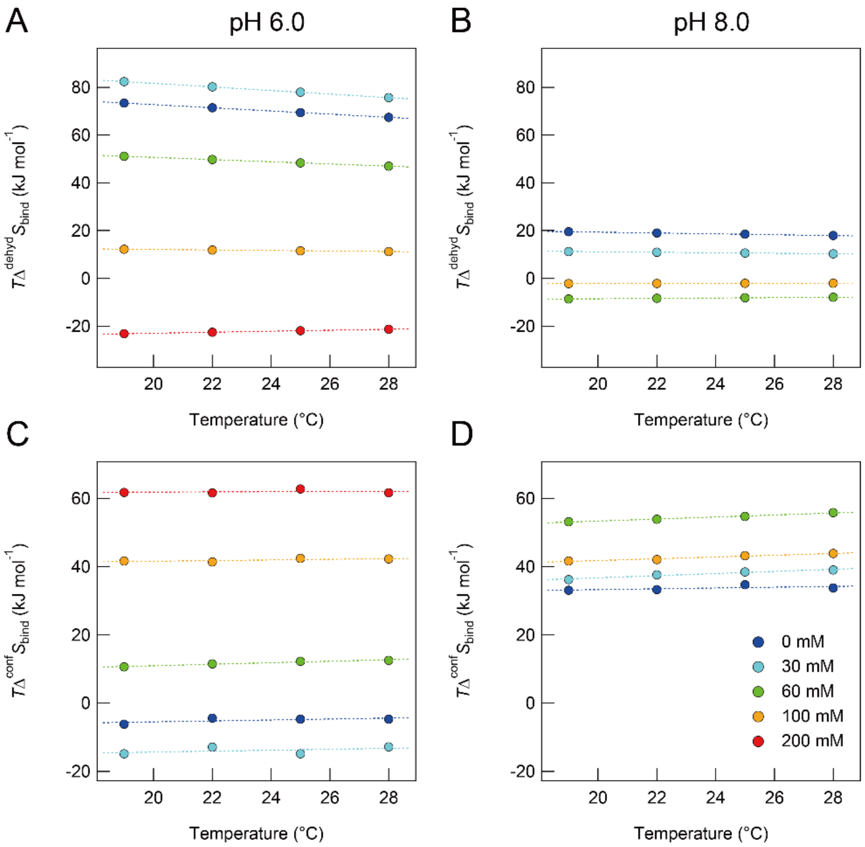

Fig. S4. Hydrational and conformational entropy changes upon Fd:FNR complex formation at various conditions.

Entropy change in hydration ($T\Delta^{\text{dehyd}}S_{\text{bind}}$) in pH 6.0 (A) and 8.0 (B) and conformation ($T\Delta^{\text{conf}}S_{\text{bind}}$) in pH 6.0 (C) and 8.0 (D) were plotted against temperature. Data obtained at distinct NaCl concentrations are represented with the color code. Dotted straight lines were drawn for indicating comprehensively a trend in changes.

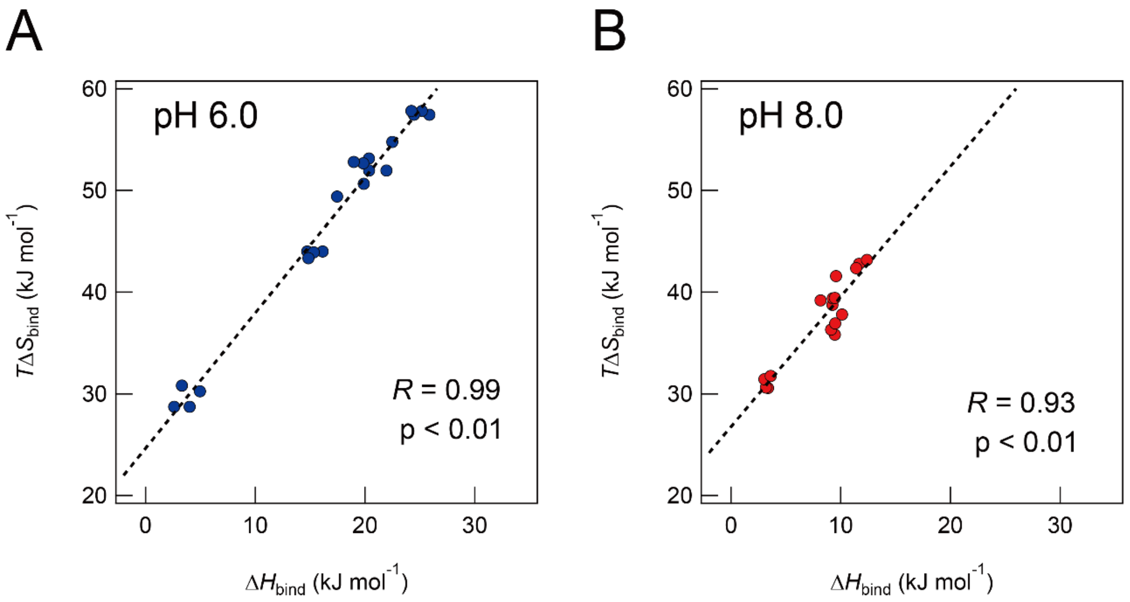

Fig. S5. Correlation between enthalpy changes and entropy changes.

Correlation coefficient (R) and significance (p) for the enthalpy-entropy compensation at pH 6.0 (A) and 8.0 (B) are shown.

Chapter 4

Energy landscapes of amyloid formation of β2-microglobulin.

Abstract

Misfolding-induced amyloid formation has shown to be responsible for more than 40 deleterious disorders. Amyloid structures and underlying mechanisms of amyloidogenesis have been increasingly revealed; however, the study on amyloid formation in terms of thermodynamics, kinetics, and polymorphism with a simple and effective method remains largely limited.

Thus, in order to have insights into amyloid generation based on thermodynamics and kinetics, I herein performed thermodynamic and kinetic studies on amyloid fibril formation of β2-microglobulin (β2m), which is a causative protein of dialysis-related amyloidosis, using isothermal titration calorimetry (ITC). All ITC isotherms at various temperatures, stirring speeds, and concentrations of crowders showed exothermic reactions after lag phase. β2m solution following ITC experiments exhibited high ThT fluorescence, far-UV CD spectra of cross-β structures, and fibrillar aggregates in AFM images, indicating that exothermic heat was ascribed to the spontaneous formation of β2m amyloid fibrils.

Detailed analyses of ITC peaks produced thermodynamic and kinetic parameters of nucleation-dependent amyloid fibrillation. Negative values of the enthalpy change (ΔH), which thus indicated enthalpy-driven amyloid formation, were estimated at all conditions and the heat capacity change was obtained temperature-dependent ΔH. Rate constants as well as activation energy of nucleation and fibril elongation were also estimated. Enhanced shear force by stirring caused the increase in the magnitude of negative ΔH and promoted nucleation without affecting elongation kinetics. The addition of ficoll also increased the magnitude of negative ΔH and accelerated nucleation in a dose-dependent manner although fibril growth adversely slowed down. These results indicated the formation of amyloid fibrils which were thermodynamically and kinetically distinguishable, namely polymorphic amyloidogenesis, which was not discriminated by ThT fluorescence, CD spectra, AFM analyses.

Energy landscape of spontaneous β2m amyloid generation was constructed by incorporating thermodynamic and kinetic parameters and was comprehensively compared to that of β2m folding. Polymorphic energy landscape well illustrated that different packing density in fibril cores produced thermodynamically and structurally distinct amyloid fibrils with the kinetic control of amyloid formation by nucleation and elongation. I finally suggest that state-of-the-art application of ITC to protein misfolding and aggregation provides us unprecedented opportunity to improve our understanding of amyloidogenesis.

1. Introduction

Soluble proteins in native states are functional and major players for countless biological and cellular processes. Nature has evolved to keep proteins functional and soluble by efficient clearance of misfolded and aggregated proteins and to aid to make misregulated proteins correctly folded to native structures in terms of homeostasis [1, 2]. However, errors and failure in the quality control, which become frequent and serious with aging and stresses, often lead to protein misfolding and concurrent aggregation [2]. Deposition of insoluble protein aggregates and aggregation process themselves cause a number of diseases, so-called protein misfolding disease, and dysfunction of proteins by damaging organelles, cells, tissues, and organs.

Proteins aggregates are largely classified to fibrillar aggregates and amorphous aggregates based on morphology, structure, and kinetic processes [3-5]. Amyloid fibrils are best studied protenious fibrillar aggregates as they have been strongly implicated to many diseases such as neurodegenerative disorders including Alzheimer`s and Parkinson`s diseases and amyloidosis such as dialysis-related amyloidosis [6]. Mature amyloid fibrils consist of several protofillaments containing β-sheets as revealed by several biophysical methods including solid-state NMR spectroscopy, X-ray crystallography, atomic force microscopy (AFM), and (cryo)-electron microscopy (EM). β-sheets are predominantly stabilized by a number of intermolecular hydrogen bonds among constituent monomers.

On the other hand, amorphous aggregates show mostly globular and spherical morphologies without specific structures although internal secondary structures of β-strands are observed to some extent [3-5]. Thus, toxic or non-toxic oligomers are often classified to amorphous aggregates. Curve-linear protofibrils, also referred to as immature fibrils, are fibrillar aggregates, and display shared properties of mature amyloid fibrils and amorphous aggregates. Three-dimensional crystals of correctly-folded native proteins tend to be excluded from the definition of protein aggregates since they are not closely related to pathogenesis.

Protein aggregates are also categorized according to apparent kinetics of self-assembling processes [3-5]. Amyloid fibrils form through two-step reactions and they grow rapidly after productive nucleation which produces the lag time while, in most cases, amorphous aggregation occurs without the appreciable lag time. Context-dependent nucleation induces multiple types of amyloid fibrils, i.e., polymorphs of amyloid fibrillation. A series of innovative studies have suggested that solubility and supersaturation are fundamental factors in understanding protein aggregation [3-5, 7]. Proteins over the solubility limit must form insoluble aggregates such as amyloid fibrils from the thermodynamic point of view. However, apparently soluble proteins prior to the phase transition to insoluble solid states are often detected due to kinetic trapping by the metastability of supersaturation, which is certainly linked to the cause and effect relationship with the nucleation and lag time[3, 4, 7]. Outer factors such as biological membranes, hydrophobic surfaces, or agitation/cavitation have shown to promote amyloid formation by disrupting the metastability of supersaturation [8, 9].

Thus, although detailed thermodynamic and kinetic studies are expected to reveal underlying and general natures of amyloid generation, knowledge and information are largely limited compared to extensive studies of protein (un)folding and stability due mainly to experimental difficulties coming from huge sizes and heterogeneity of amyloid fibrils [10, 11]. Supramolecular assemblies of amyloid fibrils often hamper the application of a lot of key biophysical methods such as solution NMR spectroscopy and hydrodynamics. Furthermore, the application of calorimetry such as differential scanning calorimetry (DSC), which has been recognized as the most powerful approach to studying thermodynamics of globular proteins, did not meet the demand of convincing results [12, 13]. Polymorphs of amyloid fibrillation in sample solution has been the bottleneck in the accurate and precise analyse and interpretation.

All these situations encouraged me to examine the thermodynamics and kinetics of amyloid formation and polymorphic natures of amyloidogenesis by using an effective and convincing methods. Lee and co-workers previously studied thermodynamics of protein aggregation using isothermal titration calorimetry (ITC) [14, 15]. They succeeded in estimating thermodynamic parameters and characterizing thermodynamic stability of aggregates formed from several amyloidogenic proteins and peptides against temperature[14]. Thus, based on this method, I performed in-depth ITC-based study for thermodynamics and kinetics of nucleation-limited amyloidogenesis of β2m under various conditions by taking advantage of several functions of a brand new ITC instrument, and aimed to establish the ITC-based method. I succeeded in observing heat accompanying amyloid formation and estimating thermodynamic and kinetic parameters. By using thermodynamic and kinetic parameters, I constructed the energy landscape of amyloid formation and compared it to that of β2m folding with description of pathogenic relevance. Polymorphic amyloid formation, which was otherwise detected using other approaches used in this study, was revealed by different thermodynamic and kinetic parameters and illustrated by constructing the comprehensive energy landscape.

2. Materials and Methods

2.1. Reagents and proteins

ThT and ficoll were obtained from Wako Pure Chemical Industries Ltd. (Osaka, Japan) and all other reagents were purchased from Nacalai Tesque (Kyoto, Japan). Recombinant human β_2-microglobulin (β2m) with an additional methionine residue at the N terminus was expressed in *Escherichia coli* and purified based on our previous study [30]. The concentration of β2m was determined using a molar extinction coefficient of 19,300 $M^{-1}\cdot cm^{-1}$ a t 280 nm calculated from amino acid sequence data and absorbance.

2.2. ITC measurements

ITC measurements for spontaneous amyloid formation of β2m of 3.5 $mg\cdot ml^{-1}$ dissolved in 10 mM HCl solution (pH 2.0) were carried out using a PEAQ-ITC instrument (Marvern Instrument, UK) at the desired temperatures, stirring speeds, and concentrations of ficoll. 2.2 μl of the 10 mM HCl solution containing 1 M NaCl in the syringe was consecutively injected to the β2m monomer solution in the cell after a 15 min initial delay for thermal equilibration. In order to minimize the influence of residual bubbles and imperfect solution filling the syringe, the first titration was conducted using 0.77 μl of solution in the syringe. Eleven NaCl titrations, spaced at intervals of 300 s, were performed with a duration of 1.54 s for the first titration and 4.4 s for the others to reach the final NaCl concentration of 100 mM. Changes in the heat flow were observed in real time with 10 $\mu cal\cdot s^{-1}$ of reference power.

2.3. ThT assay

The formation of β2m amyloid fibrils was monitored by a fluorometric assay of ThT at 37 °C. Excitation and emission wavelengths were 445 and 485 nm, respectively. 10 μl aliquots were taken from the ITC cell following incubation and mixed with 1.99 ml of 5 μM ThT in 50 mM glycine-NaOH buffer (pH 8.5). ThT fluorescence spectra were measured using a F7000 fluorescence spectrophotometer (Hitachi, Japan).

2.4. CD measurements

Far-UV circular dichroism (CD) spectra of 0.1 $mg\cdot ml^{-1}$ β2m in 10 mM HCl solution (pH 2.5) containing 100 mM NaCl before and after ITC measurements at desired temperatures were obtained using a JASCO J820 spectropolarimeter (Tokyo, Japan) and quartz cuvette with a 0.1-cm pathlength. A cell holder equipped with a water circulator was used to keep the sample temperature constant at desired temperatures. Spectra were presented as mean residue ellipticity, [θ] (deg cm^2 dmol^{-1}) after subtraction of the solvent background.

2.5. AFM measurements

A 20-μl aliquot of the β2m sample solution diluted to 0.1 mg·ml^{-1} following ITC measurements was applied to a mica plate. The residual solution was removed after 1 min, and the mica surface was washed twice using 200 μl of water and dried with compressed air. AFM images were obtained using Nanoscope IIIa (Bruker, Germany). Distribution of the height of amyloid fibrils formed at each condition was obtained by using Igor with an in-house algorithm.

3. Results

3.1. Monitoring and thermodynamic analyses of β2m amyloid formation using ITC at different temperatures

Aggregation of acid-denatured β2m was traced using ITC at the various temperature and 1,000 rpm (Fig. 1A). NaCl in the ITC syringe was titrated to solution of β2m monomers in the ITC cell to make β2m solution supersaturated by decreasing the solubility of β2m monomers [16], which produced heat of dilution with sharp and intense ITC peaks. ITC baselines in the ITC thermograms at all temperatures were kept constant for several hours and exothermic negative ITC peaks were subsequently detected. No further changes in ITC thermograms were obtained, indicating the end of reaction in equilibrium. Apparent exothermic ITC peaks appeared early and became larger as incubation temperatures were incremented from 28 to 40 °C.

In order to investigate the origin of exothermic heat and molecular species after incubation in the ITC cell under the shear force generated by ITC stirring, β2m samples were characterized using several biophysical approaches (Fig. 1B and C). ThT fluorescence intensities increased obviously and a number of fibrillar aggregates were observed (Fig. 1B). Far-UV CD spectra of unstructured β2m monomers displayed large changes with negative minima of CD signals in 210-220 nm, suggestive of formation of β-structured molecular species (Fig. 1C).

All these results demonstrated that nucleation-dependent spontaneous formation of β-structured amyloid fibrils of β2m by showing exothermic heat. It was also revealed that metastability of supersaturated β2m solution was effectively disrupted by agitation of ITC stirrer and thereby inducing productive nucleation of amyloidogenesis.

Reversibility of β2m amyloid formation was confirmed using thermal denaturation of preformed β2m amyloid fibrils (Fig. S1). β2m amyloid fibrils melt to monomers at high temperature by showing the sigmoidal heat denaturation curve based on the CD intensity at 213 nm (Fig. S1A). Cooling down to 37 °C where amyloid fibrils were prepared and further incubation restored the intensity of CD signal, suggesting that amyloid formation is a reversible process which ensured thermodynamic analyses(Fig. S1A).

Thermodynamic analyses of β2m amyloidogenesis were performed after the baseline correction using our algorithm and normalization, which gave the change in enthalpy (ΔH) of -328, -254, -313, -391, and -407 kJ mol^{-1} at 28, 31, 34, 37, and 40 °C, respectively (Fig. 1D, Table. 1). The negative value of ΔH of β2m amyloid formation was consistent with our previous studies of amyloidogenic proteins and peptides [14, 15]. The change in heat capacity (ΔC_p) of -9.8 kJ mol^{-1} K^{-1} was obtained from the slope of temperature dependence of ΔH (Fig. 1D).

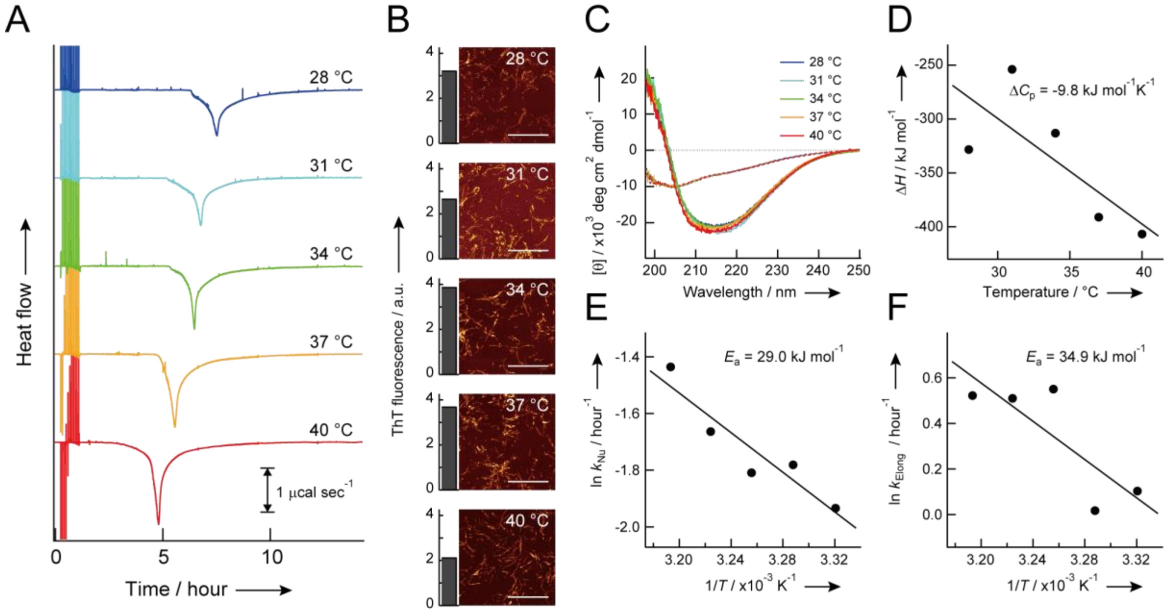

Fig. 1. Isothermal calorimetric examination of β2m amyloid formation at distinct temperatures.
(A) ITC thermograms of β2m amyloid formation at 28, 31, 34, 37, and 40 °C with the stirring speed of 1,000 rpm. (B and C) Characterization of β2m sample solutions after incubation in ITC cells using ThT fluorescence intensities (B, left), AFM images (B, right), and solid lines in far-UV CD spectra (C). The scale bars in AFM images indicate 2 μm. Far-UV CD spectra of β2m monomers at distinct temperatures before incubation are shown with broken lines in C. (D-F) Temperature dependence of ΔH (D), $\ln k_{Nu}$ (E), and $\ln k_{Elong}$ (F) is shown. The solid straight line in D indicates the fit curve based on the relationship, $\Delta C_p = \partial H / \partial T$. (E) The fit straight lines in E and F are obtained using the relationship, $-E_a/R = \partial(\ln k)/\partial T$. Values of ΔC_p, $E_{a,Nu}$, and $E_{a,Elong}$ are displayed in D, E, and F, respectively.

3.2. Monitoring and thermodynamic analyses of β2m amyloid formation using ITC at different shear forces

In order to examine effects of shear forces which influence protein stability and aggregation on β2m aggregation, a series of ITC measurements at 37 °C were performed by changing the speed of stirring from 600 to 1,400 rpm (Fig. 2A). At all stirring speeds, the similar ITC pattern in thermograms was observed: stage I. dilution heat of NaCl; stage II. lag time (no reaction heat); stage III. exothermic reaction; stage IV. stationary phase (no reaction heat). However, the increase in the stirring speed caused generally earlier and larger exothermic ITC peaks.

Increases in ThT fluorescence and fibrillar aggregates in AFM images with far-UV CD spectra of cross-β structures of β2m solution after ITC measurements (Fig. 2B and C) suggested that amyloid formation was accompanied by release of heat. There was no remarkable changes in ThT fluorescence and far-UV CD spectra with the increase in the stirring speed although the CD spectrum obtained at 600 rpm showed the slightly distinct spectrum at different stirring speeds. Interestingly, thermodynamic analyses of exothermic heat revealed that the magnitude of negative Δ*H* of nucleation-dependent spontaneous amyloid generation increased with the increase in the stirring speed. Δ*H* values were estimated to -308, -399, -391, -500, and -561 kJ mol^{-1} at 600, 800, 1,000, 1,200, and 1,400 rpm, respectively (Fig. 2D).

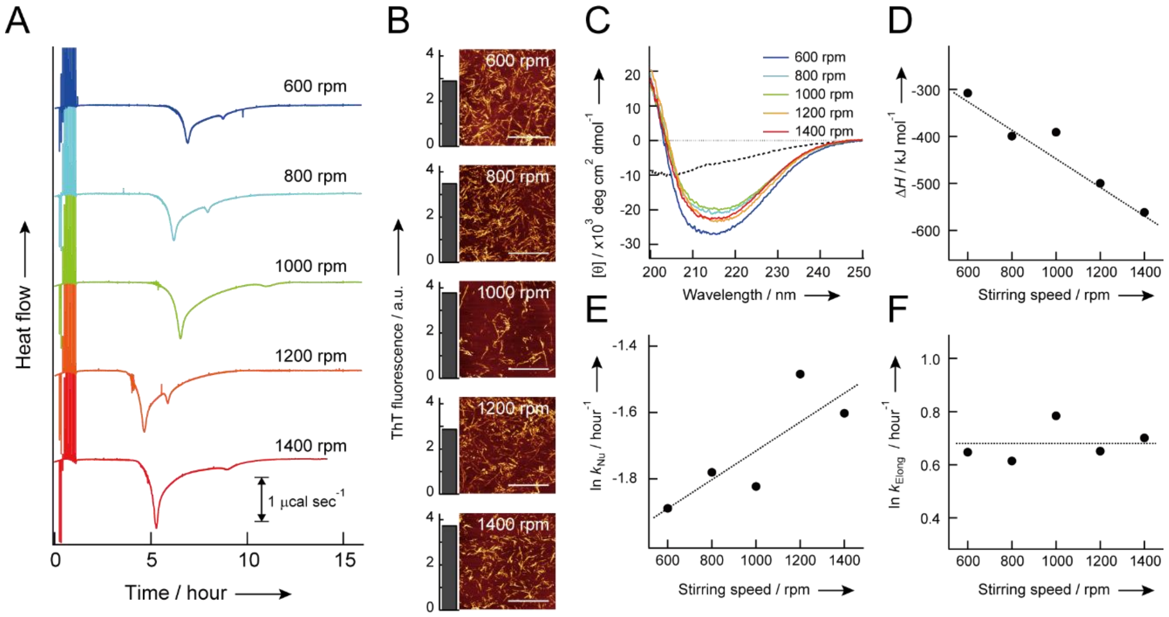

Fig. 2. Dependencies of the observed heat of β2m amyloid formation on the various stirring.
(A) ITC thermograms of β2m amyloid formation at 600, 800, 1,000, 1,200, and 1,400 rpm at 37 °C. (B and C) Characterization of β2m sample solutions after incubation in ITC cells using ThT fluorescence intensities (B, left), AFM images (B, right), and solid lines in far-UV CD spectra (C). The scale bars in AFM images indicate 2 μm. The far-UV CD spectrum of β2m monomers before incubation is shown with the broken black curve in *C*. (D-F) Stirring speed dependence of Δ*H* (D), lnk_{Nu} (E), and lnk_{Elong} (F) is shown. Broken straight black lines in D-F were drawn for eye-guide.

3.3. Monitoring and thermodynamic analyses of β2m amyloid formation using ITC under crowded milieus

Amyloid formation under physiological conditions was also examined using ITC. Iperformed ITC measurements by adding ficoll (0, 0.1, 0.2, and 0.3 g ml^{-1}) which has been used for mimicking crowded conditions [17] to β2m solution in the ITC cell at 37 °C and 1,000 rpm (Fig. 3). ITC thermograms showed clearly a single exothermic ITC peak after the dilution heat and lag time even in the presence of crowders.

Enhancements in ThT fluorescence, fibrillar aggregates in AFM images, and far-UV CD spectra of cross-β structures of β2m solution incubated in the ITC cell (Fig. 3B and C) again demonstrated exothermic amyloid formation. No marked differences in ThT fluorescence and far-UV CD spectra depending on the concentration of ficoll were detected although the far-UV CD spectrum in the absence of ficoll was different from that in the presence of ficoll to some extent. Increments in the concentration of ficoll appeared to promote amyloid formation with the larger magnitude of negative ΔH. ΔH values were calculated to -379, -362, -653, and -696 kJ mol^{-1} at 0.0, 0.1, 0.2, and 0.3 g ml^{-1}, respectively (Fig. 3D).

Effects of ficoll on structural states of β2m monomers before ITC measurements were examined using the far-UV CD (Fig. 3C) and solution NMR spectroscopies (Fig. S2). No changes in uncharacteristic CD spectra and chemical shifts in one-dimensional proton NMR spectra of β2m solution were observed, indicating no structural changes at the atomic and secondary structure level.

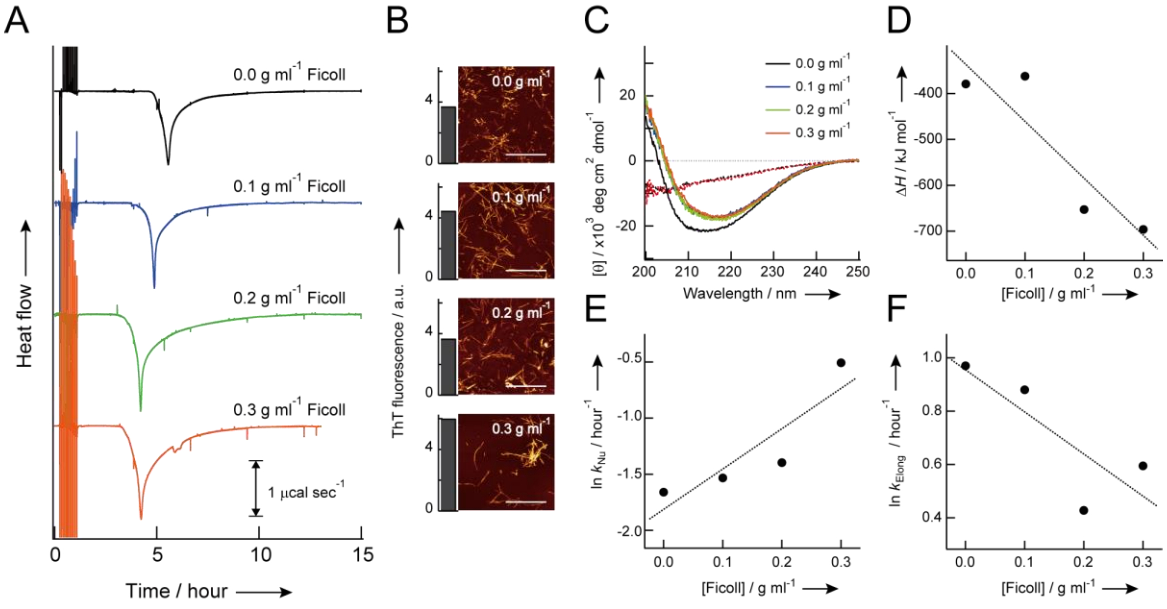

Fig. 3. Ficoll concentration-dependent β2m amyloid formation monitored by ITC.
(A) ITC thermograms of β2m amyloid formation in the presence of Ficoll at 0.0, 0.1, 0.2, and 0.3 g ml^{-1} and 37 °C with the stirring speed of 1,000 rpm. (B and C) Characterization of β2m sample solutions after incubation in ITC cells using ThT fluorescence intensities (B, left), AFM images (B, right), and solid lines in far-UV CD spectra (C). The scale bars in AFM images indicate 1 μm. Far-UV CD spectra of β2m monomers with (black) and without (red) Ficoll of 0.1 g ml^{-1} before incubation are shown with broken curves. (D-F) Ficoll concentration-dependent ΔH (D), $\ln k_{Nu}$ (E), and $\ln k_{Elong}$ (F) is shown. Broken straight lines in D-F were drawn for eye-guide.

3.4. Characterization of morphologies of β2m amyloid fibrils

I could not elucidate differences in the morphology and structure of amyloid fibrils formed at various experimental conditions (Fig. 1A-C, Fig. 2A-C, and Fig. 3A-C). Eye-based observation of amyloid fibrils in AFM images was difficult to provide detailed information on morphological properties of amyloid fibrils. Thus, in order to examine morphologies of amyloid fibrils of β2m after ITC measurements, AFM analyses were performed by constructing histograms of heights of amyloid fibrils (Figs. S3-5).

Fraction of amyloid fibrils was plotted against heights and average heights obtained using Gaussian fit were further plotted as a function of temperature, elucidating that heights of amyloid fibrils formed at distinct temperature were mainly distributed to approximately 3 nm without showing remarkable differences in heights (Fig. S3). Similarly, amyloid fibrils generated at distinct stirring speeds (Fig. S4) or concentration of ficoll (Fig. S5) showed the average height of approximately 3 nm with no significant difference.

3.5. Kinetic analysis of formation of β2m amyloid fibrils using ITC thermograms

Recent innovative studies reported that ITC was used for kinetic analyses of enzyme catalysis and intermolecular interactions [17]. I here performed kinetic analyses of amyloid formation using the ITC peaks, and estimated kinetic parameters, the nucleation rate constant (k_{Nu}), elongation rate constant (k_{Elong}), and activation energy of nucleation ($E_{\mathrm{a,Nu}}$) and fibril elongation ($E_{\mathrm{a,Elong}}$) (Fig. 1E and F, Fig. 2E and F, and Fig. 3E and F).

Kinetic analyses showed dynamic responses of kinetic parameters upon being exposed to exogenous stresses. k_{Nu} was obtained using the lag time (t_{lag}) (Fig. S6) and fit of the ITC peak decaying to the baseline with a single exponential equation produced k_{Elong}. Increases in temperature enhanced linearly k_{Nu} from 0.14 at 28 °C to 0.24 at 40 °C (Fig. 1E) by decreasing t_{lag} (Fig. S6A) and k_{Elong} from 0.1 at 28 °C to 0.52 at 40 °C (Fig. 1F), indicating that increases in temperature promoted amyloid formation. $E_{\mathrm{a,Nu}}$ (Fig. 1E) and $E_{\mathrm{a,Elong}}$ (Fig. 1F) were obtained from the linear dependence of k_{Nu} and k_{Elong} on temperature, respectively.

Enhancement of shear forces accelerated gradually nucleation by increasing k_{Nu} from 0.15 at 600 rpm to 0.20 at 1,400 rpm (Fig. 2E); however, k_{Elong} of about 0.68 was obtained irrespective of the stirring speed (Fig. 2F). Thus, apparent kinetic promotion of amyloid formation by shear force was ascribed to the nucleation step than fibril growth. Ficoll showed similar effects of promotion of nucleation (Fig. 3E) as observed at various either temperature or shear force. Nucleation became faster from 0.19 at 0.0 g ml^{-1} of ficoll to 0.60 at 0.3 g ml^{-1} of ficoll. However, elongation slowed down with the increase in the concentration of ficoll from 0.97 at 0.0 g ml^{-1} of ficoll to 0.59 at 0.3 g ml^{-1} of ficoll.

4. Discussion

4.1. Energy landscape of incorrect folding-induced amyloidogenesis and correct folding of β2m

I here could estimate simultaneously thermodynamic and kinetic parameters of nucleation-dependent spontaneous amyloid formation of β2m in equilibrium by analyzing single ITC peaks obtained various conditions. By incorporating all thermodynamic (ΔH and ΔC_p) and kinetic parameters (k_{Nu}, k_{Elong}, $E_{a,Nu}$, and $E_{a,Elong}$), the energy landscape of misfolding-induced amyloid formation was constructed and compared to that of folding-steered formation of β2m native structures (Fig. 4).

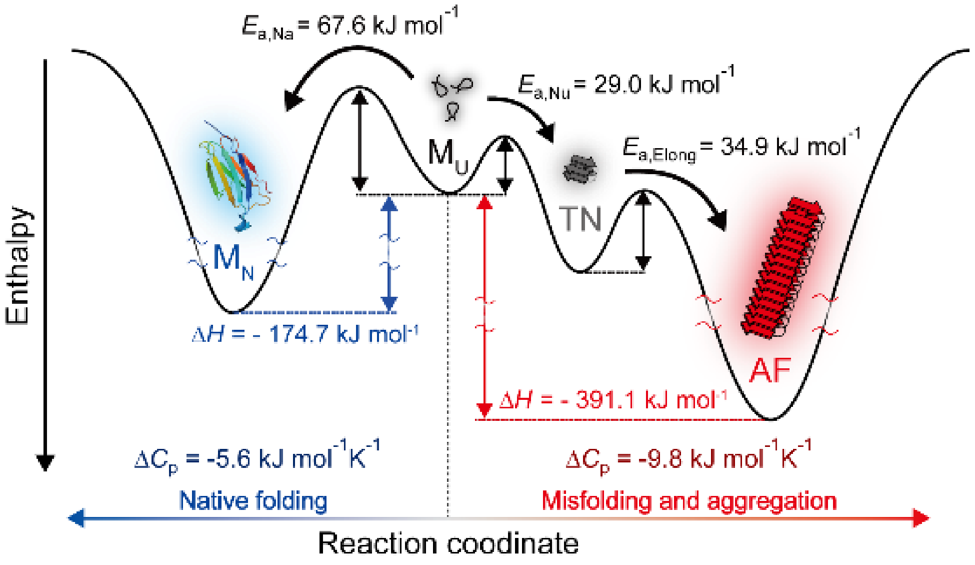
Ea,Na = 67.6 kJ mol-1
Ea,Nu = 29.0 kJ mol-1
Ea,Elong = 34.9 kJ mol-1
MU
TN
MN
AF
Enthalpy
ΔH = - 174.7 kJ mol-1
ΔH = - 391.1 kJ mol-1
ΔCp = -5.6 kJ mol-1K-1
ΔCp = -9.8 kJ mol-1K-1
Native folding
Misfolding and aggregation
Reaction coodinate

Fig. 4. Comparison of energy landscapes of β2m folding and misfolding-induced amyloid formation. Energy landscapes of β2m folding (left) and amyloidogenesis (right) are schematically depicted. Activation energy for β2m folding ($E_{a,Na}$) from the *cis* conformation (ref) on the left as well as for template formation after the nucleation ($E_{a,Nu}$) and fibril growth ($E_{a,Elong}$) on the right is represented with double-headed black arrows and numerical values. The ΔH value of formation of native structures at 37 °C (ref) and amyloid fibrils at 37 °C and a stirring speed of 600 rpm is also indicated with double-headed blue and red arrows, respectively. Unfolded (M_U) and native β2m monomers (M_N) (PDB ID: 2YXF) [31] as well as templates after nucleation (TN) and mature amyloid fibrils (AF) of β2m are shown with cartoons. ΔC_p values of native folding and amyloid formation of β2m are also represented.

Two-step amyloid formation at acidic pH was kinetically controlled by two energy barriers with similar activation energies, $E_{a,Nu}$ of 29 kJ mol^{-1} and $E_{a,Elong}$ of 35 kJ mol^{-1}, which were comparable results of HET-s PFD amyloid formation with of $E_{a,Elong}$ of 60-71 kJ mol^{-1} [18]. Meanwhile, the activation energy of β2m folding in neutral pH ($E_{a,Nu}$ of 68 kJ mol^{-1}) [19] was higher than activation energies of amyloid formation. I speculate that activation energies of amyloid formation may be higher than that of $E_{a,Nu}$ in neutral pH, which favors kinetically folding to native structures than amyloid formation. Indeed, amyloid formation of β2m native structures at physiological conditions was not observed [20]. However, the addition of destabilizer such as SDS or hydrophobic substances promoted β2m amyloid formation [20] due probably to the decrease in activation energy of unfolding and amyloid formation. In acidic conditions, $E_{a,Na}$ may be much higher which prefers kinetically amyloid formation.

Protein folding of globular proteins is generally accompanied by negative ΔH and ΔC_p as a result of formation of a number of non-covalent bond and burial of hydrophobic residues to cores, respectively. Similarly, negative ΔH and ΔC_p following amyloidogenesis is interpreted as formation of hydrogen bonds among monomers and burial of hydrophobic residues to cores in fibrils, respectively. Thus, ΔH was a driving force for both β2m folding and fibrillation as negative ΔH decreases the magnitude of Gibbs free energy. Furthermore, thermodynamic parameters provided structural information. Higher magnitudes of negative values of ΔH (-391 kJ mol^{-1}) and ΔC_p (-9.8 kJ mol^{-1}) of fibrillation than those of folding implicated that hydrogen bonds in fibrils formed under more hydrophobic environments which strengthens hydrogen bonds and buried hydrophobic surface areas of amyloidogenesis may be larger than those of folding.

Energy landscape provided us with fundamental insights into amyloid formation in terms of thermodynamics and kinetics. More energy landscapes constructed using ITC results of amyloid formation of other amyloidogenic proteins and peptides will be helpful to reveal general natures of the mechanism of amyloid formation and the structural property of amyloids.

4.2. Energy landscape of polymorphic amyloid formation of β2m

Amyloid structures have been examined using various methods. NMR, X-ray, and cryo-EM provided directly three-dimensional structures at the atomic level [21]. CD and FT-IR have been successfully used for investigation of secondary structures of fibrillar aggregates. AFM, EM, and Total Internal Reflection Fluorescence revealed fibrillar morphology at the level of single fibrils [8]. On the one hand, ThT reports surfaces of amyloid fibrils [22]. Different structures or strains of amyloid fibrils have been revealed using above methods such as polymorphs of amyloid β peptides, insulin, glucagon, and Sup35NM [23-26].

β2m formed amyloid fibrils at various conditions used here and no significant polymorphic fibrillation was indicated based on ThT fluorescence, far-UV CD spectra, and AFM images (Figs. 2B, 3B, and S3-5). However, different Δ*H* of amyloid formation depending on the change in the stirring speed (Fig. 2D) or the concentration of ficoll (Fig. 3D) suggested polymorphic amyloidogenesis as Δ*H* reflects structural information such as molecular packing, order of molecular contacts, and intramolecular forces. Distinct kinetic parameters encouraged the concept of polymorphs of fibrillation (Fig. 2E, F and Fig. 3E, F). Thus, I constructed the energy landscape of polymorphic amyloid formation of β2m on the basis of thermodynamic and kinetic results obtained using ITC (Fig. 5).

Amyloid fibrils formed with different packing under shear stress in this order: amyloid fibrils with Δ*H* of ~ -600 kJ mol^{-1} (strong agitation of 1,400 rpm) > amyloid fibrils with Δ*H* of ~ -400 kJ mol^{-1} (intermediate agitation of 1,000 rpm) > amyloid fibrils with Δ*H* of ~ -300 kJ mol^{-1} (mild agitation of 600 rpm). Crowding effects with the addition of 0.3 g ml^{-1} ficoll further decreased the magnitude of Δ*H* to ~ -700 kJ mol^{-1} with strong agitation of 1,400 rpm, suggesting the formation of tighter packing in cores regions of fibrils. As energy barriers (i.e., activation energy) show, amyloid fibrillation was also under kinetic control. Activation energies of nucleation were generally larger than those of fibril elongation and were in this order, ② ≈

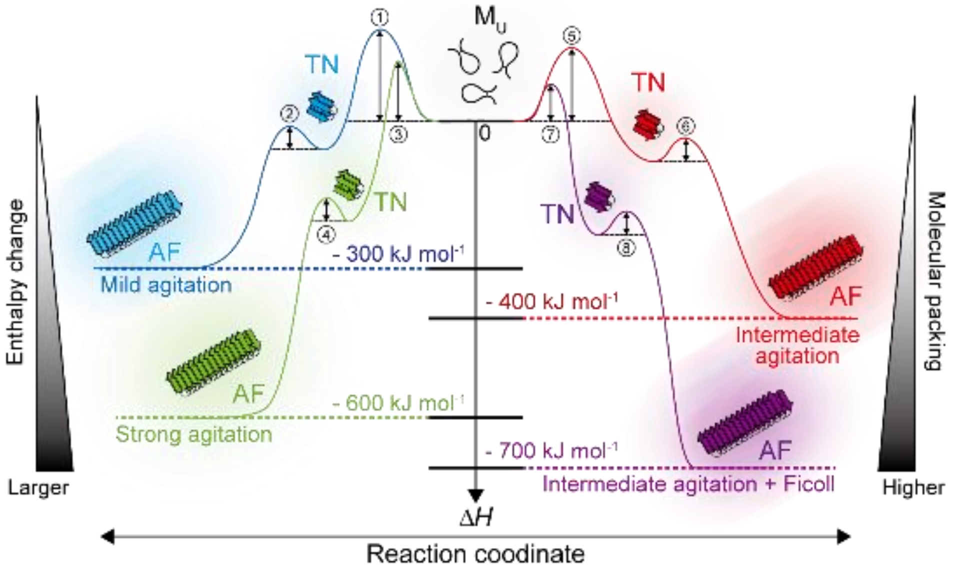

Fig. 4. Comparison of energy landscapes of β2m folding and misfolding-induced amyloid formation. Energy landscapes of β2m folding (left) and amyloidogenesis (right) are schematically depicted. Activation energy for β2m folding ($E_{\mathrm{a,Na}}$) from the *cis* conformation (ref) on the left as well as for template formation after the nucleation ($E_{\mathrm{a,Nu}}$) and fibril growth ($E_{\mathrm{a,Elong}}$) on the right is represented with double-headed black arrows and numerical values. The Δ*H* value of formation of native structures at 37 °C (ref) and amyloid fibrils at 37 °C and a stirring speed of 600 rpm is also indicated with double-headed blue and red arrows, respectively. Unfolded ($\mathrm{M_U}$) and native β2m monomers ($\mathrm{M_N}$) (PDB ID: 2YXF) [31] as well as templates after nucleation (TN) and mature amyloid fibrils (AF) of β2m are shown with cartoons. ΔC_p values of native folding and amyloid formation of β2m are also represented.

④ ≈ ⑥ ≈ ⑧ <<< ⑦ << ③ < ⑤ < ①. Agitation was more kinetically effective to nucleation than fibril elongation. Stronger agitation and shear force might promote cavitation [27] which accelerated nucleation. Macromolecular crowders facilitated productive nucleation due probably to the excluded volume effect [28] which strengthened interprotein interactions to increase local concentrations, however, slowed down the fibril growth as a result of restriction of diffusion of free monomers [29].

Variable thermodynamic outcomes of formation of amyloid fibrils due to their context-sensitive polymorphic natures are unique but may be view as one of generic properties of amyloidogenesis originated through interprotein interactions distinguished from intramolecular protein folding. Polymorphism may be beneficial for survival of functional amyloids.

Supporting information

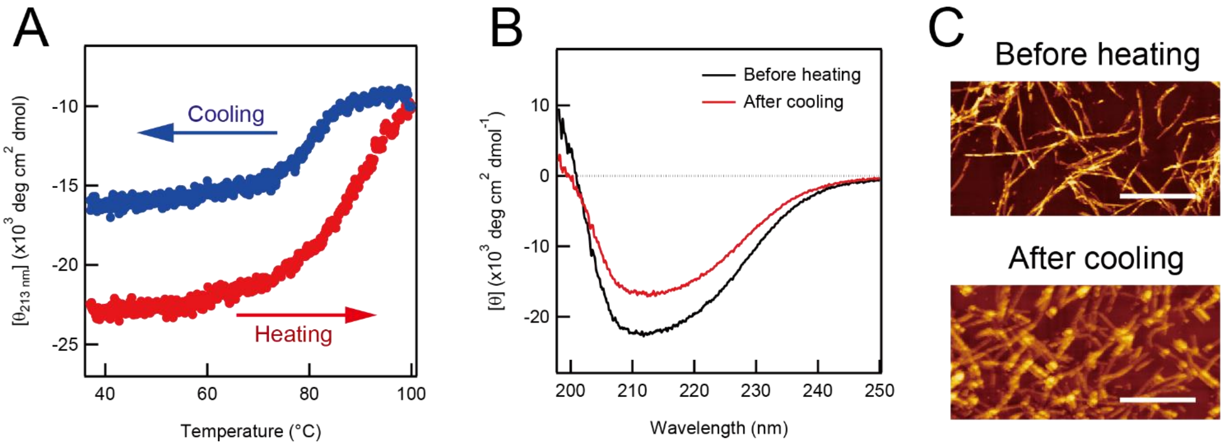

Fig. S1. Reversibility of thermal unfolding of β2m amyloid fibrils.

(A) Heating (red) and cooling (blue) of β2m amyloid fibrils between 37 and 100 °C were traced with CD intensity at 215 nm at the heating rate of 1 °C min^{-1}. (B and C) β2m amyloid fibrils before heating and after cooling were characterized using far-UV CD spectra (B) and AFM (C). CD measurements of β2m amyloid fibrils (0.1 mg·ml^{-1} μM β2m monomers) in 10 mM HCl solution (pH 2.5) containing 100 mM NaCl and its reversibility were performed using a JASCO J820 spectropolarimeter (Tokyo, Japan). Quartz cuvette with a 0.1-cm pathlength and a cell holder equipped with a water circulator were used. CD intensities were shown as mean residue ellipticity, [θ] (deg cm^2 dmol^{-1}) after subtraction of the solvent background.

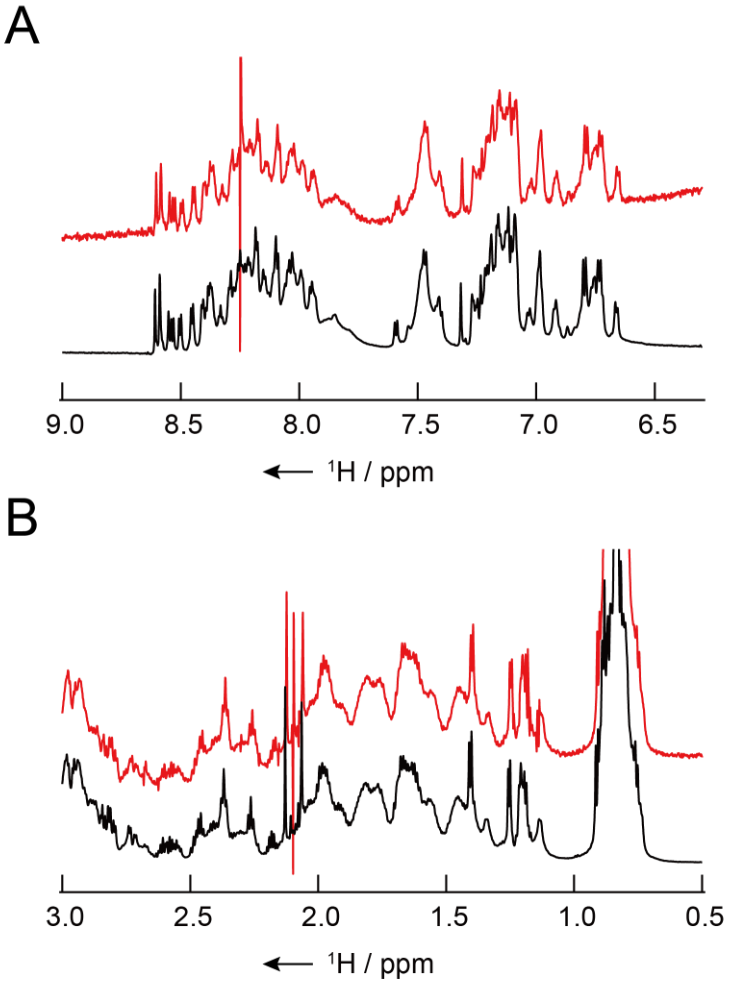

Fig. S2. One-dimensional proton NMR spectra of β2m monomer at various concentrations of ficoll.

(A and B) Solution NMR spectra of acid-unfolded β2m at 37 °C in the absence (black) and presence of excess amounts of ficoll (red). Low and high field regions are separately represented for the main chain and aromatic residues (A) and for the methyl and methylene groups of side chains for simplicity (B). NMR spectra after the subtraction of those of ficoll are shown.

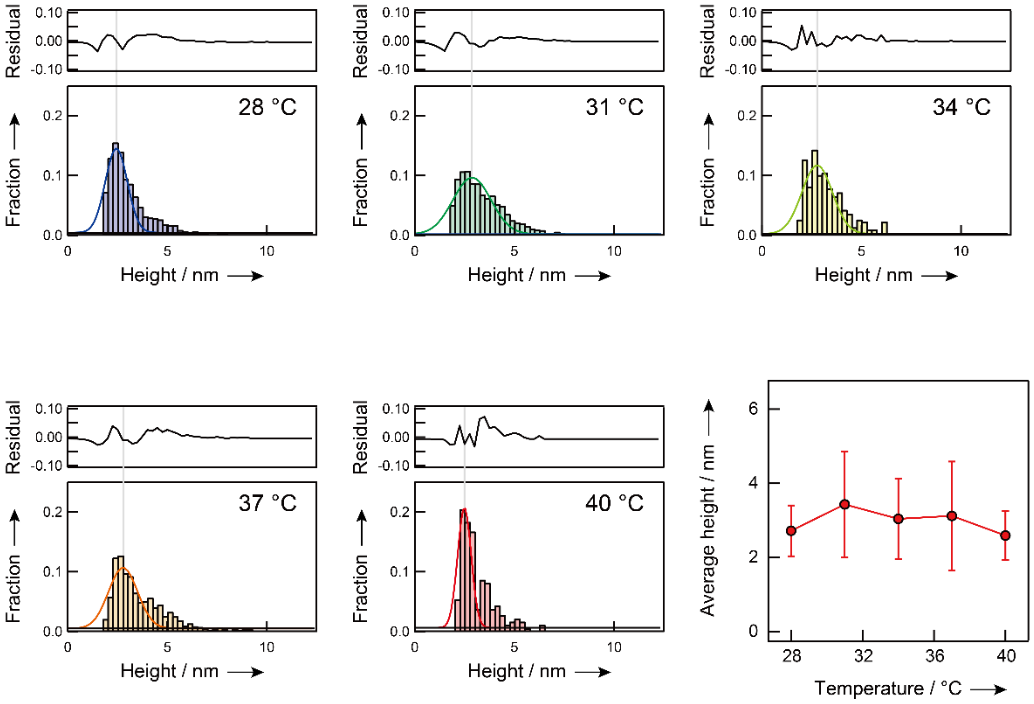

Fig. S3. Analyses of AFM images of β2m amyloid fibrils after ITC measurements at various temperatures. (A-E) Distribution of the height of amyloid fibrils formed at 28 (A), 31 (B), 34 (C), 37 (D), and 40 °C (E) with a stirring speed of 1,000 rpm is shown. Fractions of fibrils with distinct heights are represented using histograms at each lower panel. Fit curves of histograms to the Gaussian function are indicated using solid lines. Residuals of fit are shown at upper panels. The center of the Gaussian fit is indicated the vertical line. (F) Average values of the height of amyloid fibrils with standard deviations were plotted as a function of temperature for generating amyloids.

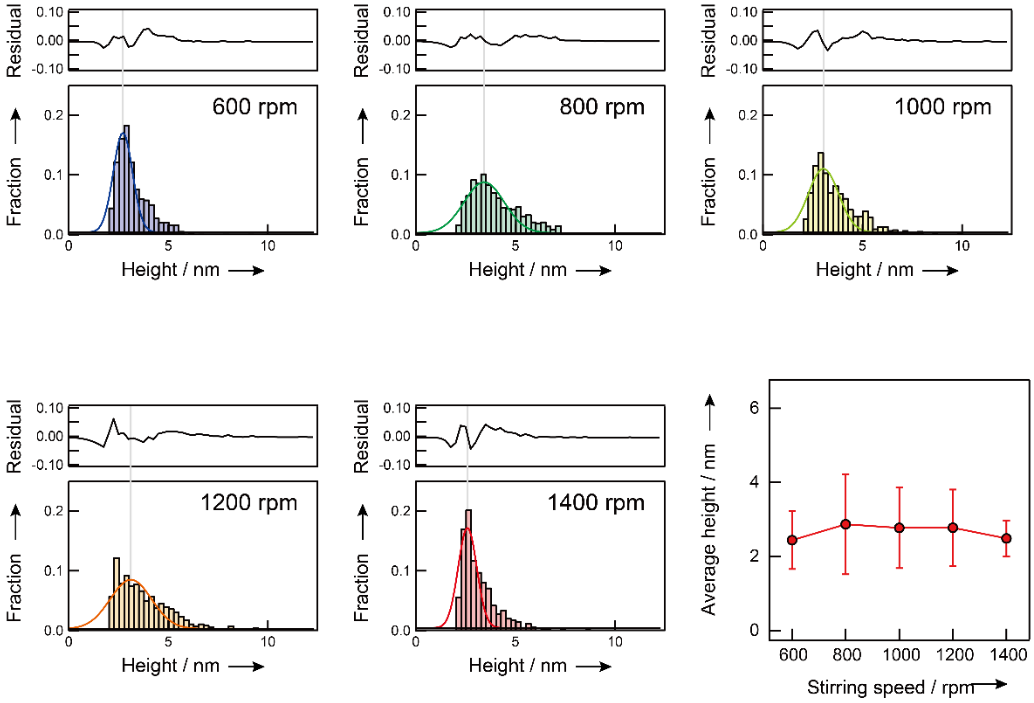

Fig. S4. Analyses of AFM images of β2m amyloid fibrils after ITC measurements at various stirring speeds. (A-E) Distribution of the height of amyloid fibrils formed at 37 °C with the stirring speed of 600 (A), 800 (B), 1,000 (C), 1,200 (D), and 1,400 rpm (E) is shown. Fractions of fibrils with distinct heights are represented using histograms at each lower panel. Fit curves of histograms using the Gaussian function are indicated with solid lines. Residuals of fit are shown at upper panels. The center of the Gaussian fit is indicated the vertical line. (F) Average values of the height of amyloid fibrils with standard deviations were plotted as a function of the stirring speed for generating amyloids.

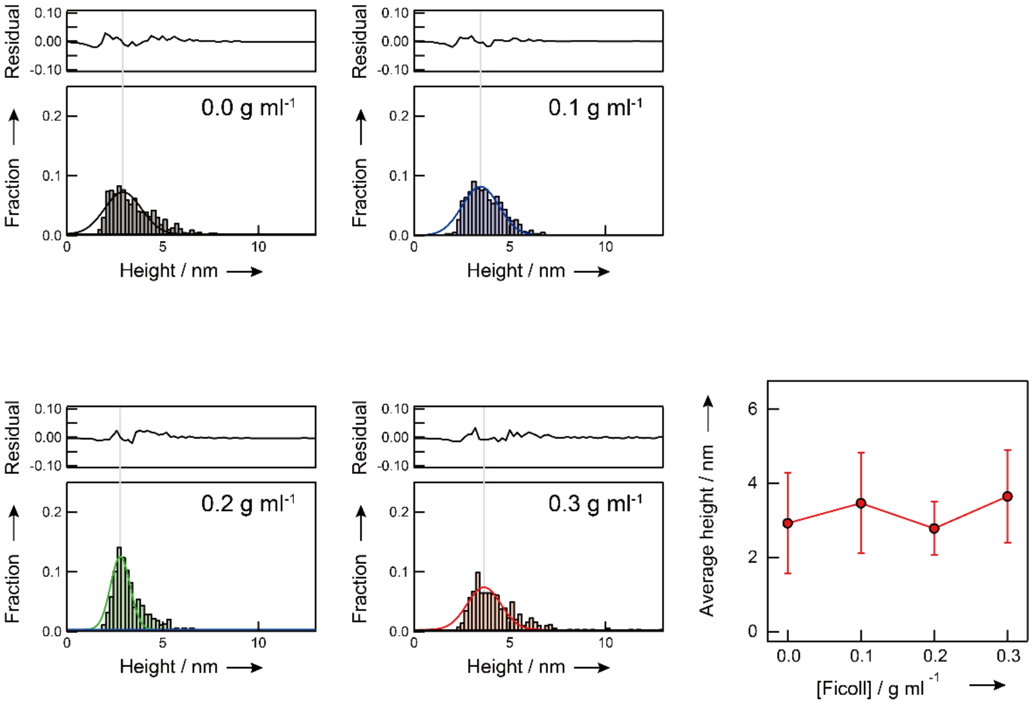

Fig. S5. Analyses of AFM images of β2m amyloid fibrils after ITC measurements at various concentrations of ficoll.

(A-E) Distribution of the height of amyloid fibrils formed at 37 °C with the stirring speed of 1,000 rpm in the presence of ficoll at 0.0 (A), 0.1 (B), 0.2 (C), and 0.3 g ml^{-1} (D). Fractions of fibrils with distinct heights are represented using histograms at each lower panel. Fit curves of histograms based on the Gaussian function are indicated using solid lines. Residuals of fit are shown at upper panels. The center of the Gaussian fit is indicated the vertical line. (F) Average values of the height of amyloid fibrils with standard deviations were plotted as a function of the concentration of ficoll for ITC measurements.

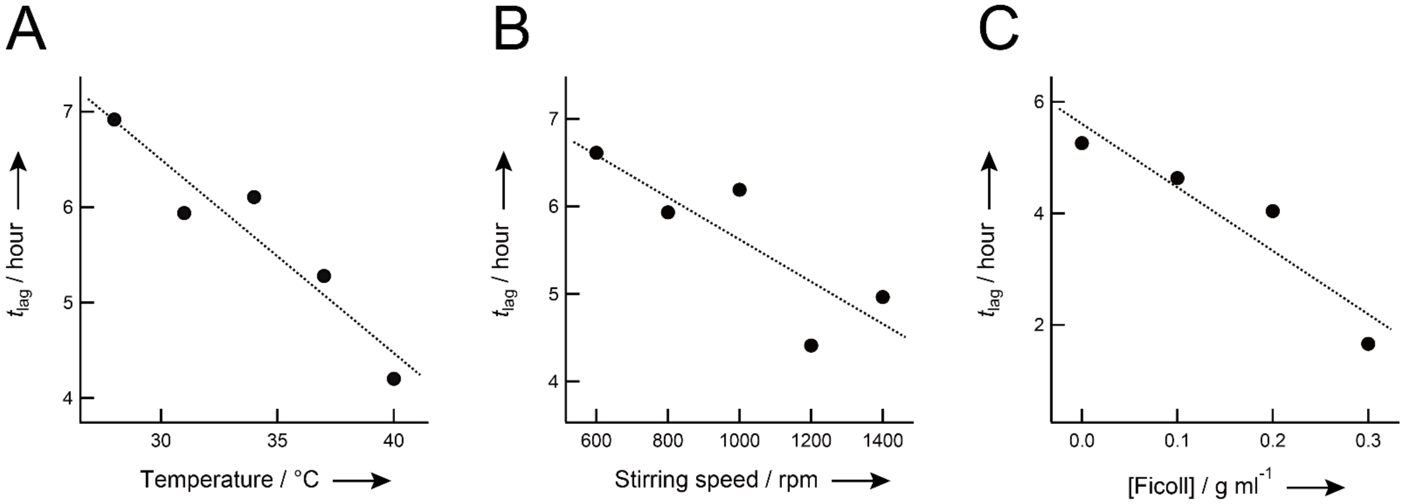

Fig. S6. Variances in the lag time of β2m amyloidogenesis under various conditions.

(A-E) Lag times were plotted as a function of temperature at 1000 rpm (A), stirring speed at 37 °C (B), and the concentration of ficoll at 1,000 rpm and 37 °C (C). Broken straight lines in A-C were drawn for eye-guide.

References

[1] C. Hammond, A. Helenius, Quality control in the secretory pathway, Curr Opin Cell Biol, 7 (1995) 523-529.

[2] C.M. Dobson, Protein folding and misfolding, Nature, 426 (2003) 884-890.

[3] Y. Lin, Y.H. Lee, Y. Yoshimura, H. Yagi, Y. Goto, Solubility and supersaturation-dependent protein misfolding revealed by ultrasonication, Langmuir, 30 (2014) 1845-1854.

[4] H. Muta, Y.H. Lee, J. Kardos, Y. Lin, H. Yagi, Y. Goto, Supersaturation-limited amyloid fibrillation of insulin revealed by ultrasonication, J Biol Chem, 289 (2014) 18228-18238.

[5] Y. Yoshimura, Y. Lin, H. Yagi, Y.H. Lee, H. Kitayama, K. Sakurai, M. So, H. Ogi, H. Naiki, Y. Goto, Distinguishing crystal-like amyloid fibrils and glass-like amorphous aggregates from their kinetics of formation, Proc Natl Acad Sci U S A, 109 (2012) 14446-14451.

[6] T.P.J. Knowles, M. Vendruscolo, C.M. Dobson, The amyloid state and its association with protein misfolding diseases, Nature Reviews Molecular Cell Biology, 15 (2014) 384.

[7] Y. Lin, J. Kardos, M. Imai, T. Ikenoue, M. Kinoshita, T. Sugiki, K. Ishimori, Y. Goto, Y.-H. Lee, Amorphous Aggregation of Cytochrome c with Inherently Low Amyloidogenicity Is Characterized by the Metastability of Supersaturation and the Phase Diagram, Langmuir, 32 (2016) 2010-2022.

[8] M.S. Terakawa, H. Yagi, M. Adachi, Y.H. Lee, Y. Goto, Small liposomes accelerate the fibrillation of amyloid beta (1-40), J Biol Chem, 290 (2015) 815-826.

[9] M. Kinoshita, E. Kakimoto, M.S. Terakawa, Y. Lin, T. Ikenoue, M. So, T. Sugiki, A. Ramamoorthy, Y. Goto, Y.H. Lee, Model membrane size-dependent amyloidogenesis of Alzheimer's amyloid-beta peptides, Phys Chem Chem Phys, 19 (2017) 16257-16266.

[10] Y.H. Lee, E. Chatani, K. Sasahara, H. Naiki, Y. Goto, A comprehensive model for packing and hydration for amyloid fibrils of beta2-microglobulin, J Biol Chem, 284 (2009) 2169-2175.

[11] E. Chatani, Y.H. Lee, H. Yagi, Y. Yoshimura, H. Naiki, Y. Goto, Ultrasonication-dependent production and breakdown lead to minimum-sized amyloid fibrils, Proc Natl Acad Sci U S A, 106 (2009) 11119-11124.

[12] K. Sasahara, H. Yagi, H. Naiki, Y. Goto, Heat-induced conversion of beta(2)-microglobulin and hen egg-white lysozyme into amyloid fibrils, J Mol Biol, 372 (2007) 981-991.

[13] K. Sasahara, H. Yagi, H. Naiki, Y. Goto, Thermal response with exothermic effects of beta2-microglobulin amyloid fibrils

and fibrillation, J Mol Biol, 389 (2009) 584-594.

[14] T. Ikenoue, Y.H. Lee, J. Kardos, M. Saiki, H. Yagi, Y. Kawata, Y. Goto, Cold denaturation of alpha-synuclein amyloid fibrils, Angew Chem Int Ed Engl, 53 (2014) 7799-7804.

[15] T. Ikenoue, Y.H. Lee, J. Kardos, H. Yagi, T. Ikegami, H. Naiki, Y. Goto, Heat of supersaturation-limited amyloid burst directly monitored by isothermal titration calorimetry, Proc Natl Acad Sci U S A, 111 (2014) 6654-6659.

[16] K. Yanagi, K. Sakurai, Y. Yoshimura, T. Konuma, Y.H. Lee, K. Sugase, T. Ikegami, H. Naiki, Y. Goto, The monomer-seed interaction mechanism in the formation of the beta2-microglobulin amyloid fibril clarified by solution NMR techniques, J Mol Biol, 422 (2012) 390-402.

[17] B. Bohrmann, M. Haider, E. Kellenberger, Concentration evaluation of chromatin in unstained resin-embedded sections by means of low-dose ratio-contrast imaging in STEM, Ultramicroscopy, 49 (1993) 235-251.

[18] R. Sabate, V. Castillo, A. Espargaro, S.J. Saupe, S. Ventura, Energy barriers for HET-s prion forming domain amyloid formation, Febs j, 276 (2009) 5053-5064.

[19] M. Sakata, E. Chatani, A. Kameda, K. Sakurai, H. Naiki, Y. Goto, Kinetic coupling of folding and prolyl isomerization of beta2-microglobulin studied by mutational analysis, J Mol Biol, 382 (2008) 1242-1255.

[20] S. Yamamoto, K. Hasegawa, I. Yamaguchi, S. Tsutsumi, J. Kardos, Y. Goto, F. Gejyo, H. Naiki, Low concentrations of sodium dodecyl sulfate induce the extension of beta 2-microglobulin-related amyloid fibrils at a neutral pH, Biochemistry, 43 (2004) 11075-11082.

[21] A.W.P. Fitzpatrick, B. Falcon, S. He, A.G. Murzin, G. Murshudov, H.J. Garringer, R.A. Crowther, B. Ghetti, M. Goedert, S.H.W. Scheres, Cryo-EM structures of tau filaments from Alzheimer's disease, Nature, 547 (2017) 185-190.

[22] D.J. Lindberg, A. Wenger, E. Sundin, E. Wesen, F. Westerlund, E.K. Esbjorner, Binding of Thioflavin-T to Amyloid Fibrils Leads to Fluorescence Self-Quenching and Fibril Compaction, Biochemistry, 56 (2017) 2170-2174.

[23] E.J. Alred, M. Phillips, W.M. Berhanu, U.H. Hansmann, On the lack of polymorphism in Abeta-peptide aggregates derived from patient brains, Protein Sci, 24 (2015) 923-935.

[24] W. Dzwolak, S. Grudzielanek, V. Smirnovas, R. Ravindra, C. Nicolini, R. Jansen, A. Loksztejn, S. Porowski, R. Winter, Ethanol-perturbed amyloidogenic self-assembly of insulin: looking for origins of amyloid strains, Biochemistry, 44 (2005) 8948-8958.

[25] C.B. Andersen, M.R. Hicks, V. Vetri, B. Vandahl, H. Rahbek-Nielsen, H. Thogersen, I.B. Thogersen, J.J. Enghild, L.C. Serpell, C. Rischel, D.E. Otzen, Glucagon fibril polymorphism reflects differences in protofilament backbone structure,

J Mol Biol, 397 (2010) 932-946.

[26] B.H. Toyama, M.J. Kelly, J.D. Gross, J.S. Weissman, The structural basis of yeast prion strain variants, Nature, 449 (2007) 233-237.

[27] Y. Iida, M. Ashokkumar, T. Tuziuti, T. Kozuka, K. Yasui, A. Towata, J. Lee, Bubble population phenomena in sonochemical reactor: I Estimation of bubble size distribution and its number density with pulsed sonication – Laser diffraction method, Ultrasonics Sonochemistry, 17 (2010) 473-479.

[28] H.-X. Zhou, G. Rivas, A.P. Minton, Macromolecular Crowding and Confinement: Biochemical, Biophysical, and Potential Physiological Consequences, Annual Review of Biophysics, 37 (2008) 375-397.

[29] A. Bancaud, S. Huet, N. Daigle, J. Mozziconacci, J. Beaudouin, J. Ellenberg, Molecular crowding affects diffusion and binding of nuclear proteins in heterochromatin and reveals the fractal organization of chromatin, The EMBO Journal, 28 (2009) 3785-3798.

[30] T. Chiba, Y. Hagihara, T. Higurashi, K. Hasegawa, H. Naiki, Y. Goto, Amyloid fibril formation in the context of full-length protein: effects of proline mutations on the amyloid fibril formation of beta2-microglobulin, J Biol Chem, 278 (2003) 47016-47024.

[31] K. Iwata, T. Matsuura, K. Sakurai, A. Nakagawa, Y. Goto, High-resolution crystal structure of beta2-microglobulin formed at pH 7.0, J Biochem, 142 (2007) 413-419.

Publication list

1. **Misaki Kinoshita**, Ju Yaen Kim, Satoshi Kume, Yukiko Sakakibara, Toshihiko Sugiki, Chojiro Kojima, Genji Kurisu, Takahisa Ikegami, Toshiharu Hase, Yoko Kimata-Ariga, and Young-Ho Lee, "Physicochemical nature of interfaces controlling ferredoxin NADP$^+$ reductase activity through its interprotein interactions with ferredoxin", ***Biochim. Biophys. Acta, Bioenerg.***, **1847**, 1200-1211 (2015)

2. Yuxi Lin, József Kardos, Mizue Imai, Tatsuya Ikenoue, **Misaki Kinoshita**, Toshihiko Sugiki, Koichiro Ishimori, Yuji Goto, and Young-Ho Lee, "Amorphous aggregation of cytochrome *c* with inherently low amyloidogenicity is characterized by the metastability of supersaturation and the phase diagram", ***Langmuir***, **8**, 2010-2022 (2016)

3. Toru Kawakami, Yuichi Mishima, **Misaki Kinoshita**, Young-Ho Lee, and Isao Suetake, "A thiirane linker for isopeptide mimetics by peptide ligation", ***Tetrahed. Lett.***, **57**, 2112-2115 (2016)

4. Ju Yaen Kim, **Misaki Kinoshita**, Satoshi Kume, Hanke Guy Thomas, Toshihiko Sugiki, John E. Ladbury, Chojiro Kojima, Takahisa Ikegami, Genji Kurisu, Yuji Goto, Toshiharu Hase, and Young-Ho Lee, "Non-covalent forces tune the electron transfer complex between ferredoxin and sulfite reductase to optimize enzymatic activity", ***Biochemical J.***, **473**, 3837-3854 (2016)

5. **Misaki Kinoshita**, Ju Yean Kim, Yuxi Lin, Natalia Marlova, Toshiharu Hase, and Young-Ho Lee, "Biochemical and biophysical methods to examine the effects of site-directed mutagenesis on enzymatic activities and interprotein interactions", ***Methods Mol. Biol. (Springer)***, **1498,** 439-460 (2017)

6. Ju Yaen Kim, **Misaki Kinoshita**, Takashi Inui, Genji Kurisu, Yuji Goto, Toshiharu Hase, Koichiro Ishimori, and Young-Ho Lee, "Thermodynamics of protein-protein interactions examined by isothermal titration calorimetry", ***Protein-Protein Interactions (PPIs): Types, Methods for Detection and Analysis (Nova Science Publishers, Inc.)***, 67-80 (2017)

7. Tatsuya Ikenoue, Yuxi Lin, **Misaki Kinoshita**, Kazumasa Sakurai, Yuji Goto, and Young-Ho Lee, "Molecular Structure of Amyloid Fibrils Revealed by Thermodynamics", ***Protein-Protein Interactions (PPIs): Types, Methods for Detection and Analysis (Nova Science Publishers, Inc.)***, 81-96 (2017)

8. Tatsuya Ikenoue, **Misaki Kinoshita**, Yuxi Lin, and Young-Ho Lee, "Biophysical application of calorimetric methods to protein misfolding and aggregation examinations", ***Malvern white paper*** (2017) (online review article)

9. **Misaki Kinoshita**, Ju Yaen Kim, Yuxi Lin, and Young-Ho Lee, "Practical tips for MicroCal PEAQ-ITC experiments: troubleshooting and additional help to maximize performance", ***Malvern technical note*** (2017) (online review article)

11. **Misaki Kinoshita**, Ju Yean Kim, Satoshi Kume, Yuxi Lin, K. Hun Mok, Yosky Kataoka, Koichiro Ishimori, Natalia Marlova, Genji Kurisu, Toshiharu Hase, and Young-Ho Lee, "Energetic basis on interactions between ferredoxin and ferredoxin NADP$^+$ reductase at varying physiological conditions", ***Biochem. Biophys. Res. Commun.***, **482**, 909-915 (2017)

12. **Misaki Kinoshita**, Yxi Lin, Masatoshi Nakatsuji, Takashi Inui, and Young-Ho Lee, "Kinetics and polymorphs of yeast prion Sup35NM amyloidogenensis", ***Int. J. Biol. Macromol.***, **102**, 1241-1249 (2017)

13. **Misaki Kinoshtia#**, Erina Kakimoto#, Mayu S. Terakawa, Yuxi Lin, Tatsuya Ikenoue, Masatomo So, Toshihiko Sugiki, Ayyalusamy Ramamoorthy, Yuji Goto, and Young-Ho Lee (#these authors contributed equally), "Model membrane size-dependent amyloidogenesis of Alzheimer's amyloid-β peptides", ***Phys. Chem. Chem. Phys.***, **19**, 16257-16266 (2017)

14. Mayu S. Terakawa#, Young-Ho Lee#, **Misaki Kinoshita#**, Yuxi Lin, Toshihiko Sugiki, Naoya Fukui, Tatsuya Ikenoue, Yasushi Kawata, and Yuji Goto*, (#these authors contributed equally) "Membrane-induced initial structure of α-synuclein control its amyloidogenesis on model membranes", ***Biochim. Biophys. Acta, Biomembranes.***, *In press* (2017)

15. Donghoon Kim, Je Min Yoo, Heehong Hwang, Junghee Lee, Su Hyun Lee, Seung Pil Yun, Myung Jin Park, MinJun Lee, Seulah Choi, Sang Ho Kwon, Saebom Lee, Seung-Hwan Kwon, Sangjune Kim, Yong Joo Park, **Misaki Kinoshita**, Young-Ho Lee, Seokmin Shin, Seung R. Paik, Seulki Lee, Byung Hee Hong, and Han Seok Ko, "Graphene quantum dots prevent α-synuclein transmission in Parkinson's disease", ***Nature Nanotechnol.,*** *Under review* (3rd round) (2017)

16. **Misaki Kinoshita**, Yuxi Lin, Toshihiko Sugiki, and Young-Ho Lee, "Kinetic Study on Amyloid Formation of Alzheimer's Amyloid β(1-42)", ***J. Appl. Sol. Chem. Model.,*** *Submitted* (2017)

17. **Misaki Kinoshtia** et al., "Energy landscapes of amyloid formation of β2-microglobulin", *In preparation* (Chapter IV)